Numerical studies of magnetism and transport properties in graphene nanodevices

Thu Phung

UNIVERSITÉ de Cergy-Pontoise

LPTM Laboratoire de Physique Théorique et Modélisation

THÈSE DE DOCTORAT

UNIVERSITÉ DE CERGY-PONTOISE

Présentée par

Thị Thu PHÙNG

POUR OBTENIR LE GRADE DE **DOCTEUR**

SPÉCIALITÉ : PHYSIQUE THÉORIQUE

Numerical studies of magnetism and transport properties in graphene nano-devices

---

Date de la soutenance : 16 Décembre 2019

Devant le jury de thèse :

Mme. Christine Richter	Université de Cergy-Pontoise	Présidente
M. Daniel Cabra	Universidad Nacional de La Plata	Rapporteur
M. François Peeters	University of Antwerpen	Rapporteur
M. Jean Avan	Université de Cergy-Pontoise	Examinateur
M. Grégoire Misguich	Institut de Physique Théorique, CEA Saclay	Examinateur
M. Andreas Honecker	Université de Cergy-Pontoise	Directeur de thèse
M. Guy Trambly de Laissardière	Université de Cergy-Pontoise	Invité

Unité de Recherche: Laboratoire de Physique Théorique et Modélisation

Résumé

Les matériaux à deux dimensions retiennent l'attention d'un grand nombre physiciens de la matière condensées du fait leur applications potentielles. Parmi eux, le *graphène* a été l'objet de nombreuses études depuis la première analyse expérimentale d'un plan d'atomes de carbone en 2004. Ses propriétés inhabituelles en font un bon candidat pour remplacer le silicium. Les nano-structures en nid d'abeille, telles que les 'dots' quantiques, apparaissent comme des briques élémentaires pour des nouveaux microcircuits électroniques. Les propriétés de ces nano-structures sont déterminées principalement par les bords qui sont à l'origine d'états de basses énergies – canaux de bords – gouvernant les propriétés de transport. En outre les bords en configuration zigzag, qui favorisent les corrélations électroniques, sont à l'origine d'un état magnétique alors que le graphène infini est non magnétique. La combinaison possible de ces propriétés font de cet nano-matériaux de bons candidats pour des applications en spintronique.

Ce travail de thèse contribue à la compréhension théorique des ces phénomènes. Concrètement, nous utilisons une approche de champ moyen pour calculer les propriétés magnétiques et de transport de nano-flocons de graphène. Pour cela nous utilisons un modèle de Hubbard avec énergies d'interaction de Coulomb sur site. Des études antérieures ont montré que la méthode du champ moyen donne de bons résultats pour traiter les interactions, y compris pour l'étude des propriétés dynamiques. Techniquement, lorsque un état de champ moyen a été déterminé de façon auto-cohérente, le problème est équivalent à celui d'électrons sans interaction. La première partie de la thèse est consacrée au graphène infini, dont le résultat en champ moyen dans l'approximation de Hartree-Fock est connu, pour étudier l'effet du couplage spin-orbite sur les interactions électroniques et évaluer la précision de la méthode par rapport aux autres méthodes numériques. Nous montrons, entre autres, que le semi-métal de gap nul (sans spin-orbite) et l'isolant topologique (avec spin-orbite) sont stables pour des valeurs faibles et intermédiaires de l'interaction électron-électron, alors qu'un état anti-ferromagnétique apparaît aux fortes interactions. L'ordre anti-ferromagnétique sans spin-orbite est un ordre de Néel et un ordre plan simple avec spin-orbite. La deuxième partie est consacrée à l'étude du magnétisme des nano-flocons de graphène sans tenir compte du couplage spin-orbite. L'apparition du moment magnétique aux bords des flocons dépend directement de leur taille, leur géométrie et la configuration de leurs bords. L'origine du magnétisme

de bords est due aux états de bords localisés lorsque les bords sont en configuration 'zigzag' alors que ces états disparaissent lorsque les bords sont en configuration 'armchair'. La dernière partie est consacrée à l'étude du transport résolu en spin (spin up et spin down) d'une nano-flocon hexagonale magnétique en contact avec deux réservoirs ayant des températures différentes, par la méthode des fonctions de Green hors équilibre combinée aux résultats en champ moyen. Lorsque la différence de température entre les réservoirs est non nulle, des courants de spin up et down circulent en sens opposés dans la nano-flocon de graphène. Cela est dû aux différences de concentration de porteurs de charge dans les deux réservoirs, déterminée par la distribution de Fermi-Dirac, et le coefficient de transmission de la nano-flocon. Nos calculs montrent qu'un effet Seebeck parfait, c'est à dire un pur courant du spin sans courant de charge, un fort filtrage de spin et une amplification du courant de spin, peut être obtenu pour certaines valeurs des températures des réservoirs, du gradient de température et de la tension de grille appliquée. Ces résultats ouvrent la voie vers de nouvelles applications des nano-flocons de graphène dans le domaine de la spin-caloritronique.

Abstract

2D materials are attracting attention from a big research community in solid-state physics because of a large number of applications. Among these materials *graphene* has been at the focus of attention ever since its experimental realization as a single layer of carbon atoms in 2004 as an alternative to silicon due to its many unusual properties. Honeycomb nanostructures such as quantum dots constitute fundamental building blocks for potential device applications. Essential ingredients of such nanostructures are provided by the edges since they give rise to low-energy excitations. Accordingly, such edge channels will dominate the transport of a nano-device. Furthermore, zigzag edges are unstable with respect to interactions such that one may get magnetism at these edges even if for example bulk graphene is non-magnetic. The combination of both factors bears promise for spintronic applications.

The current work contributes to the theoretical understanding of the aforementioned phenomena. Concretely, we use a single-band Hubbard model with an on-site Coulomb interaction combined with the mean-field theory in order to compute the magnetic and transport properties of graphene nanoflakes. Previous investigations have shown that a mean-field decoupling of the interaction yields surprisingly accurate answers even for dynamical properties. At a technical level, once a static mean-field has been determined self-consistently, the problem is reduced to non-interacting electrons. A first part of this thesis revisits the Hartree-Fock mean-field approximation for bulk graphene to study the impact of electron-electron interaction with and without spin-orbit coupling and concurrently assess its accuracy by comparing with other numerical methods. The gapless semi-metal (for zero spin-orbit coupling) and the topological band insulator (for nonzero spin-orbit coupling) are stable for weak to intermediate electron-electron interaction, and undergo a transition to an antiferromagnetic phase at strong interaction. The antiferromagnetic order is of the Néel type without spin-orbit coupling, and of the easy-plane type with spin-orbit coupling. The systematic investigation of magnetism on graphene nanoflakes is the second part of the present work when ignoring the spin-orbit coupling. The onset of the edge magnetic moment strictly depends on the size of the graphene nanoflakes, the geometry and the edge termination. Herein, the origin of the magnetism on the edges of graphene nanoflakes is attributed to the localized edge states in zigzag edges which vanish in armchair edges. A final part of the dissertation investigates spin-resolved transport properties depending on the thermal

bias, typically the transport of charge carriers via spin-up and spin-down states, in a magnetic hexagonal graphene nanoflake connected with two metallic leads. As a temperature difference is applied, significant spin-up and spin-down currents, which are computed using the non-equilibrium Green's function technique combined with the mean-field theory, flow in opposite directions through the graphene nanoflakes. This is the consequence of the imbalance of charge carrier concentrations, which is determined by the Fermi-Dirac distribution at the two leads, and transmission spectra. Furthermore, our calculations show that a perfect spin-Seebeck effect, a pure spin current without charge current, a high spin-filtering effect as well as the amplification of spin current can be obtained by tuning the temperature at the leads, the temperature gradient and the back-gate voltage. These results pave the way for new application potential of the graphene nanoflakes in the field of spin caloritronics.

Acknowledgements

Foremost, I would like to express my most sincere gratitude to my supervisors: Prof. Andreas Honecker and Dr. Guy Trambly de Laissardière for their support, fruitful discussion, patience, enthusiasm, and immense knowledge. Without their guidance and encouragement this work would have taken a longer time. Thank you for giving me the opportunity to participate in the international group where I have exchanged scientific knowledge with other researchers.

My sincere thanks go to Dr. Javad Vahedi who works as a Postdoc in Laboratoire de Physique Théorique et Modélisation for his training, helping and sharing in research. Thank you for your dedicated guidance in calculating and building the computing program together with the useful discussions which help me solve the stalemate in researching problems.

I would like to express my thanks to Prof. Fakher F. Assaad, Robert Peters, Martin Hohenadler and Nayuta Takemori for their helpful discussion and data used in this thesis.

I am profoundly grateful to Prof. Diep The Hung and Prof. Trong Tuong Truong who have given me enthusiastic assistance and great advice, and my thanks to Cédric Gerard for his assistance, especially in relation to the computer. I also express my appreciation to Laboratoire de Physique Théorique et Modélisation, Somepalli Venkateswarlu, Pierre Fromholz, Quentin Duprey and Maheshwor Tiwari for supporting and helping me a lot since the first days I came to France.

My sincere gratefulness to University Science and Technology of Hanoi (USTH) and Vietnamese government (Project 911) for financial support.

Last but not least, special thanks to my parents for their immense love together with unconditional and endless support. I would also like to thank my young brother, my young sister-in-law and my best friend Do Hai Doan for giving me a lot of encouragement on both the work and the life during three years in France.

Contents

1 Introduction **1**

1.1 Motivation . . . 1

1.2 The electronic properties of graphene . . . 6

1.2.1 Crystal structure of graphene . . . 6

1.2.2 Electronic band structure of graphene . . . 8

1.2.3 Graphene nanoribbons . . . 11

2 Models and Method **15**

2.1 The Hubbard model . . . 15

2.2 The Kane-Mele-Hubbard model . . . 18

2.3 The mean-field theory . . . 23

3 Magnetism in graphene nanoflakes **30**

3.1 Review: Magnetism in graphene . . . 31

3.2 Phase diagram . . . 35

3.3 Magnetism in graphene nanoflakes . . . 40

4 The non-equilibrium Green's function method **44**

4.1 Introduction . . . 44

4.2 Setup transport problem . . . 46

4.3 The non-equilibrium Green's function formalism . . . 48

4.3.1 Basic formulas . . . 48

4.3.2 The current of charge carriers . . . 51

4.4 Wide-band limit approximation . . . 54

5 Thermally induced spin current across a spin caloritronic device **56**

5.1 Thermally induced spin current . . . 57

5.2 The physical mechanism of thermally induced spin current . . . 61

5.3 The back-gate voltage-modulated spin current . . . 67

5.4 The charge and spin thermovoltage . . . 73

6 Summary **76**

Appendices **79**

A Thermally induced spin current across a spin caloritronic device **80**

A.1 The thermally induced spin current within the dynamic mean-field theory 80

A.2 The transmission coefficient under the particle-hole symmetry 82

A.3 The impact of the degree of chiral symmetric breaking on magnetism and transport properties in graphene nanoflakes 86

List of Figures

1.1 Left: Honeycomb crystal structure of graphene consists of two sublattices: A (red) and B (blue) with Bravais lattice vectors (yellow arrows) a_1 and a_2 together with the nearest-neighbor vectors (black arrows) δ_1, δ_2, δ_3. Right: First Brillouin Zone of graphene with a central point Γ, two nonequivalent so-called K and K' points and M positioned at the middle of KK', and the reciprocal lattice vectors (red arrows) b_1 and b_2 7

1.2 Three dimensional energy dispersion for bulk graphene (a). Density of states as a function of energy (b). 9

1.3 Honeycomb structure of graphene with two edges: Armchair edge and zigzag edge. 12

1.4 Energy band structure of graphene nanoribbons for armchair edge with the width of $N = 10$ (a) and 20 (c) and their corresponding DOS (b) and (d), respectively, for zigzag edge with $N = 20$ (e) and its DOS (f). 13

2.1 Single-particle energy spectra (left) and corresponding DOS (right) for the graphene honeycomb lattice with some values of λ/t obtained from the Kane-Mele model. 21

2.2 Energy band structure (left) and DOS (right) of the zigzag GNRs for $N = 4$ (a) and $N = 20$ (b), respectively, at $\lambda = 0.2t$ obtained from the Kane-Mele model. 22

2.3 Algorithm of the self-consistent calculation 26

2.4 Single-particle energy spectra of the graphene honeycomb lattice using the Kane-Mele-Hubbard model within the Hartree-Fock mean-field approximation for (a) $U = 0$, $\lambda = 0$, (b) $U = 2.5t$, $\lambda = 0$, (c) $U = 2.5t$, $\lambda = 0.1t$. 27

3.1 (a) Staggered magnetization and single-particle gap (in the inset) Δ_{sp} versus U/t within the mean-field Hubbard approximation. (b) Phase diagram using the KMH model at the mean-field level. The inset displays the data obtained from the MFT (red circles) and QMC (blue triangles). 37
3.2 Staggered magnetization and single-particle gap (in the inset) as a function of U/t with the intrinsic SOC $\lambda = 0.5t$. 38
3.3 Phase diagram using KMH model in the mean-field approximation with the AF moment in z direction (blue line) and x direction (red line). 39
3.4 Staggered magnetization M_s on the edges (a, b) and single-particle gap Δ_{sp} (c, d) versus U/t, and local magnetic moments (e, f) for hexagonal and diamond GNFs, respectively. Pink circles denote the magnitude of spin-up densities, while yellow ones are proportional to the magnitude of spin-down densities. The insets of figures (a) and (b) display the dependence of U_c/t on the number of sites on each nanoflake. 41
3.5 Local density of states (LDOS) at each site of the hexagonal (a) and diamond (b) nanoflakes for the energy of $E = 0\ eV$. The area of each blue circle is proportional to the amplitude of the LDOS. 42

4.1 (a) The schematic configuration of a two-lead device. The contact position of leads with the edges of GNFs in three configurations: (b) *ortho*, (c) *meta* and (d) *para*. 47

5.1 Spin-resolved currents versus U/t at $T_S = 0.026t$ and $\Delta T = 0.0052t$ for different sizes of hexagonal zigzag GNFs (a). The maximum value of spin-up current (blue curve) and corresponding value U_h/t (red curve) with respect to the number of sites of nanoflakes N (b). Here $\eta = 10^{-2}t$ and $\Gamma = 0.02t$. 58
5.2 Spin-resolved currents versus T_S/t and temperature gradient ΔT for different nanoflake sizes with $\eta = 10^{-2}t$ and $\Gamma = 0.02t$. 59
5.3 The carrier concentration difference between the source and the drain. 62
5.4 Transmission coefficient as a function of E/t in (a) *ortho* and (b) *para* configurations for four nanoflakes plotted in separate panels. Here $U = U_h$, $\eta = 10^{-2}t$ and $\Gamma = 0.02t$. 63

5.5 Transmission coefficient for spin-up and spin-down versus E/t in *meta* configuration for four nanoflakes. Here $U = U_h$, $\eta = 10^{-2}t$ and $\Gamma = 0.02t$. 64
5.6 Spin-resolved current spectra $J(E)$ versus energy E/t for different T_S and a fixed $\Delta T = 0.0052t$ for four nanoflakes: $N = 54$ (a), 96 (b), 294 (c) and 600 (d) with $U = U_h$, $\eta = 10^{-2}t$ and $\Gamma = 0.02t$. 65
5.7 Spin-resolved current spectra versus energy E/t at several ΔT and a fixed $T_S = 0.026t$ for four configurations: $N = 54$ (a), 96 (b), 294 (c) and 600 (d) with $U = U_h$, $\eta = 10^{-2}t$ and $\Gamma = 0.02t$. 66
5.8 The dependence of the spin-resolved currents on the back-gate voltage V_g at $T_S = 0.026t$ and $\Delta T = 0.0052t$ for the nanoflakes with $U = U_h$, $\eta = 10^{-2}t$ and $\Gamma = 0.02t$. 68
5.9 Spin-up and spin-down currents with respect to T_S and ΔT, and transmission coefficient as a function of E/t for $N = 96$ (a), (b), (c) and $N = 600$ (d), (e), (f) at a fixed $V_g/t = -0.04$, respectively, with $\eta = 10^{-2}t$ and $\Gamma = 0.02t$. 70
5.10 The impact of the Coulomb energy U on the charge and spin currents under several V_g for four nanoflakes, wherein (a) and (e) for $N = 54$, (b) and (f) for $N = 96$, (c) and (g) for $N = 294$, and (d) and (h) for $N = 600$, respectively, at $T_S = 0.026t$ and $\Delta T = 0.0052t$ with $\eta = 10^{-2}t$ and $\Gamma = 0.02t$. 71
5.11 Charge and spin thermovoltages as a function of ΔT and V_g for four nanoflakes: (a) and (b) for $N = 54$, (c) and (d) for $N = 96$, (e) and (f) for $N = 294$, and (g) and (h) for $N = 600$, respectively, with $\eta = 10^{-2}t$ and $\Gamma = 0.02t$. 74

A.1 Spin-resolved currents driven by the temperature gradient versus T_S with ΔT (a) and transmission coefficient (b) as a function of E/t for $N = 600$ at $U/t = 0.8$ and 1.6 using the real-space DMFT. 81
A.2 Phase diagram of graphene nanoflakes: $N = 96$ and $N = 600$ using the mean-field Hubbard model (a). Staggered magnetization on the edges of graphene nanoflake of 600 sites for $\epsilon = 0t$, $0.1t$, $0.2t$ and $0.3t$ (b). 87

A.3 The dependence of the spin-up and spin-down currents on ϵ/t at $T_S = 0.026t$ and $\Delta T = 0.0052t$ for several hexagonal graphene nanoflakes with the zigzag edge. Herein the repulsive Coulomb energy is U_h/t corresponding to each nanoflake, see Table 5.1, $\eta = 10^{-2}t$ and $\Gamma = 0.02t$. 88

A.4 Spin-resolved current as a function of U/t for several values of $\epsilon = 0t$, $0.1t$, $0.2t$ and $0.3t$ at $T_S = 0.026t$ and $\Delta T = 0.0052t$ for $N = 294$ (a) and $N = 600$ (b) with $\eta = 10^{-2}t$ and $\Gamma = 0.02t$. 89

A.5 Spin-resolved transmission spectra with respect to E/t for $N = 600$ at $U = 0t$, $0.8t$, $1.2t$ and a fixed $\epsilon = 0.1t$ with $\eta = 10^{-2}t$ and $\Gamma = 0.02t$. 90

List of abbreviations

AF	Antiferromagnetic
AFI	Antiferromagnetic Insulator
BZ	Brillouin Zone
DFT	Density Functional Theory
DMFT	Dynamical Mean-Field Theory
DOS	Density of State
GNRs	Graphene Nanoribbons
GNFs	Graphene nanoflakes
hBN	hexagonal Boron Nitride
KMH	Kane-Mele-Hubbard
LDA	Local Density Approximation
MFT	Mean-Field Theory
NEGF	Non-Equilibrium Green's Function
NRG	Numerical Renormalization Group
QHE	Quantum Hall Effect
QMC	Quantum Monte Carlo
QSHE	Quantum Spin Hall Effect
SM	Semi-Metal
SOC	Spin-Orbit Coupling
SSE	Spin Seebeck Effect
TB	Tight-Binding
TBI	Topological Band Insulator
VCA	Variational Cluster Approach

Chapter 1

Introduction

Contents

1.1 Motivation 1

1.2 The electronic properties of graphene 6

1.2.1 Crystal structure of graphene 6

1.2.2 Electronic band structure of graphene 8

1.2.3 Graphene nanoribbons 11

In this chapter, we manifest the motivation, ideas and structure of the thesis. Next will be the fundamentals and electronic properties of graphene.

1.1 Motivation

According to Mermin-Wagner theorem, two-dimensional materials should be thermodynamically unstable and they therefore could not exist in nature. Nevertheless, the reality indicated the opposite through the appearance of the graphene sheet which was first isolated in 2004 [1, 2]. That result not only robustly confirms the existence of two-dimensional materials in nature, but also sets up a stone for an extremely interesting new field of research. Although graphene has been theoretically studied since 1947 with the first investigation carried out by Wallace [3], its fame really began after its isolation and the Nobel Prize which was awarded to A. Geim and K. Novoselov in 2010. Since then, there is great attention for the isolation, identification and characterization of graphene and other two-dimensional materials such as hexagonal boron nitride (hBN), transition metal dichalcogenides (MoS_2, $MoSe_2$, $MoTe_2$, WS_2, WSe_2,...), silicene, etc.

Both experiment and theory show that graphene with a unique electronic band

structure near the Fermi energy is a lot more than just a two-dimensional material. In particular, the conduction band and valence band touch each other at two nonequivalent Dirac points, called K and K', with zero bandgap and zero density of states (DOS) at the Fermi energy. Graphene is hence a gapless semiconductor or a semimetal (SM). Most prominently, graphene can be described by the Dirac equation for the massless fermions at low energy. However, the spin and the speed of light in the Dirac Hamiltonian are here replaced by the sublattice degrees of freedom (known as *pseudospin*) and graphene Fermi velocity [4]. Moreover, the conservation of *pseudospin* can give rise to outstanding properties in graphene such as the absence of backscattering or Klein tunneling where an incident electron is totally transmitted by a local defect [4]. Because of these properties, graphene possesses a relatively large electronic mobility which can reach up to $2 \times 10^5\ cm^2V^{-1}s^{-1}$ [5,6]. Combining with the high thermal conductivity [7], graphene has created a great revolution in the development of efficient electronic devices in the present era. In addition to the interesting electronic properties, graphene with other impressive properties has been driving it to various fields, leading to a new graphene era. For instance, owing to its high surface area and good dispersion in various solvents, graphene can be used to build a highly efficient capacitor [8]. Graphene has received positive responses for biomedical applications such as drug delivery, biomedical imaging, biosensors, etc., due to its biocompatibility, non-toxicity, selectivity and solubility in a biological system [9]. Graphene nanoflakes (GNFs) with the finite band gap have further potential applications in photodetection, photovoltaic and light-emitting diodes (Leds) [10], and so on.

Most notably, graphene has attracted much more attention for applications to spintronics for several reasons as follows. (1) The weak spin-orbit coupling of graphene results in the relatively easy control of the electron spin [11] by the external fields such as the electric field or the Rashba spin-orbit coupling. It is considered as a consequence of the simple relation between the carrier wavevector and the external fields [12]. (2) The spin diffusion length has been theoretically proposed up to 100 μm with the spin lifetime approximately 1 μs [13, 14]. Many recent experimental results have confirmed the potential of graphene for spin transport with long spin diffusion length over tens of micrometers and long spin relaxation time at room temperature [12, 15, 16]. Experimental studies of spin transport in hBN encapsulated single-layer graphene in nonlocal spin valves showed a spin relaxation time of 2 ns and spin relaxation length exceeding 12 μm at room temperature [12], as

an example. (3) Furthermore, it is worth mentioning that graphene behaves as a new magnetic material with nontrivial magnetic properties, *i.e.*, magnetic moment on zigzag edges, because graphene does not contain d or f electrons. More importantly, one-dimensional graphene nanoribbons (GNRs) can be fabricated and one can control precisely the edges of the ribbons in experiment [17, 18]. Consequently, the investigation of magnetic properties in graphene has been highly encouraged as the main subject in many works. As indicated, the pristine graphene does not hold magnetic moment because of the balance of the two graphene sublattices. Yet numerous studies on both theory and experiment show that the magnetic properties in graphene can be induced by defects because they are considered as sources so as to generate the imbalance in the two graphene sublattices [19–25]. The defects can be vacancies, impurities effect, light and heavy adatoms, non-metal doping or Coulomb correlation. The spins on the same sublattice exhibit ferromagnetic order and the spins on different sublattices are found to show antiferromagnetic (AF) order. On the other hand, the emergence of edge states and the reduction of dimensionality give rise to a significant modification in the electronic band structure of graphene. So they affect directly on the magnetism of graphene systems at nanoscales such as graphene nanoribbons and graphene nanoflakes. Not only theoretical findings but also recent experimental findings have indicated the presence of spin polarization on the edges of GNRs [26, 27]. The edge magnetism in graphene nanostructures has been also predicted [28]. Simultaneously their potential application in spintronics has been proven by numerous proposals in relation to GNF-based devices [29–31] as well. Therefore, we focus on the investigation of the edge magnetism in the graphene nanoflakes using the mean-field Hubbard model at half-filling and zero temperature.

In addition, the study of the spin-resolved transport in graphene nanostructures has been also the goal of numerous works [32–34]. As indicated by Luo et al. [33] the spin-polarized electron transport through a system of hexagonal zigzag-edge GNFs attached between two electrodes is decided by the magnetic configuration of the system. Namely, that work shows that the electron transport at low energy is not significantly affected by the long-range interactions and the conductance is found quenched mainly by the short-range interactions in the lowest antiferromagnetic state. Yet the conductance becomes spin-dependent in the ferromagnetic state. By applying a bias voltage to such a system, a spin-polarized current is generated wherein the current in the ferromagnetic state is found to be larger than that in the antiferromagnetic state [35]. The utilization of the bias voltage is an extensively

used way for manipulating the electron current via spin-up and spin-down states in spintronic devices [36–39]. Recently, a novel approach used to modulate the transport of spin current in the spintronic devices is based on the thermal bias [40–43]. Striking advantages of this approach not only solve effectively the problem of heat dissipation, or energy waste which is one of the big challenges in the design of nanostructure devices nowadays, but also can integrate multiple functions in a device with low power consumption. Such a device can be considered as a combination of thermoelectric and spintronic effects that paves the way for a new and fertile research field, well-known as *spin caloritronics*. The majority of works in this field have emphasized on examining the spin-dependent transport in finite GNRs due to spin polarization along its edges in the ground state [44, 45]. Therefore, we choose the hexagonal zigzag GNFs as the main component of our spin caloritronic device because the hexagonal zigzag GNFs can be realized easily in experiment [46]. A common way for studying the interplay of the spin and heat transport through such a system is to use the non-equilibrium Green's function (NEGF) method combined with the density functional theory (DFT) [45,47]. Nonetheless, it requires a big computational resource and takes a long time if a large number of atoms are calculated. For simplicity, the mean-field theory is thus prioritized to use for obtaining main features in a graphene nanoflakes in our work rather than the DFT. The features of the transport are then computed by the NEGF. Consequently, the present work is organized as follows:

In the subsequent parts of this chapter, the honeycomb structure of graphene with characteristic parameters will be described in detail. Next will be a brief introduction of its unique band structure for the itinerant π-electrons based on the nearest neighbor-hopping tight-binding (TB) model. The band structure of graphene is linear and behaves as massless Dirac fermions near the Fermi energy where the conduction and valence bands are adjacent at two nonequivalent Dirac points. More importantly, the huge influence of the electronic edge states on the energy band structure will be described within the nearest-neighbor hopping TB Hamiltonian for the graphene nanoribbons.

Chapter 2 begins with a general overview of the models and method which allow us to study desirable properties of the graphene nanoflakes. The issue of electron-electron interaction leading to the spin-polarized states in graphene nanostructures is solved by the Hubbard model which (only) takes into account the Coulomb interaction of

electrons on the same site. In addition, this chapter also represents how the spin-orbit coupling (SOC) is involved and its impact on the energy band structure of graphene by means of the Kane-Mele model. The combination of the Hubbard model with the Kane-Mele model yields the Kane-Mele-Hubbard (KMH) model which is employed to study the interplay between the spin-orbit interaction and electron-electron interaction on the graphene honeycomb lattice. At the end of chapter 2, we describe the mean-field theory (MFT) within the Hartree-Fock approximation and its application to the KMH model for the graphene honeycomb lattice.

The numerical results obtained from the Hubbard model and the KMH model within the MFT are analyzed and discussed in Chapter 3. The beginning of this chapter is an overview of the magnetism studied in graphene. Next, we reconsider the phase diagram of the graphene honeycomb lattice without and with the SOC interaction within the Hartree-Fock mean-field theory. In analogy to more sophisticated methods such as quantum Monte Carlo simulations, a transition from the semi-metal phase (without SOC) and the topological insulator phase (with SOC) to the antiferromagnetic insulator phase takes place at strong interaction. Then we discuss the impact of the electron-electron interaction encoded by a parameter U on the magnetism in GNFs with different sizes and geometries (typically, hexagon and diamond). Calculations show that the spontaneous magnetization on the edges induced by the electron-electron interaction crucially depends on the geometry, the edge termination and the size of the graphene system.

In chapter 4 we give a definition and a brief introduction of the *spin caloritronic* devices. The detailed description of a spin caloritronic device based on the magnetic GNFs sandwiched between two metallic leads will be indicated shortly thereafter. In such a device, a spin current is expected to flow from the left lead to the right lead (or vice versa) in the presence of a thermal bias rather than a voltage bias. Therefore, this chapter provides the Landauer-Büttiker formula to compute the spin current across the device and describes how the non-equilibrium Green's function method invoked to calculate the transport properties.

Chapter 5 presents the results obtained from the NEGF method combined with the mean-field approximation. A spin current is generated in the graphene nanoflakes when the temperature gradient and the magnetism on the edges are triggered. However, depending on the contact location of the leads with the edges of GNFs such spin current can or can not be produced. Simultaneously, the effect of the repul-

sive Coulomb energy, back-gate voltage and sublattice potential on the thermally induced spin current are analyzed and discussed as well. Finally, brief summaries will be given in chapter 6, then appendices and references for the thesis.

1.2 The electronic properties of graphene

1.2.1 Crystal structure of graphene

Graphene is a two-dimensional crystal of carbon atoms arranged in a honeycomb lattice due to their sp^2 hybridization. The distance between the nearest carbon atoms is $a \simeq 0.142$ nm. In a solid, each carbon atom has 6 electrons written in the electron configuration: $1s^2 2s^2 2p^2$ in which two electrons fill the inner shell $1s$ and do not participate in any chemical reactions. All important properties of carbon-based materials can be determined by the four remaining electrons occupying the outer shell of $2s$ and $2p$ ($2p_x$, $2p_y$, $2p_z$). In the ground state, the energy of the $2s$ orbital is less than that of the $2p$ orbitals, two electrons are thus located in the $2s$ orbital and the two remaining electrons are in the $2p$ orbitals. In graphene, these four electrons are responsible for forming the sp^2 hybridization. Wherein three electrons in the $2s$ and two $2p$ orbitals participate in the formation of in-plane sp^2 hybridization which produces three σ bonds. The remaining electron in the p_z orbital, which is perpendicular to graphene plane, forms the π bond [4, 48, 49]. Electrons in σ bonds (σ electrons) are far away from the Fermi energy, while those in π bonds (π electrons) are close to the Fermi energy. The π electrons therefore take responsibility for electronic properties at low energy.

The two-dimensional graphene's honeycomb lattice can be described in terms of two inter-penetrating triangular sublattices. Consequently, one can view graphene as a triangular Bravais lattice with a basis of two carbon atoms per unit cell, labeled A and B, indicating a bipartite lattice structure. The triangular Bravais lattice vectors can be written as [50]

$$\mathbf{a_1} = \left(\frac{3a}{2}, \frac{\sqrt{3}a}{2}\right) \quad \text{and} \quad \mathbf{a_2} = \left(\frac{3a}{2}, \frac{-\sqrt{3}a}{2}\right) \tag{1.1}$$

where a is the carbon-carbon distance. Figure 1.1(Left) illustrates that each carbon

atom on the A sublattice has three nearest-neighbor carbon atoms on the B sublattice and vice versa. Three vectors $\boldsymbol{\delta_1}$, $\boldsymbol{\delta_2}$ and $\boldsymbol{\delta_3}$ which connect a site on the A sublattice with three nearest sites on the B sublattice are defined as [50]

$$\boldsymbol{\delta_1} = \left(\frac{a}{2}, \frac{\sqrt{3}a}{2}\right), \quad \boldsymbol{\delta_2} = \left(\frac{a}{2}, \frac{-\sqrt{3}a}{2}\right), \quad \boldsymbol{\delta_3} = (-a, 0)\,. \tag{1.2}$$

The six second nearest-neighbor vectors are positioned at: $\boldsymbol{\delta'_{1,2}} = \pm a_1$, $\boldsymbol{\delta'_{3,4}} = \pm a_2$, $\boldsymbol{\delta'_{5,6}} = \pm(a_2 - a_1)$.
The reciprocal lattice vectors corresponding to (1.2) are given by

$$\mathbf{b_1} = \left(\frac{2\pi}{3a}, \frac{2\pi\sqrt{3}}{3a}\right) \quad \text{and} \quad \mathbf{b_2} = \left(\frac{2\pi}{3a}, \frac{-2\pi\sqrt{3}}{3a}\right). \tag{1.3}$$

The area of each unit cell of graphene is $S_u = 3\sqrt{3}a \approx 0.051\ nm^2$ and the density of carbon atoms is calculated as $n_c = 2/S_u = 39 \times 10^{15} cm^{-2}$. The density of valence electrons equals exactly to the density of carbon atoms and is $39 \times 10^{15} cm^{-2}$ because there is one π electron per carbon atom [48].

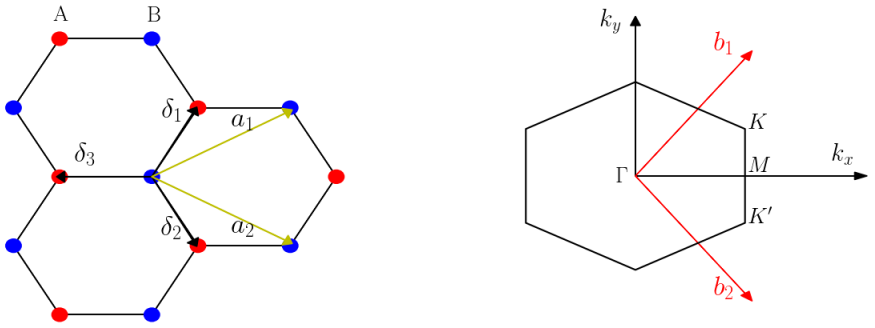

Figure 1.1: Left: Honeycomb crystal structure of graphene consists of two sublattices: A (red) and B (blue) with Bravais lattice vectors (yellow arrows) a_1 and a_2 together with the nearest neighboring vectors (black arrows) δ_1, δ_2, δ_3. Right: First Brillouin Zone of graphene with a central point Γ, two nonequivalent so-called K and K' points and M positioned at the middle of KK', and the reciprocal lattice vectors (red arrows) b_1 and b_2 (*these figures are replotted according to Ref. [50]*).

Figure 1.1 (Right) presents the first Brillouin Zone (BZ) of graphene which has a hexagonal shape and shows a set of inequivalent points in the reciprocal space with the long wavelength excitations situated in the vicinity of the Γ point ($\Gamma = (0, 0)$) [48]. The six corners of the first BZ contains two inequivalent points K and K',

known as Dirac points as well, represented as

$$K = \left(\frac{2\pi}{3a}, \frac{2\pi}{3\sqrt{3}a}\right) \quad \text{and} \quad K' = \left(\frac{2\pi}{3a}, -\frac{2\pi}{3\sqrt{3}a}\right) \tag{1.4}$$

while the four remaining corners may be indeed connected to one of these points via a translation by a reciprocal lattice vector. These points play a crucial role in the electronic properties of graphene because the low-energy excitations are centered around the two K and K' points [48].

1.2.2 Electronic band structure of graphene

We now describe how the tight-binding (TB) model is applied for π electrons of graphene to get insight the electronic properties. In the present work, one only considers the hopping between the nearest-neighbor carbon atoms. Hence the TB Hamiltonian is given by

$$H_t = -t \sum_{\langle i,j\rangle\sigma} a^+_{i\sigma} b_{j\sigma} + h.c \tag{1.5}$$

where t ($t \simeq 2.8eV$) is the hopping amplitude between the p_z orbitals of two adjacent carbon atoms, $a^+_{i\sigma}$ ($b^+_{i\sigma}$) and $a_{i\sigma}$ ($b_{i\sigma}$) are the creation and annihilation operators of an electron with spin $\sigma = \uparrow, \downarrow$ on site i of the A (B) sublattice and $h.c$ is the Hermitian conjugate term.

The Fourier transformations for creation and annihilation operators are given by

$$\begin{aligned}
a^+_{i\sigma} &= \frac{1}{\sqrt{N}} \sum_{k\sigma} a^+_{k\sigma} e^{ikr_i} \\
a_{i\sigma} &= \frac{1}{\sqrt{N}} \sum_{k\sigma} a_{k\sigma} e^{-ikr_i} \\
b^+_{i\sigma} &= \frac{1}{\sqrt{N}} \sum_{k\sigma} b^+_{k\sigma} e^{ikr_i} \\
b_{i\sigma} &= \frac{1}{\sqrt{N}} \sum_{k\sigma} b_{k\sigma} e^{-ikr_i}
\end{aligned} \tag{1.6}$$

where N is the number of lattice points per sublattice and r_i is the position vector of A or B atom located at the i^{th} site. Applying the Fourier transformations to Eq. (1.5), the TB Hamiltonian is then written in momentum space as

$$H_t = \sum_{k\sigma} a^+_{k\sigma} b_{k\sigma} (-t \sum_n e^{-ik\delta_n}) + \sum_{k\sigma} b^+_{k\sigma} a_{k\sigma} (-t \sum_n e^{ik\delta_n}). \tag{1.7}$$

Writing H_t in the matrix form

$$H_t = \sum_{k\sigma} \begin{pmatrix} a^+_{k\sigma} & b^+_{k\sigma} \end{pmatrix} \begin{pmatrix} 0 & -t\sum_{n=1}^{3} e^{-ik\delta_n} \\ -t\sum_{n=1}^{3} e^{ik\delta_n} & 0 \end{pmatrix} \begin{pmatrix} a_{k\sigma} \\ b_{k\sigma} \end{pmatrix}. \tag{1.8}$$

one has

$$H_t(k) = \begin{pmatrix} 0 & -t\gamma_k \\ -t\gamma_k^* & 0 \end{pmatrix} \tag{1.9}$$

with $\gamma_k = \sum_{n=1}^{3} e^{-ik\delta_n}$ (δ_n is the nearest-neighbor vectors).

By diagonalizing the matrix $H_t(k)$, one obtains the energy dispersion as a function

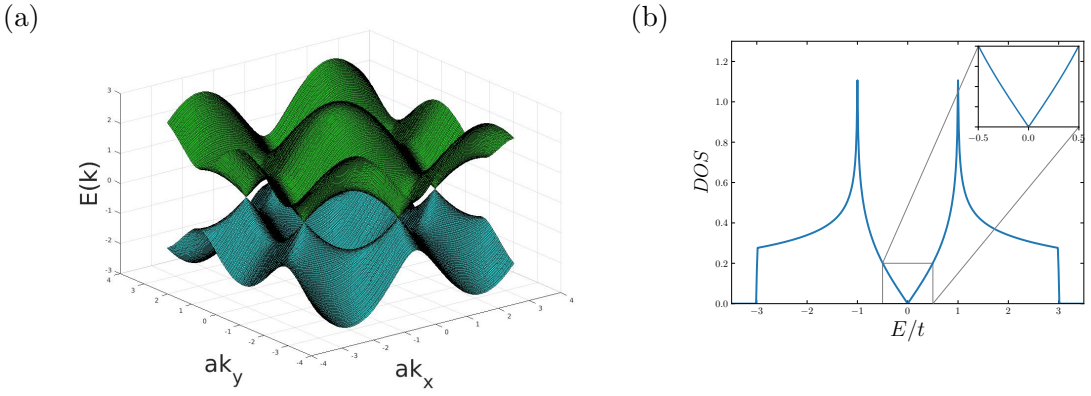

Figure 1.2: Three dimensional energy dispersion for bulk graphene (a). Density of states as a function of energy (b).

of k: $E^{\pm}(k) = \pm|t\gamma_k|$ [3, 51, 52] which can read as follows

$$E^{\pm}(k) = \pm t\sqrt{3 + 2\cos k(\delta_1 - \delta_2) + 2\cos k(\delta_1 - \delta_3) + 2\cos k(\delta_2 - \delta_3)} \tag{1.10}$$

where $E^+(k)$ and $E^-(k)$ stand for the conduction and valence bands, respectively. At half-filling, the valence band is completely filled while the other band is completely empty because each carbon atom contributes one π electron and each electron may occupy either the spin-up state or the spin-down state. The density of states (DOS) of graphene is calculated from the energy dispersion $E(k)$ as

$$DOS = \frac{2}{N}\sum_{k} \delta(E - E(k)) \tag{1.11}$$

with $\delta(E - E(k))$ describing a Delta function with respect to the energy E. As illustrated in Figure 1.2(a), the bottom of the conduction band and the top of the valence band touch each other at the six corners of the first BZ. These two bands are mirror symmetric with respect to zero energy. Besides, the DOS points out a zero bandgap between the conduction band and the valence band, as shown in Figure

1.2(b). Therefore, neutral graphene behaves as a gapless semimetal with zero energy dispersion and zero density of states at the Fermi energy E_F which exactly locates at Dirac points. One finds that the energy band structure indicates the particle-hole symmetry due to $E^{\pm}(k) = -E^{\mp}(k)$. Nonetheless, the particle-hole symmetry will be broken and the two bands will become asymmetric if one takes into consideration the second nearest-neighbor hopping [48, 50]. In addition, the time-reversal symmetry is also conversed which implies that $E^{\pm}(-k) = E^{\pm}(k)$ [50]. Consequently, if K is a solution of $E(k) = 0$, so is K', resulting in the necessary occurrence in pairs of Dirac points [48]. In graphene, there is one pair of Dirac points, the zero-energy states are thus doubly degenerate. In the proximity of the K points the energy dispersion is a linear function of the absolute value of the wave vector $(k - K)$ where the DOS linearly depends on the energy, see a zoom in of the DOS [26].

Low-energy excitations: To clarify such linear properties, it is essential to expand the energy dispersion in the vicinity of Dirac points by replacing $k = \pm K + q$ with $|q| \ll |K|$ [4, 48]. Eq. (1.9) can be then written in the form [4]

$$H(q) = \hbar v_F(\eta \sigma_x q_x + \sigma_y q_y) \tag{1.12}$$

where $\eta = 1(-1)$ for $K(K')$ points, $v_F = 3a|t|/2\hbar$ is the graphene Fermi velocity with the value $v_F \simeq 10^6$ m/s [50] and does not depend on any energy and momentum, and σ^x and σ^y are the Pauli matrices defined as

$$\sigma^x = \begin{pmatrix} 0 & 1 \\ 1 & 0 \end{pmatrix} \quad \text{and} \quad \sigma^y = \begin{pmatrix} 0 & -i \\ i & 0 \end{pmatrix} \tag{1.13}$$

Eq. (1.12) is analogous to the Dirac equation for massless fermions. Therefore the electrons in graphene are referred to as Dirac fermions. Yet the Pauli matrices in Eq. (1.12) denote the sublattice degrees of the freedom rather than the spin and the speed of light is replaced by the graphene Fermi velocity v_F [4]. For these reasons, the sublattice degrees of the freedom and the K points are called *pseudospin* and *Dirac points*, respectively. Now Eq. (1.10) becomes

$$E^{\pm}(q) = s\hbar v_F|q| \tag{1.14}$$

with $s = 1$ for the conduction band and $s = -1$ for the valence band. From Eq. (1.14), it is evident that the energy dispersion $E^{\pm}(q)$ is a linear function of q around the Dirac points. This leads to the fact that the DOS is indeed directly proportional to energy, $DOS = 2|E|/\pi\hbar^2 v_F^2$ [4].

On the other hand, interchanging the spinor components of the A and B sublattices at the K' point the effective low-energy Hamiltonian may be represented as [4, 48]

$$H^{\eta}(q) = \hbar v_F \tau^z \otimes q \cdot \sigma \tag{1.15}$$

here the Pauli matrices σ manifest the *sublattice pseudospin*, τ are also Pauli matrices representing the valley degree of freedom, called *valley pseudospin*, and $\otimes$ denotes the tensor product. The fact that the projection of the pseudospin is a well-defined conserved quantity in the low-energy limit [4, 48]. As a consequence, the conservation of the pseudospin gives rise to the absence of backscattering in graphene [53] and is at the origin of Klein tunneling [54] in which a massless Dirac particle is fully transmitted through a high electrostatic barrier without being reflected.

1.2.3 Graphene nanoribbons

In a finite structure, the graphene shows two most important edges including armchair edge and zigzag edge. These two types of edges have a tremendous impact on the energy spectrum, resulting in the change in the electronic and magnetic properties of graphene. Most remarkably, the presence of electronic states localized at the edge is expected as a source of the intrinsic magnetism and peculiar transport properties in graphene nanostructures [26]. Therefore, we briefly review here the energy structure of the graphene nanoribbon to indicate a significant edge effect at the nanoscale.

The graphene nanoribbon can be obtained by reducing the dimension of a graphene sheet along one direction to the nano-size. Figure 1.3 reveals that the armchair edge consists of carbon atoms of two graphene sublattices while the zigzag edge is only formed by carbon atoms of the A sublattice or the B sublattice. The atomically defined edges recently have been observed and controlled in experiment. By using STM (Scanning Tunnelling Microscopy) and AFM (Atomic Force Microscopy) armchair edge [18, 55–57] and zigzag edge [17, 58, 59] GNRs with high quality were experimentally observed. Even a single graphene quantum dot with zigzag edge structure was also fabricated and was detected by high-resolution TEM (Transmission Electronic Microscopy) [60]. Recently, Rajender's group successfully synthesized few-layer graphene quantum dots with the edge shape (zigzag or armchair)

controlled by different solvents [61].

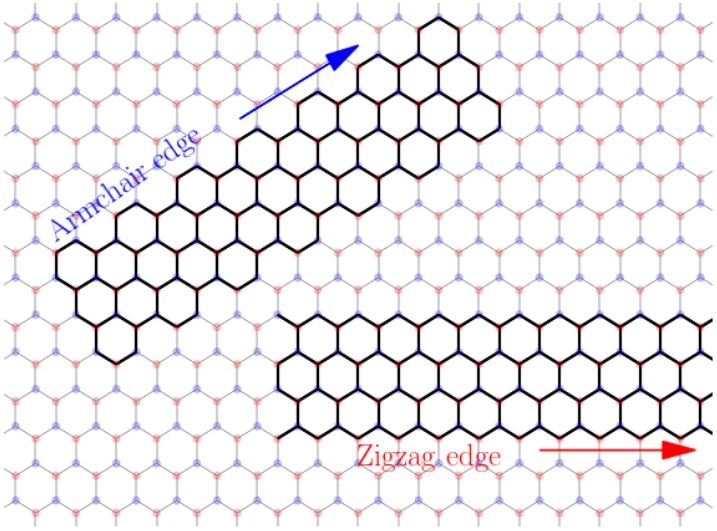

Figure 1.3: Honeycomb structure of graphene with two edges: Armchair edge and zigzag edge.

It has been known that the zigzag edge of graphene supports the electronic states located at the edge, while the armchair edge does not indicate such localized states. This difference is interpreted through the analysis of the electronic band structure of the graphene nanoribbons using the nearest-neighbor hopping TB model (the reader can see detailed calculations in Ref. [26]). Here, we define N as the width of the GNRs which identifies the number of dimer (two carbon sites) lines for armchair GNRs and the number of zigzag lines for zigzag GNRs. Figure 1.4 exhibits the large difference between the energy band structures of the armchair GNRs and those of the zigzag GNRs. For the armchair GNRs, the energy band structures rigorously depend on the width of nanoribbons and this width determines whether the GNRs are metallic or semiconducting, see Figure 1.4(a) and (b). Particularly, as $N = 3m + 2$, m is an integer, *e.g.*, $N = 20$, the conduction band and the valence band cross each other at a point of $ka = 0$, so the system becomes metallic. A direct gap at $ka = 0$ opens for the remaining widths of the nanoribbons, *i.e.*, $N = 3m + 1$ or $N = 3m$, leading to a semiconducting system with a vanishing density of states at Dirac point. However the gap decreases gradually with the increase of the width and approaches zero in the limit of very large width. Experimentally, by using angle-resolved photoemission spectroscopy and Fourier-transformed scanning tunneling spectroscopy, the electronic bandgap was measured as 2.37 eV for the 7-armchair GRN [55], 1.4 eV for the 9-armchair GNR [56] and 0.86 eV for the 15-armchair

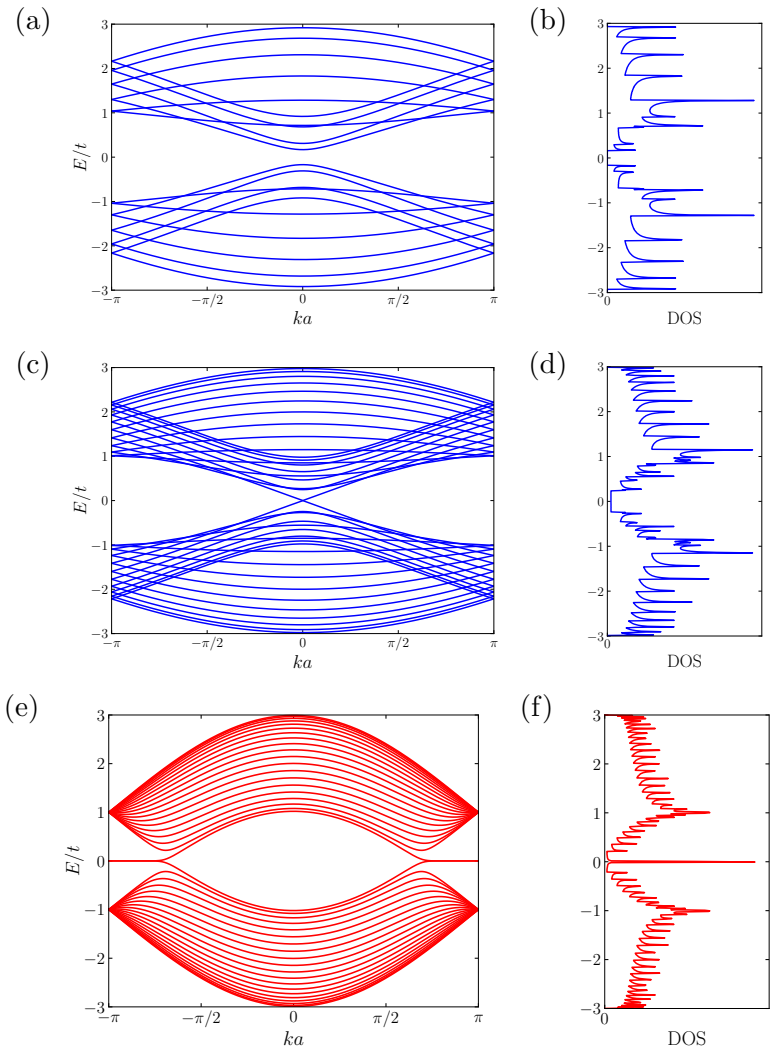

Figure 1.4: Energy band structure of graphene nanoribbons for armchair edge with the width of $N = 10$ (a) and 20 (c) and their corresponding DOS (b) and (d), respectively, for zigzag edge with $N = 20$ (e) and its DOS (f).

GNR [62]. These experimental results are in good agreement with the theoretical predictions. Otherwise, the armchair GNRs always behave as a semiconductor for all widths confirmed by the first-principles calculation within LDA approximation [63]. That approach also unveils that the smallest gap is obtained in the case of $N = 3m + 2$.

On the other hand, the zigzag GNRs reveal different behavior. The energy band structures of the zigzag GNRs do not change with an arbitrary value of N and the zigzag GNRs are always metallic. The most noticeable difference compared to the armchair nanoribbons is that one sees a pair of flat bands located at the Fermi energy in the range of $2\pi/3 < |ka| < \pi$ in the zigzag GNRs. The electronic states in

the flat bands are understood as the localized states (or known as edge states). The presence of the edge-localized states in the zigzag edge GRNs was recently proved by experiment [17, 64] using STM. It is apparent that such edge states result in a large contribution to the DOS, as can be witnessed in Figure 1.4(f). Typically a sharp peak at zero energy is shown in the DOS of the zigzag GNRs which is not observed in that of the armchair GNRs as well as of the bulk graphene. When invoking the electron-electron interaction, the spin polarization of carbon atoms belonging to the zigzag edge is developed, while there is no spin polarization in the middle of nanoribbons as well as the armchair edge for small electron-electron interaction. The origin of this property can be explained by the emergence of the edge-localized states in which the amplitude of the edge states is only non-zero at the sites of the zigzag edge and decreases in the inward direction [26]. Therefore it can be suggested that the edge states take responsibility for the magnetic properties in graphene nanostructure which will be taken into account in detail in chapter 3.

In conclusion, we reviewed in this chapter the general characteristics of graphene and applied the tight-binding model to revisit several important properties in the pristine graphene and graphene nanoribbons. Of particular importance for physical properties of graphene is the unique band structure near the Fermi energy which behaves as massless Dirac fermions and the emergence of edge-localized states at the zigzag edge.

Chapter 2

Models and Method

Contents

2.1 The Hubbard model 15

2.2 The Kane-Mele-Hubbard model 18

2.3 The mean-field theory 23

We briefly introduce in this chapter tools and method used in the present work. While the Hubbard model contains the information on the electron-electron interaction and the nearest-neighbor hopping tight-binding parameters, the Kane-Mele-Hubbard Hamiltonian involves the information held in the Hubbard Hamiltonian plus the spin-orbit coupling term. Several general features of the Hubbard model are taken over in which the particle-hole symmetry is presented more detailed. In addition, we also re-visit the results of the Kane-Mele model for bulk graphene and GNRs which was proposed by Kane and Mele in 2005. The ultimate section of this chapter represents the mean-field theory within the Hartree-Fock approximation to treat interaction. The key idea of this theory is to decouple the full wave function of the many-body problem into a single-particle wave function.

2.1 The Hubbard model

The Hubbard model contains information about the interaction of particles, original fermions moving in a solid, this model thus exhibits intriguing phenomena in nature such as ferromagnetism, a Mott-Hubbard transition, superconductivity, a Tomonaga-Luttinger liquid in one space dimension and a Pomeranchuk instability [65]. As a consequence, the Hubbard model is extensively used to study physical properties under the contribution of electron-electron interaction in the solid.

The Hubbard model was introduced independently by Hubbard [66], Kanamori [67] and Gutzwiller [68] for the description of ferromagnetism in metals in 1963. The Hubbard model is principally constructed by two parts: the hopping of electrons between the lattice sites and the repulsive on-site Coulomb interaction of electrons on the same site. The single-band Hubbard Hamiltonian is given by

$$H = -t \sum_{\langle i,j \rangle \sigma} (c^{+}_{i\sigma} c_{j\sigma} + h.c) + U \sum_{i} n_{i\uparrow} n_{i\downarrow} - \mu \sum_{i\sigma} n_{i\sigma}. \tag{2.1}$$

The first term is the kinetic energy describing the nearest-neighbor hopping on the lattice with the creation and annihilation operators $c^{+}_{i\sigma}$ and $c_{i\sigma}$ for an electron with spin σ at site i, respectively. The second term (usually called Hubbard term) denotes the electron-electron interaction on the same site. U is the repulsive Coulomb energy and $n_{i\sigma} = c^{+}_{i\sigma} c_{i\sigma}$ is the electron number operator for spin σ at site i. μ in the final term is a chemical potential which is able to control the filling.

Physically, the Hubbard model shows several important symmetries as follows [65].

1, The gauge symmetry. This is a fundamental symmetry of most models describing fermions in condensed matter physics. When using the transformations: $c^{+}_{i\sigma} \rightarrow e^{i\alpha} c^{+}_{i\sigma}$ and $c_{i\sigma} \rightarrow e^{-i\alpha} c_{i\sigma}$, the Hubbard Hamiltonian does not change and the particle number is preserved.

2, The lattice symmetry.

3, The spin symmetry. Starting from the definitions of spin operators.

$$S^{\alpha}_{i} = \frac{1}{2} \sum_{\sigma\sigma'} c^{+}_{i\sigma} \sigma^{\alpha} c^{+}_{i\sigma'} \quad \text{and} \quad S^{\alpha} = \sum_{i} S^{\alpha}_{i} \quad \text{with} \quad \alpha = x, y, z \tag{2.2}$$

S^{α}_{i} and S^{α} are respectively the local and total spin operators, $S = (S^{x}, S^{y}, S^{z})$. σ^{α} $= (\sigma^{x}, \sigma^{y}, \sigma^{z})$ are the Pauli matrices with

$$\sigma^{x} = \begin{pmatrix} 0 & 1 \\ 1 & 0 \end{pmatrix}, \quad \sigma^{y} = \begin{pmatrix} 0 & -i \\ i & 0 \end{pmatrix}, \quad \sigma^{z} = \begin{pmatrix} 1 & 0 \\ 0 & 1 \end{pmatrix} \tag{2.3}$$

The Hubbard Hamiltonian commutes with the global ones, thus exhibiting a $SU(2)$ symmetry due to the formation of a $SU(2)$ algebra of these operators. One has $[S^{x}, S^{y}] = iS^{z}$. The eigenvalues of S^{2} are $S(S+1)$ with S known as the total spin of eigenstate.

4, The particle-hole symmetry, one of the important features of the Hubbard model,

is considered here for a bipartite lattice structure. Lots of relatively attractive phenomena such as Mott insulator, antiferromagnetic order, etc. appear when studying the Hubbard model at half-filling. We therefore rewrite the Hubbard Hamiltonian at half-filling with $\mu = 0$.

$$H = -t \sum_{\langle i,j\rangle\sigma} (c^+_{i\sigma} c_{j\sigma} + h.c) + U \sum_i (n_{i\uparrow} - \frac{1}{2})(n_{i\downarrow} - \frac{1}{2}). \tag{2.4}$$

One then introduces new operators which exchange the role of creation and annihilation operators [69]

$$c^+_{i\sigma} \longrightarrow d_{i\sigma} = (-1)^i c^+_{i\sigma} \quad \text{and} \quad c_{i\sigma} \longrightarrow d^+_{i\sigma} = (-1)^i c_{i\sigma}. \tag{2.5}$$

The factor $(-1)^i$ becomes $+1$ if i is in one sublattice and -1 for i belonging to the other. Using the particle-hole transformations in Eq. (2.5), one gets

$$d^+_{i\sigma} d_{i\sigma} = 1 - c^+_{i\sigma} c_{i\sigma}. \tag{2.6}$$

The nearest-neighbor hopping term of Eq. (2.4) is then rewritten in the new operators

$$c^+_{i\sigma} c_{j\sigma} + c^+_{j\sigma} c_{i\sigma} = (-1)^{i+j} d_{i\sigma} d^+_{j\sigma} + (-1)^{i+j} d_{j\sigma} d^+_{i\sigma} = d^+_{i\sigma} d_{j\sigma} + d^+_{j\sigma} d_{i\sigma}. \tag{2.7}$$

It is apparent that the hopping term takes exactly the same form in term of the new operators d as it did in term of the old operators c. Therefore, this term is unchanged under the particle-hole symmetry. Similarly, the Hubbard term written in new operators, $(\frac{1}{2} - d^+_{i\uparrow} d_{i\uparrow})(\frac{1}{2} - d^+_{i\downarrow} d_{i\downarrow}) = (d^+_{i\uparrow} d_{i\uparrow} - \frac{1}{2})(d^+_{i\downarrow} d_{i\downarrow} - \frac{1}{2})$, is invariant. It turns out that the Hubbard Hamiltonian under the particle-hole transformations is completely equivalent to the initial Hubbard Hamiltonian which is expressed as

$$H' = -t \sum_{\langle i,j\rangle\sigma} (d^+_{i\sigma} d_{j\sigma} + d^+_{j\sigma} d_{i\sigma}) + U \sum_i (d^+_{i\uparrow} d_{i\uparrow} - \frac{1}{2})(d^+_{i\downarrow} d_{i\downarrow} - \frac{1}{2}). \tag{2.8}$$

The particle-hole symmetry gives us information about the symmetry of the whole phase diagram of the Hubbard Hamiltonian on a bipartite lattice at half filling [69].

On the other hand, according to Lieb's theorem [70] the total net spin gets the value of $S = \frac{1}{2}|N_A - N_B|$ with N_A (N_B) being the number of sites on the A (B) sublattice and the ground state of the Hubbard Hamiltonian is unique for all U if the system is a bipartite structure and a half-filled band in the repulsive Hubbard model ($U > 0$). In the meanwhile, the ground state of this Hamiltonian has zero

angular momentum $S = 0$ for the attractive case. Note that if the U is very large, the Hubbard Hamiltonian is an effectively isotropic spin 1/2 Heisenberg antiferromagnet and the ground state is also unique and $2S =\mid N_A - N_B \mid$. Furthermore, depending on whether the two sublattices are the same size or not, Lieb's theorem suggests antiferromagnetic and ferrimagnetic orders for the Hubbard model at half-filling [65]. In addition to Lieb's theorem, there are several other theorems and their corollaries considered as rigorous results which are also constructed for the Hubbard model such as the Mermin-Wagner theorem, Nagaoka's theorem, flat-band systems, etc [65]. Generally speaking, almost all theorems are closely related to the magnetic ground state at the zero temperature.

Thanks to the inclusion of electron correlations, simplicity and rich physics the Hubbard model becomes universal. The Hubbard model can be exactly solved in one dimension with the solution of an insulating state at half-filling and a conducting state for away from the half-filling [71]. Nevertheless, there is no exact solution for this model in more than one dimension. So a variety of techniques have been exploited to address the Hubbard model, for instance, the Hartree-Fock approximation [66], exact diagonalization [72], quantum Monte Carlo calculations [73, 74], etc.

2.2 The Kane-Mele-Hubbard model

Topological states of matter have been a fertile research field in condensed matter physics [75]. The topological state is an insulator in the bulk, nevertheless it supports gapless boundary states robust to disorder [76]. The first topological states were discovered in the 1980s known as integer and fractional quantum Hall effects (QHE) in the presence of a large perpendicular magnetic field. The QHE hence yields the breaking of the time-reversal symmetry. Besides, due to the lack of the bulk local order parameter, typically in the integer QHE, the bulk is characterized by an integer topological invariant which is read off by a Chern number. The Chern number [77] corresponds to the number of stable gapless edge states and is related to the value of the Hall conductance in units of e^2/h. About more than two decades later, a new topological state of matter, or quantum spin Hall effect (QSHE) which has paved the way for a revolution in modern condensed matter physics, was described independently by Kane and Mele [78,79] in 2005 and Bernevig and Zhang [80]

in 2006, and is today called *Topological insulator*. The model proposed by Kane and Mele, known as Kane-Mele model, took into account the spin-orbit coupling (SOC) in graphene based on earlier work of Haldane [81]. The proposal by Bernevig and Zhang studied the SOC in a strained zinc-blende semiconductor. In contrast to the QHE, the QSHE is caused by the intrinsic spin-orbit interaction instead of the external magnetic field, therefore the QSHE does not break the time-reversal symmetry. Furthermore, the edge states in the QSHE are helical edge modes rather than chiral edge modes as in the QHE due to the correlation of spin with the direction of propagation [76]. The topological insulator invariant is denoted by the Z_2 invariant which is defined for a time-reversal invariant [79]. The fact that because such proposed systems have small intrinsic spin-orbit interaction, *e.g.*, about 10^{-3} (meV) for graphene, it is hard to measure experimentally the QSHE in the proposed systems. Nonetheless, the QSHE was eventually observed experimentally in a HgTe quantum well [82].

As mentioned before, some interesting physical phenomena may be caused by the interaction of electrons. Therefore we investigate in the current work the interplay of the SOC and electron-electron interaction on graphene using the Kane-Mele-Hubbard model.

We first re-visit the Kane-Mele model for the graphene honeycomb lattice whose Hamiltonian is given by

$$H_{KM} = -t \sum_{\langle i,j\rangle\sigma} (a^+_{i\sigma} b_{j\sigma} + b^+_{j\sigma} a_{i\sigma}) + i\lambda \sum_{\langle\langle i,j\rangle\rangle} \sum_{\sigma\sigma'} \upsilon_{ij} \sigma^z_{\sigma\sigma'} (a^+_{i\sigma} a_{j\sigma'} + b^+_{i\sigma} b_{j\sigma'}) \tag{2.9}$$

where $a^+_{i\sigma}$ and $b_{i\sigma}$ are creation and annihilation operators of the A and B sublattices for spin σ at site i, respectively. The first term is a sum over the nearest-neighbor sites, denoted by $\langle i,j\rangle$, which describes the nearest hopping tight-binding term. The second term describing the spin-orbit coupling, introduced by Kane and Mele, is a sum over the next-nearest-neighbor $\langle\langle i,j\rangle\rangle$. In the second term λ denotes the amplitude of the SOC, $\upsilon_{ij} = \pm 1$ depending on the orientation of the sites gives "$+$" for clockwise and "$-$" for anticlockwise. Note that the hopping from the site of the A sublattice would yield the opposite sign than the hopping from the B sublattice in the same direction. $\sigma^z_{\sigma\sigma'}$ is the Pauli matrix. In order to solve the Kane-Mele Hamiltonian (2.9), we use Fourier transformations. After substituting Eq. (1.6) to

Eq. (2.9), the Kane-Mele Hamiltonian is expressed as [83]

$$\begin{aligned} H_{KM} &= -t\sum_{\langle i,j\rangle\sigma}(a^+_{i\sigma}b_{j\sigma}+b^+_{j\sigma}a_{i\sigma}) + i\lambda\sum_{\langle\langle i,j\rangle\rangle}\sum_{\sigma\sigma'}\sigma^z_{\sigma\sigma'}(a^+_{i\sigma}a_{j\sigma'}-b^+_{i\sigma}b_{j\sigma'}) \\ &= -t\sum_{k\sigma}(\gamma_k a^+_{k\sigma}b_{k\sigma}+\gamma^*_k b^+_{k\sigma}a_{k\sigma}) + \sum_k \lambda_k(a^+_{k\uparrow}a_{k\uparrow}-a^+_{k\downarrow}a_{k\downarrow}-b^+_{k\uparrow}b_{k\uparrow}+b^+_{k\downarrow}b_{k\downarrow}) \end{aligned} \tag{2.10}$$

with $\lambda_k = 2\lambda(-\sin(\sqrt{3}ak_y) + 2\cos(\frac{3}{2}ak_x)\sin(\frac{\sqrt{3}}{2}ak_y))$ and $\gamma_k = \sum_{n=1}^{3} e^{-ik\delta_n}$. After that it is convenient to write the Hamiltonian in the form $H_{KM} = \sum_k \Psi^+_k H_{KM}(k)\Psi_k$, with

$$H_{KM}(k) = \begin{pmatrix} \lambda_k & -t\gamma_k & 0 & 0 \\ -t\gamma^*_k & -\lambda_k & 0 & 0 \\ 0 & 0 & -\lambda_k & -t\gamma_k \\ 0 & 0 & -t\gamma^*_k & \lambda_k \end{pmatrix} \tag{2.11}$$

and $\Psi^+(k) = (a^+_{k\uparrow}, b^+_{k\uparrow}, a^+_{k\downarrow}, b^+_{k\downarrow})$. By diagonalizing the 4×4 matrix of $H_{KM}(k)$, one gets indeed the eigenvalues $E(k) = \pm\sqrt{|t\gamma_k|^2+\lambda^2_k}$. Figure 2.1 exhibits the single-particle energy spectra and their corresponding DOS of the graphene honeycomb lattice obtained from the Kane-Mele Hamiltonian for several values of λ/t. At first sight, the single-particle energy spectra are mirror symmetric, therefore both the particle-hole symmetry and the time-reversal symmetry are preserved for all values of λ/t [78, 79, 83, 84]. As $\lambda = 0t$, the upper band and lower band cross each other at the K point, it coincides with the result obtained from the nearest-neighbor hopping TB model. It means that the gapless Dirac spectrum is recovered at the K points. As $0t < \lambda < (1/(3\sqrt{3}))t$, a gap at the K point opens and increases linearly with the increase of the SOC. The distance between two peaks in the DOS is equivalent to that between the conduction and valence bands at the M point. When $\lambda \geq (1/(3\sqrt{3}))t$, the gap remains constant [83] with the size $2t$, however the gap position shifts from the K point to the M point. The position of the peaks in the DOS moves far away from zero energy with the increase of the spin-orbit coupling. Noticeably, as shown in Figure 2.1, at $\lambda = 0.5t$ one observes a pair of *armchair* points, named p_a, in the DOS where the energy position of these two points coincides with that of the conduction band and the valence band at the K point. The distance between these two points increases linearly in terms of λ/t corresponding to the linear increase of the gap at K point.

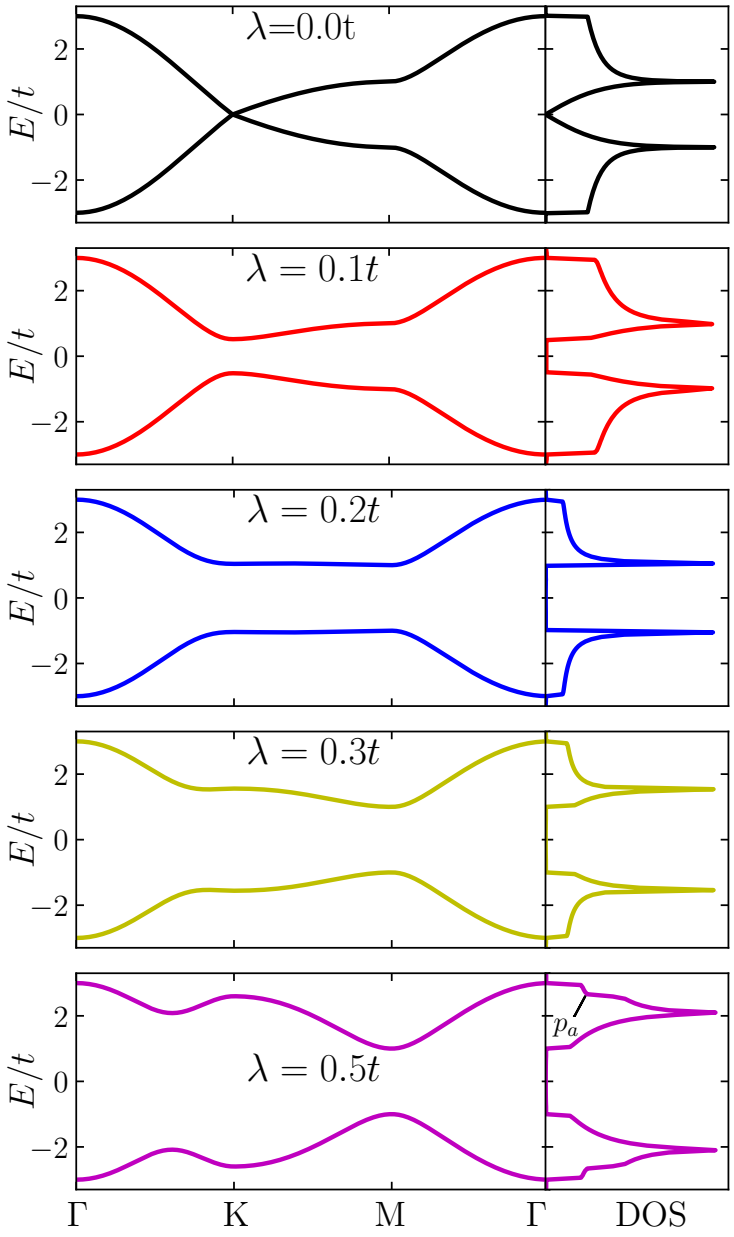

Figure 2.1: Single-particle energy spectra (left) and corresponding DOS (right) for the graphene honeycomb lattice with some values of λ/t obtained from the Kane-Mele model.

At low energy, the spin-orbit term H_{SO} can be expressed as $H_{SO} = \Delta_{SO}\Psi^{+}(q)\sigma^{z}\tau^{z}s^{z}\Psi(q)$ with the eigenvalues $E(q) = \pm\sqrt{(\hbar v_F q)^2 + \Delta_{SO}^2}$ [78], where σ^z, τ^z, s^z are the Pauli matrices representing the states on the A (B) sublattice, at the K (K') points and the spin of electron, respectively, and $\Delta_{SO} = 3\sqrt{3}\lambda$. Noticeably, the term $\sigma^{z}\tau^{z}s^{z}$ is invariant under both the parity and the time-reversal symmetry. At the K points, one finds $|E(q = K)| = \Delta_{SO}$ rather than $|E(q = K)| = 0$ as in the case of zero spin-orbit coupling. As a result, the bulk graphene is gapped and the gap size at K

points equals to $2\Delta_{SO}$ [78] as shown in Figure 2.1. It can be seen that the band gap produced in the presence of the SOC is spin dependent and has opposite sign at the K and K' points [85], indicating the difference between the anomalous topological insulator with the SOC and the ordinary topological state.

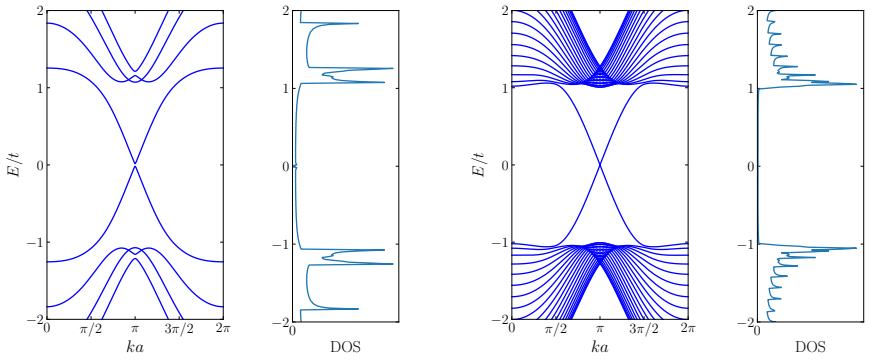

(a) $N = 4$ and $\lambda = 0.2t$ (b) $N = 20$ and $\lambda = 0.2t$

Figure 2.2: Energy band structure (left) and DOS (right) of the zigzag GNRs for $N = 4$ (a) and $N = 20$ (b), respectively, at $\lambda = 0.2t$ obtained from the Kane-Mele model.

In contrast, the opening gap depends rigorously on the width (N) of the zigzag GNRs. A small gap is only found at half-filling where the Fermi energy is at the Dirac point in the case of even N, *e.g.*, $N = 4$, and it decays exponentially with further increasing the width, shown in Figure 2.2(a) and 2.2(b), while no gap is produced for all odd values of N [86, 87]. The reason for that is due to the breaking of one of the sublattice translational invariances at the boundaries for an even N, leading to the finite interedge hopping between the two edge states. Nevertheless, the sublattice translational invariance symmetry is preserved for an odd N [87]. As mentioned, a zero-energy flat band corresponding to the edge states in the zigzag GNRs is localized in the interval of $2\pi/3 \leq ka \leq 4\pi/3$ without the SOC. Meanwhile, the energy band structure for large N intersects at $ka = \pi$ with the SOC. More interestingly, the edge states are spin-filtered, giving rise to the helical edge states, in which electrons with opposite spin carry currents in opposite direction along the same edge. For armchair GNRs, in spite of no edge state in the zero SOC case, the spin-filtered edge states also appear in the presence of the spin-orbit interaction [78, 85, 88] and two energy bands cross at $ka = 0$ in the semiconducting armchair GNRs. On the contrary, the valence band and the conduction band are split, indicating a finite gap for the armchair GNRs with metallic behavior. This gap induced by the SOC has the tendency to drop with the increase of the width of the armchair GNRs

[86]. It can be concluded that the spin-orbit coupling drives graphene into a two-dimensional topological insulator. It gives rise to a gap in the bulk and a nonzero spin Hall in relation to the helical states in the gapless edge that are protected against perturbations by the time-reversal symmetry. According to Kane and Mele [78], the topological insulator state is insensitive to weak interactions and disorder.

Now by adding the Hubbard term into the Kane-Mele model one gets the Kane-Mele-Hubbard model with its Hamiltonian

$$\begin{aligned} H_{KMH} =& H_{KM} + U\sum_{i}(n_{i\uparrow}-\frac{1}{2})(n_{i\downarrow}-\frac{1}{2}) \\ =& -t\sum_{\langle i,j\rangle\sigma}(a^{+}_{i\sigma}b_{j\sigma}+b^{+}_{j\sigma}a_{i\sigma}) + i\lambda\sum_{\langle\langle i,j\rangle\rangle}\sum_{\sigma\sigma'}\upsilon_{ij}\sigma^{z}_{\sigma\sigma'}(a^{+}_{i\sigma}a_{j\sigma'}+b^{+}_{i\sigma}b_{j\sigma'}) \\ &+ U\sum_{i}(n_{i\uparrow}-\frac{1}{2})(n_{i\downarrow}-\frac{1}{2}). \end{aligned} \tag{2.12}$$

This model was first proposed by S. Rachel et al. [83] and studied using a slave-rotor mean-field theory, and then other techniques have been utilized such as Quantum Monte Carlo simulations [89], the cellular dynamical mean-field theory (CDMFT) [90], a variational cluster approach [91], and the density-matrix renormalization group [92]. While the Hubbard term respects the $SU(2)$ spin symmetry, the SOC reduces the $SU(2)$ spin symmetry down to a U(1) symmetry and lattice symmetry C_6 to C_3. Nevertheless, the time-reversal symmetry is preserved [79].

2.3 The mean-field theory

To address the complicated problems related to the interaction of particles in which the motion of the individual particle depends on the position of all the others, the mean-field theory (MFT) can allow us to study such systems in a more convenient way [93]. This approximation actually reduces the many-body problem to a one-particle problem. Correspondingly, the interaction part in the Hamiltonian can be treated more easily. Moreover, the MFT can be realized in the real space with a big system for all shapes and it is flexible. In addition, it offers the simplest way to treat the many-body problem and is considered as a starting point for more elaborate calculations. The idea of the approximation is first to assume that the full wave function may be decoupled and represented as a product of single-particle wave functions [94]. After putting this idea into the Schrödinger equation, in the

end every individual particle is moving in the mean-field built up by the other ones. Let's now apply this idea to the Hubbard term: $H_U = U\sum_i (n_{i\uparrow} - 1/2)(n_{i\downarrow} - 1/2)$. First, the number operator $n_{i\sigma}$ is expressed as an average value plus a deviation

$$n_{i\uparrow} = \langle n_{i\uparrow}\rangle + (n_{i\uparrow} - \langle n_{i\uparrow}\rangle) = \langle n_{i\uparrow}\rangle + \delta_{i\uparrow} \tag{2.13}$$

$$n_{i\downarrow} = \langle n_{i\downarrow}\rangle + (n_{i\downarrow} - \langle n_{i\downarrow}\rangle) = \langle n_{i\downarrow}\rangle + \delta_{i\downarrow}. \tag{2.14}$$

Using these expressions, one gets

$$n_{i\uparrow}n_{i\downarrow} = \langle n_{i\downarrow}\rangle n_{i\uparrow} + \langle n_{i\uparrow}\rangle n_{i\downarrow} - \langle n_{i\uparrow}\rangle\langle n_{i\downarrow}\rangle + \delta_{i\uparrow}\delta_{i\downarrow}. \tag{2.15}$$

Eq. (2.15) shows that the spin-up electrons at site i interact with the average density of spin-down electrons and similarly the spin-down electrons at site i interact with the average density of spin-up electrons. Then substituting Eq. (2.15) into the Hubbard term and neglecting the correlation fluctuation $\delta_{i\uparrow}\delta_{i\downarrow}$, the Hubbard term reads

$$H_U^{MF} = U\sum_i \langle n_{i\downarrow}\rangle n_{i\uparrow} + \langle n_{i\uparrow}\rangle n_{i\downarrow} - \langle n_{i\uparrow}\rangle\langle n_{i\downarrow}\rangle - \frac{1}{2}(n_{i\uparrow} + n_{i\downarrow}) + \frac{1}{4}. \tag{2.16}$$

As a consequence, the mean-field Hubbard Hamiltonian only contains single-particle operators. Hence the initial many-body problem has been reduced to a single-particle problem, resulting in an easy diagonalization of the Hamiltonian. It is important to note that such mean-field approximation shows the Hartree term in which the mean-field Hubbard term is only written for the z component of the spin moment. This is the most commonly applied way to examine the magnetic properties of a system [26,28,95–97]. Nevertheless, the magnetic moment can be in favor of the xy-plane rather than the z-direction in the presence of the spin-orbit coupling [98]. To include the x (y) component of the spin moment the Fock term should be represented together with the Hartree term in the Hubbard Hamiltonian. By using Wick's theorem, the operators can be decoupled by forming creation-annihilation pairs as follows

$$\begin{aligned} n_{i\uparrow}n_{i\downarrow} =& c^+_{i\uparrow}c_{i\uparrow}c^+_{i\downarrow}c_{i\downarrow} \\ \rightarrow& \langle c^+_{i\downarrow}c_{i\downarrow}\rangle c^+_{i\uparrow}c_{i\uparrow} + \langle c^+_{i\uparrow}c_{i\uparrow}\rangle c^+_{i\downarrow}c_{i\downarrow} - \langle c^+_{i\uparrow}c_{i\uparrow}\rangle\langle c^+_{i\downarrow}c_{i\downarrow}\rangle \\ & - \langle c^+_{i\downarrow}c_{i\uparrow}\rangle c^+_{i\uparrow}c_{i\downarrow} - \langle c^+_{i\uparrow}c_{i\downarrow}\rangle c^+_{i\downarrow}c_{i\uparrow} + \langle c^+_{i\uparrow}c_{i\downarrow}\rangle\langle c^+_{i\downarrow}c_{i\uparrow}\rangle \\ =& \langle n_{i\downarrow}\rangle n_{i\uparrow} + \langle n_{i\uparrow}\rangle n_{i\downarrow} - \langle n_{i\uparrow}\rangle\langle n_{i\downarrow}\rangle - \langle S^-_i\rangle S^+_i - \langle S^+_i\rangle S^-_i + \langle\, S^+_i\rangle\langle S^-_i\rangle \end{aligned} \tag{2.17}$$

here $n_{i\uparrow} = c^+_{i\uparrow}c_{i\uparrow}$, $n_{i\downarrow} = c^+_{i\downarrow}c_{i\downarrow}$, $S^+_i = c^+_{i\uparrow}c_{i\downarrow}$ and $S^-_i = c^+_{i\downarrow}c_{i\uparrow}$. Therefore, the Hubbard term within the Hartree-Fock approximation is given by

$$\begin{aligned} H_U^{HF} =& H_U^H + H_U^F \\ =& U\sum_i \langle n_{i\downarrow}\rangle n_{i\uparrow} + \langle n_{i\uparrow}\rangle n_{i\downarrow} - \langle n_{i\uparrow}\rangle\langle n_{i\downarrow}\rangle - \langle S_i^-\rangle S_i^+ - \langle S_i^+\rangle S_i^- + \langle\ S_i^+\rangle\langle S_i^-\rangle \\ & - \frac{1}{2}(n_{i\uparrow} + n_{i\downarrow}) + \frac{1}{4}. \end{aligned} \tag{2.18}$$

From the computational point of view, from Eq. (2.16) the diagonal elements of the Hubbard Hamiltonian matrix now depend on the unknown parameters $\langle n_{i\uparrow}\rangle$ and $\langle n_{i\downarrow}\rangle$. This problem can be solved by the self-consistent algorithm, as shown in Figure 2.3. At the first step, one needs to provide initial values for the unknown parameters which can be chosen randomly to get a good solution. The initial values are plugged in the Hamiltonian matrix and the iterative calculation is started. At each cycle, the Hamiltonian matrix is diagonalized to get eigenvalues and eigenvectors which are used to compute new spin densities $\langle n_{i\uparrow}\rangle$ and $\langle n_{i\downarrow}\rangle$. These new spin densities are then used as the initial values for the next iteration. The procedure is repeated until satisfying convergence condition of the self-consistency, it means that $|A^{s+1} - A^s| < \epsilon$ (A denotes for the spin densities), with s is the index of the self-consistent cycle and ϵ is a small number (usually chosen $\epsilon = 10^{-6}$).

At half-filling and zero temperature, these spin densities are computed from the eigenstates ($\psi_i(E)$) of the Hamitonian as follows [99]

$$\langle n_{i\uparrow}\rangle = \sum_{E<E_F} \psi_i^*(E)\psi_i(E) \quad \text{and} \quad \langle n_{i\downarrow}\rangle = \sum_{E<E_F} \psi_{i+N}^*(E)\psi_{i+N}(E) \tag{2.19}$$

and

$$\langle S_i^+\rangle = \sum_{E<E_F} \psi_i^*(E)\psi_{i+N}(E) \quad \text{and} \quad \langle S_i^-\rangle = \sum_{E<E_F} \psi_{i+N}^*(E)\psi_i(E) \tag{2.20}$$

where E_F is the Fermi energy. To reach the self-consistency it is helpful to use a linear mixing method, $A_{in}^{s+1} = pA_{out}^s + (1-p)A_{out}^{s-1}$, p is the mixing coefficient. After accomplishing the self-consistency, we can calculate the local magnetic moments in the x, y, and z directions as [99]

$$M_i^x = \frac{\langle S_i^+\rangle + \langle S_i^-\rangle}{2} \tag{2.21}$$

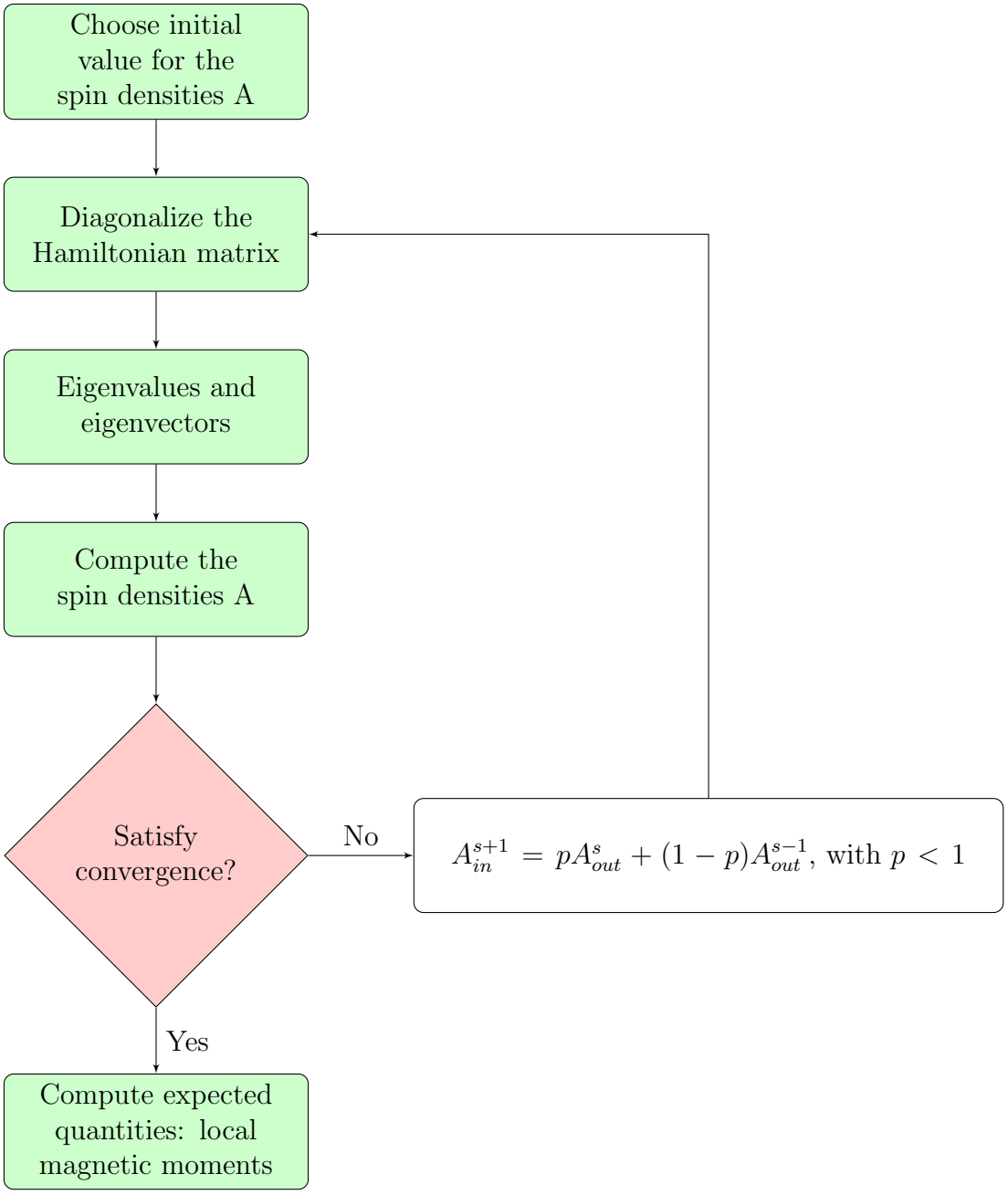

Figure 2.3: Algorithm of the self-consistent calculation (*this scheme is reproduced based on Ref. [96]).*

$$M_i^y = \frac{\langle S_i^+ \rangle - \langle S_i^- \rangle}{2j} \tag{2.22}$$

$$M_i^z = \frac{\langle n_{i\uparrow} \rangle - \langle n_{i\downarrow} \rangle}{2}. \tag{2.23}$$

Now applying the Hartree-Fock mean-field approximation into the KMH model for the graphene honeycomb lattice at half-filling and zero temperature. The KMH

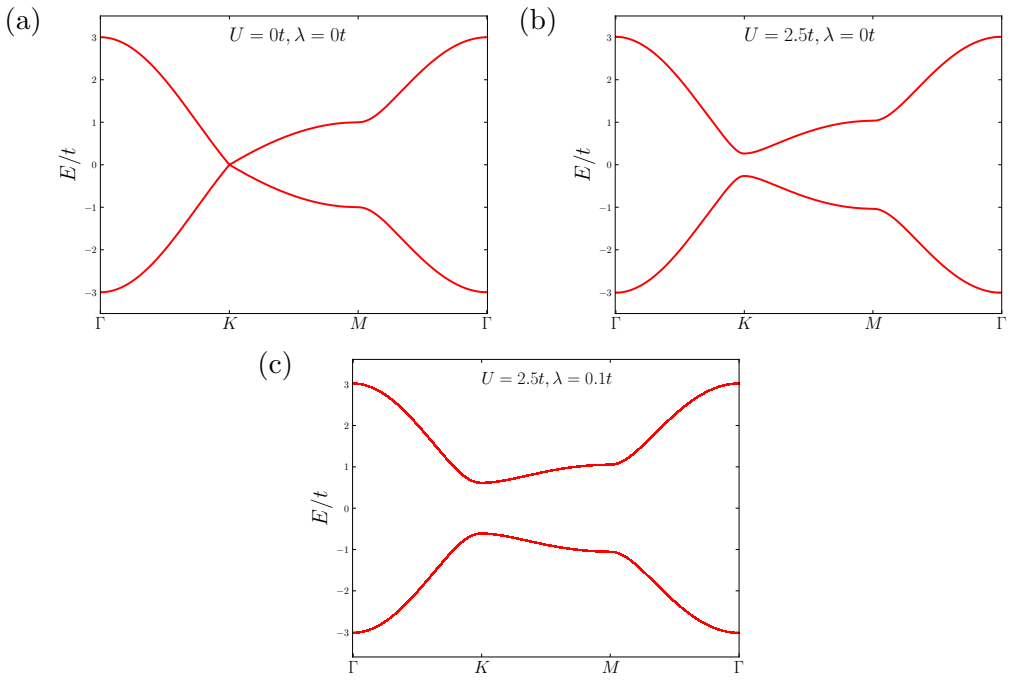

Figure 2.4: Single-particle energy spectra of the graphene honeycomb lattice using the Kane-Mele-Hubbard model within the Hartree-Fock mean-field approximation for (a) $U = 0$, $\lambda = 0$, (b) $U = 2.5t$, $\lambda = 0$, (c) $U = 2.5t$, $\lambda = 0.1t$.

Hamiltonian within the mean-field theory reads

$$\begin{aligned} H_{KMH}^{HF} =& -t \sum_{\langle i,j\rangle\sigma} (a_{i\sigma}^{+} b_{j\sigma} + b_{j\sigma}^{+} a_{i\sigma}) + i\lambda \sum_{\langle\langle i,j\rangle\rangle} \sum_{\sigma\sigma'} v_{ij} \sigma_{\sigma\sigma'}^{z} (a_{i\sigma}^{+} a_{j\sigma'} + b_{i\sigma}^{+} b_{j\sigma'}) \\ &+ U \sum_{i} \langle n_{i\downarrow}\rangle n_{i\uparrow} + \langle n_{i\uparrow}\rangle n_{i\downarrow} - \langle n_{i\uparrow}\rangle\langle n_{i\downarrow}\rangle - \langle S_i^{-}\rangle S_i^{+} - \langle S_i^{+}\rangle S_i^{-} + \langle\, S_i^{+}\rangle\langle S_i^{-}\rangle \\ &- \frac{1}{2}(n_{i\uparrow} + n_{i\downarrow}) + \frac{1}{4}. \end{aligned} \tag{2.24}$$

To be convenient, one first writes the Kane-Mele-Hubbard Hamiltonian (2.24) in k-space by using the Fourier transformations Eq. (1.6)

$$\begin{aligned} H_{KMH}^{HF} =& \sum_{k\sigma} (a_{k\sigma}^{+} b_{k\sigma}(-t\gamma_k) + b_{k\sigma}^{+} a_{k\sigma}(-t\gamma_k^{*})) + \sum_{k} \lambda_k (a_{k\uparrow}^{+} a_{k\uparrow} - a_{k\downarrow}^{+} a_{k\downarrow} - b_{k\uparrow}^{+} b_{k\uparrow} + b_{k\downarrow}^{+} b_{k\downarrow}) \\ &+ \frac{U}{N} \sum_{k} \langle n_{k\downarrow}\rangle n_{k\uparrow} + \langle n_{k\uparrow}\rangle n_{k\downarrow} - \langle n_{k\uparrow}\rangle\langle n_{k\downarrow}\rangle - \langle S_k^{-}\rangle S_k^{+} - \langle S_k^{+}\rangle S_k^{-} + \langle\, S_k^{+}\rangle\langle S_k^{-}\rangle \\ &- \frac{1}{2}(n_{k\uparrow} + n_{k\downarrow}) + \frac{1}{4}, \end{aligned} \tag{2.25}$$

under the form of matrices: $H^{HF}_{KMH} = \sum_k \Psi^+_k H^{HF}_{KMH}(k)\Psi_k$ with

$$H^{HF}_{KMH}(k) = \begin{pmatrix} \lambda_k + a & -t\gamma_k & -\frac{U}{N}\sum_k\langle S^-_{ak}\rangle & 0 \\ -t\gamma^*_k & -\lambda_k + b & 0 & -\frac{U}{N}\sum_k\langle S^-_{bk}\rangle \\ -\frac{U}{N}\sum_k\langle S^+_{ak}\rangle & 0 & -\lambda_k + c & -t\gamma_k \\ 0 & -\frac{U}{N}\sum_k\langle S^+_{bk}\rangle & -t\gamma^*_k & \lambda_k + d \end{pmatrix} \tag{2.26}$$

with

$$a = \frac{U}{N}\sum_k\langle n_{ak\downarrow}\rangle - \frac{U}{2}, \quad b = \frac{U}{N}\sum_k\langle n_{bk\downarrow}\rangle - \frac{U}{2},$$
$$c = \frac{U}{N}\sum_k\langle n_{ak\uparrow}\rangle - \frac{U}{2}, \quad d = \frac{U}{N}\sum_k\langle n_{bk\uparrow}\rangle - \frac{U}{2},$$

$$\lambda_k = 2\lambda(-\sin(\sqrt{3}ak_y) + 2\cos(\frac{3}{2}ak_x)\sin(\frac{\sqrt{3}}{2}ak_y)),$$
$$\gamma_k = \sum_{n=1}^{3} e^{-ik\delta_n}.$$

Let

$$m = \frac{1}{2N}\sum_k(\langle n_{ak\uparrow}\rangle - \langle n_{ak\downarrow}\rangle).$$

At half-filling,

$$\frac{1}{N}\sum_k\langle n_{ak\uparrow}\rangle = \frac{1}{N}\sum_k\langle n_{bk\downarrow}\rangle = (\frac{1}{2} + m),$$
$$\frac{1}{N}\sum_k\langle n_{ak\downarrow}\rangle = \frac{1}{N}\sum_k\langle n_{bk\uparrow}\rangle = (\frac{1}{2} - m),$$
$$n = \frac{1}{N}\sum_k\langle S^{\pm}_{ak}\rangle = -\frac{1}{N}\sum_k\langle S^{\pm}_{bk}\rangle.$$

Then substituting into the Hamiltonian matrix (2.26), one gets the energy dispersion after the diagonalization of the Hamiltonian matrix

$$E(k) = \pm\sqrt{-t^2\gamma_k^2 + (\lambda_k - Um)^2 - U^2n^2}. \tag{2.27}$$

Figure 2.4 shows the single-particle energy spectra of the graphene honeycomb lattice using the Hartree-Fock mean-field KMH approximation for different values of U and λ. At $\lambda = 0$, if U is zero the energy dispersion $E(k)$, $E(k) = \pm t\gamma_k$, reduces to the

nearest-neighbor hopping TB model. Therefore single-particle energy spectrum in Figure 2.4(a) is gapless. When the electron-electron interaction is involved, $U = 2.5t$, a bulk gap at the K point opens within the mean-field approximation, Figure 2.4(b). Meanwhile, the bulk gap is still gapless at $U = 2.5t$ within the QMC simulations [98]. Turning on the SOC, *i.e.*, $\lambda = 0.1t$, the bulk gap is observed in both with and without the Hubbard interaction U. Figure 2.4(c) indicates that the bulk gap in the presence of both $U = 2.5t$ and $\lambda = 0.1t$ is bigger than that for zero SOC (Figure 2.4(b)) or for zero Hubbard interaction (Figure 2.1). Generally, the bulk gap of graphene depends simultaneously on the SOC interaction and Hubbard interaction [100, 101] which will be discussed in detail in the next chapter. Furthermore, for all cases considered the conduction band and valence band are mirror symmetric, *i.e.*, $E(k) = -E(-k)$. This implies that the time-reversal symmetry is not broken under the impact of the electron-electron and spin-orbit interactions at the mean-field theory.

To conclude, in this chapter we have briefly introduced the models and the mean-field approximation used to study the magnetism and transport properties in graphene. Besides, some important physical quantities were also reviewed.

Chapter 3

Magnetism in graphene nanoflakes

Contents

3.1 Review: Magnetism in graphene 31

3.2 Phase diagram 35

3.3 Magnetism in graphene nanoflakes 40

As is well known, graphene is a gapless semi-metal with no magnetic properties, however it becomes a magnetic material in some ways. This chapter will begin with a review of magnetism in graphene. Subsequently, we will show the numerical results obtained from the Hubbard Hamiltonian and the Kane-Mele-Hubbard Hamiltonian within the mean-field approximation. We first re-plot and discuss the phase diagram of the infinite graphene without and with the spin-orbit coupling at the mean-field level and then make a comparison with other works. The remaining part of this chapter presents the findings in relation to the intrinsic magnetism in the zigzag graphene nanoflakes. Two types of geometries, including hexagonal and diamond shapes, with various sizes are studied. In addition to the robust influence of the edge termination, the geometry and the size also have a significant impact on the edge magnetic properties of a nano-scale graphene system.

Partial results of this chapter are presented in our paper [102] in which we investigate the single-band Hubbard model on an infinite graphene honeycomb lattice. The aim of our paper is to provide a detailed comparison between the results obtained from the mean-field theory and those obtained from sophisticated methods including the dynamical mean-field theory and quantum Monte Carlo simulations by computing ground-state energy, single-particle gap, double occupancy, staggered magnetization and single-particle spectra. At the mean-field level local moments cannot be generated without breaking the $SU(2)$ spin symmetry. The dynamical mean-field theory is found to be very accurate in the Dirac semi-metallic phase because the dynamical

mean-field theory takes into account local temporal fluctuations and captures the local moment formation in the paramagnetic phase. However, the impact of spin fluctuations on the single-particle spectral function is only visible in the lattice quantum Monte Carlo approach. Therefore, the presentation in this chapter is different from the paper, the reader can visit our paper to obtain more information.

3.1 Review: Magnetism in graphene

The magnetism of carbon-based materials is one of the extremely intriguing research domains which can lead to a breakthrough in spintronics because it originates from the π-electrons. Typically, investigations have shown an interestingly unconventional magnetization at the graphene system on both experiment and theory.

From the experimental point of view: Although atomically precise edge graphene is rather difficult to synthesize and bare graphene termination is very sensitive to chemical modification, several recent efforts supported the idea of intrinsic magnetism, *i.e.*, edge magnetism, in graphene nanostructures. Tao et al. [64] used the tunneling spectroscopy measurement to provide a strong signal of magnetization in the chiral GNRs at $T = 7K$ synthesized by unzipping carbon nanotubes. That work shows that the finite energy gap was measured for various chiral GNRs with a range of chiral angle $3.7° < \theta < 16.1°$ (θ is the angle between the zigzag edge direction and the actual edge orientation), for example, a gap approximately $23.8 \pm 3.2\ meV$ for (8,1) GNR (with (n, m) expressing the edge orientation of GNRs in graphene lattice coordinates). Noticeably, as pointed out in Ref. [27] an electronic bandgap of about $0.2 - 0.3$ eV, measured by STM, is revealed for narrow zigzag GNRs with the width N less than 7, indicating a signature of interaction-induced spin ordering along the edges. The gap opening associated with the edge magnetism is predicted by various theories, such as the mean-field theory [103], the density functional theory [63], and quantum Monte Carlo simulations [73]. Additionally, Magda et al. [27] detected a transition from semiconductor to metal, which can be identified as the antiferromagnetic-ferromagnetic transition, corresponding to the bandgap changing from finite value to zero upon increasing graphene nanoribbon width. The findings in that work also demonstrated the stability of the edge magnetic order even at room temperature. Differential conductance (dI/dV) spectrum obtained by using STM displayed the energy splittings of $\Delta^0 = 1.5$ eV and $\Delta^1 = 1.9$ eV between the

two occupied states and the unoccupied one, respectively, for 6-zigzag GNR [17], providing not only the existence of edge-localized states but also edge magnetic order. The experimental findings in that article are in good agreement with theoretical results where the DFT calculation unveiled the energy splittings $\Delta^0 = 1.4$ eV and $\Delta^1 = 1.7$ eV in the energy band structure of the zigzag GNR. Furthermore, several other studies were carried out in order to provide important additional evidence about the presence of the magnetic edge states, for instance, using jointly Near-edge x-ray absorption fine structure (NEXAFS) and Electron-spin resonance (ESR) on few-layer-graphene nanoribbons synthesized by chemical vapor deposition [104], using four-pulse DEER (Double electron-electron resonance) on Nitronyl nitroxide-radical-functionalized GNRs [105] and others [106–108]. Evidently, most experimental observations have only been successful on the GNRs. Meanwhile, many reports fabricated successfully GNFs from different approaches with various shapes and sizes [109–114], but there has not been still any clear evidence about the intrinsic magnetic moment in graphene quantum dots yet. Nevertheless, according to a recent experimental work [115], the purely Curie-like paramagnetism with the magnetic moment of 1.2 μ_B at $2K$ was obtained on substantially pristine edge graphene quantum dots which have the average diameter of 2.04 nm and average height of approximately 0.52 nm (implying that most of the graphene quantum dots are mono and bi-layer). In spite of the relatively small detected value, that result may be considered as an experimental proof for the possibility of the spontaneous magnetism in graphene quantum dots.

From the theoretical point of view: The majority of computational studies are realized within the DFT because it is able to provide information about the spin-resolved density of states of the system. Albeit so, another approach used widely is the single-band Hubbard model for π-electrons. According to the single-band Hubbard model, both local and total magnetic moments depend exclusively on the strength of the on-site Coulomb interaction U. At half-filling, the graphene honeycomb lattice is in the semimetallic state with weak Coulomb interaction U. An expected phase transition to an insulator state with antiferromagnetic order is introduced upon increasing the strength of U. The threshold value of U where occurs a semimetal-antiferromagnetic transition is very sensitive such that its magnitude can be influenced easily by external conditions [116] or intrinsic and Rashba spin-orbit coupling (Rashba SOC arise from the electric field or interaction with a substrate [79]) [91, 98]. Since the π-electron is localized at the carbon atoms on the zigzag edge, while no such lo-

calization is expected for the armchair edge, the intrinsic magnetism on the edges can only be induced by the edge-localized states. Spins localized at the zigzag edge align in parallel if they belong to the same sublattice. In contrast, the spins become antiparallel if they belong to different sublattices. Such intrinsic magnetization on the edges has been extensively studied on the GNRs by the MFT, DFT or QMC calculations [63, 73, 103, 117]. As indicated, with arbitrary non-zero Coulomb interaction U, the magnetic moment on a zigzag edge of pristine GNRs displays ferromagnetism at the intra-edge and antiferromagnetism at the inter-edge. Its amplitude decays sharply from edge sites to inner sites for the weak Coulomb energy. Similar phenomena have been also predicted in the GNFs. Remarkably, the GNFs can be semiconducting with a finite bandgap even in the absence of Coulomb interaction. The amplitude of such gap declines once increasing the size and vanishes at limit large size which has been demonstrated both experimentally [118] and theoretically [39]. Together with the quantum confinement effect, the magnetization in the GNFs therefore points out the sensitive dependence on the size, shape and edge orientation.

Since graphene is a bipartite lattice, for real space there are two counting rules [103]; consisting of the benzenoid graph theory and Lieb's theorem, that can be applied to predict a few characteristics including the magnetic properties in a finite graphene system. The benzenoid graph theory can provide directly the number of zero-energy states η of the nearest-neighbor TB Hamiltonian which is equal to $\eta = 2\alpha - N$, where N is the total number of sites and α provides the maximum possible number of non-adjacent sites. Nevertheless, this theory does not estimate clearly the spin alignment in the zero-energy states. Lieb's theorem determines the total spin of the ground state in the bipartite system described by the Hubbard Hamiltonian, $S = |N_A - N_B|/2$ with N_A and N_B are the number of sites in the A and B sublattices, respectively. As a consequence, the GNFs with arbitrary shapes can be classified into two types, that are, nanoflakes with sublattice balance ($N_A = N_B$) like hexagon, diamond and nanoflakes with sublattice imbalance ($N_A \neq N_B$) such as triangle, pentagon. For the former, because of the balance of the graphene sublattices the total spin $S = 0$ results in either a non-magnetic solution or a fully compensated intrinsic AF solution [119–121]. In the case of nanoflakes with sublattice imbalance, the total spin is nonzero, thus there exists a finite magnetic moment in the system [122].

In addition, the significant effect of the vacancies, doping, strain or edge modification on the magnetism of graphene systems has been extensively investigated. It is theoretically demonstrated that vacancies emerging in GNRs can govern not only their bandgap but also magnetic state. Because of the imbalance of sublattices, vacancies introduced into the armchair GNRs reveal interesting magnetization and the magnetic moment values depend on the number of vacancies and distance of vacancies [19, 123]. Topsakai et al. [124] predicted that metallization, as well as magnetization, can be induced by repeating vacancies or divacancies in non-magnetic semiconducting nanoribbons due to the spin polarization of local defect states. In that work, the change from the AF ground state to the ferrimagnetic state in semiconducting zigzag GNRs was observed in the presence of vacancy defects. Using the determinant QMC simulations, G. Yang et al. [125] provided a way to control magnetism at room temperature by tunning the strain. The increase of the strain along the zigzag GNRs can enhance the edge magnetization and a ferromagnetic-like behavior with a proper strain may be produced at a relatively weak Coulomb interaction. In analogy to the strained GNRs, these behaviors were also found in the strained graphene quantum dots [119, 126]. Investigations also suggested that carrier-doped graphene can tune the magnetic ordering [120, 121, 127]. Particularly, according to Ref. [120], the emergence of inter-edge ferromagnetic coupling on the hexagonal graphene quantum dot with $N = 54$, without the on-site Coulomb interaction, is due to a single hole or electron doping in which the total magnetic moment calculated for the hole doping case is larger. While the competition between the on-site Coulomb interaction and carrier doping gives rise to a complex magnetic phase diagram: including the intrinsic AF, fully polarized ferromagnetic and mixed phase. In contrast, the edge modification like reconstruction, hydrogen passivation has been predicted to suppress magnetism in the GNFs [115, 128–130]. Furthermore, in spite of the small intrinsic spin-orbit coupling, its effect on the magnetism has been studied using various methods such as QMC simulations [84, 89, 98], slave-rotor MFT [83, 131], variational cluster approach (VCA) [101], renormalization group [87] or other approaches [90, 132]. A large number of investigations exhibit the interplay between spin-orbit coupling and electron-electron interactions. In addition to the emergence of topological insulating phase, the magnetization is in favor of in-plane rather than being in out-of-plane in the presence of the SOC.

To sum up, it is clear that the variety of GNFs with different shapes and sizes was studied. However, the systematic investigation to point out the onset of magnetiza-

tion on GNFs with sublattice balance from the small to large GNFs has been scarce. In what follows, we therefore will describe in detail the Hubbard model within the MFT to gain insight the intrinsic magnetism on the GNFs for hexagonal and diamond shapes. Besides, we also analyze the phase diagram in the presence of the intrinsic SOC at the Hartree-Fock mean-field level which has not been shown yet.

3.2 Phase diagram

We first revisit the phase diagram of the graphene honeycomb lattice in the absence of the SOC within the mean-field Hubbard approximation at half-filling and zero temperature. Unlike the two dimensional square lattice (in the case of the nearest-neighbor hopping considered), where the ground state is an AF state at even an infinitesimally small onsite Coulomb energy U [133], the transition to the AF phase occurs at a finite U for the honeycomb lattice, named critical value with the abbreviation of U_c. This is considered to be a consequence of the vanishing density of states at zero energy. The value of U_c is found at $2.23t$ [134] at the mean-field level. As shown in Figure 3.1(a), we find a so-called Mott-Hubbard transition point at the U_c where the graphene undergoes a phase transition from the gapless semi-metal (SM) to the antiferromagnetically ordered insulator. The staggered magnetization M_s increases as U/t beyond the critical point U_c/t. The single-particle gap Δ_{sp} is shown in the inset of Figure 3.1. It opens and climbs up nearly linear with respect to U/t in the magnetic phase. One considers the dispersion energy $E(k)$ at K point. In particular, γ_K in Eq. (2.27) is zero and Eq. (2.27) reads, $E(K) = \pm U|M_s|$ with $m = M_s$ (without spin-orbit coupling). The single-particle gap can be calculated as follows

$$\Delta_{sp} = 2U|M_s|. \tag{3.1}$$

We see explicitly the direct relation between the staggered magnetization and single-particle gap within the mean-field approximation by Eq. (3.1) where a finite staggered magnetization gives rise to a finite gap. These findings are in excellent agreement with the established literature [95, 134]. In comparison with other numerical approaches, the results generally show higher critical values U_c than $2.23t$. We performed a study of the single-band Hubbard model on the graphene honeycomb lattice to compare the mean-field results with the elaborate DMFT and lattice QMC [102]. Due to the inclusion of quantum fluctuation in the DMFT, the transition shifts to

the value of $U_c/t \approx 3.7$ (within DMFT + NRG) and $U_c/t \approx 3.5$ (within DMFT + QMC) close to the result obtained from the projective auxiliary field QMC simulations, namely $U_c/t \approx 3.78$ (see Ref. [102] for details)[1]. This value $U_c \approx 3.78t$ was also provided by the pinning field approach for QMC of Assaad et al. [135]. In addition, Sorella et al. found a $U_c/t = 4.5 \pm 0.5$ [134] for clusters containing up to 648 sites, a more accurate estimate $U_c/t = 3.869 \pm 0.013$ [136] for much lager clusters containing up to 2592 sites using QMC. Other QMC approaches found a $U_c/t \approx 3.6$ by Furukawa et al. [137] and a $U_c/t \approx 5$ by Paiva et al. [138]. The two-particle self-consistent approach [139] to the honeycomb lattice reported a $U_c/t = 3.79 \pm 0.01$ which is quite close to the value using large-scale QMC. A $U_c/t \sim 3.8$ is given using the functional renormalization group [140]. Moreover, a finite $U_c/t \sim 3.3$ was also calculated using cluster DMFT combined with continuous-time QMC simulations given by Wu et al. [52]. Another value $U_c = 3.7t$ was obtained from the two-site dynamical impurity approximation [141]. In short, although the critical point U_c is sensitive to different numerical approaches which may be subject to different errors, the *true* value is unique and the antiferromagnetic phase exists at strong interaction.

With regard to the presence of the intrinsic SOC λ, Figure 3.1(b) plots the ground-state phase diagram using the Kane-Mele-Hubbard model within the Hartree-Fock mean-field approach. At first glance, there are three phases, including the gapless semi-metal (SM), the topological band insulator (TBI) and antiferromagnetic insulator (AFI), instead of two phases as in the case of zero SOC. The transition points U_c dramatically increase when the intrinsic SOC λ increases. The reason for that is the opening of a finite bandgap by the SOC without the electron-electron interaction [91], see Figure 2.2(a). In detail, the SM phase, which only exists at $\lambda = 0$, is characterized by $\Delta_{sp} = 0$ and is non-magnetic as mentioned before. A transition from the SM phase to the TBI phase occurs for arbitrary non-zero λ. In contrast to the SM phase, the TBI phase has $\Delta_{sp} > 0$, see the inset of Figure 3.2, and the system still remains non-magnetic. Both the SM and TBI phases are stable against weak interaction. Nonetheless, a transition to the AFI phase occurs at strong interaction. While the out-of-plane magnetic moment is prioritized for development at $\lambda = 0$, indicating the Néel type, the finite intrinsic SOC suppresses the parallel orientation of magnetic moment to the z axis. Concurrently, it drives the moment into a xy-plane AF order. This phenomenon has been confirmed by the slave-rotor

[1]Numerical calculations are performed by our colleagues: Fakher F. Assaad (QMC), Robert Peters (DMFT + NRG) and Nayuta Takemori (DMFT + QMC)

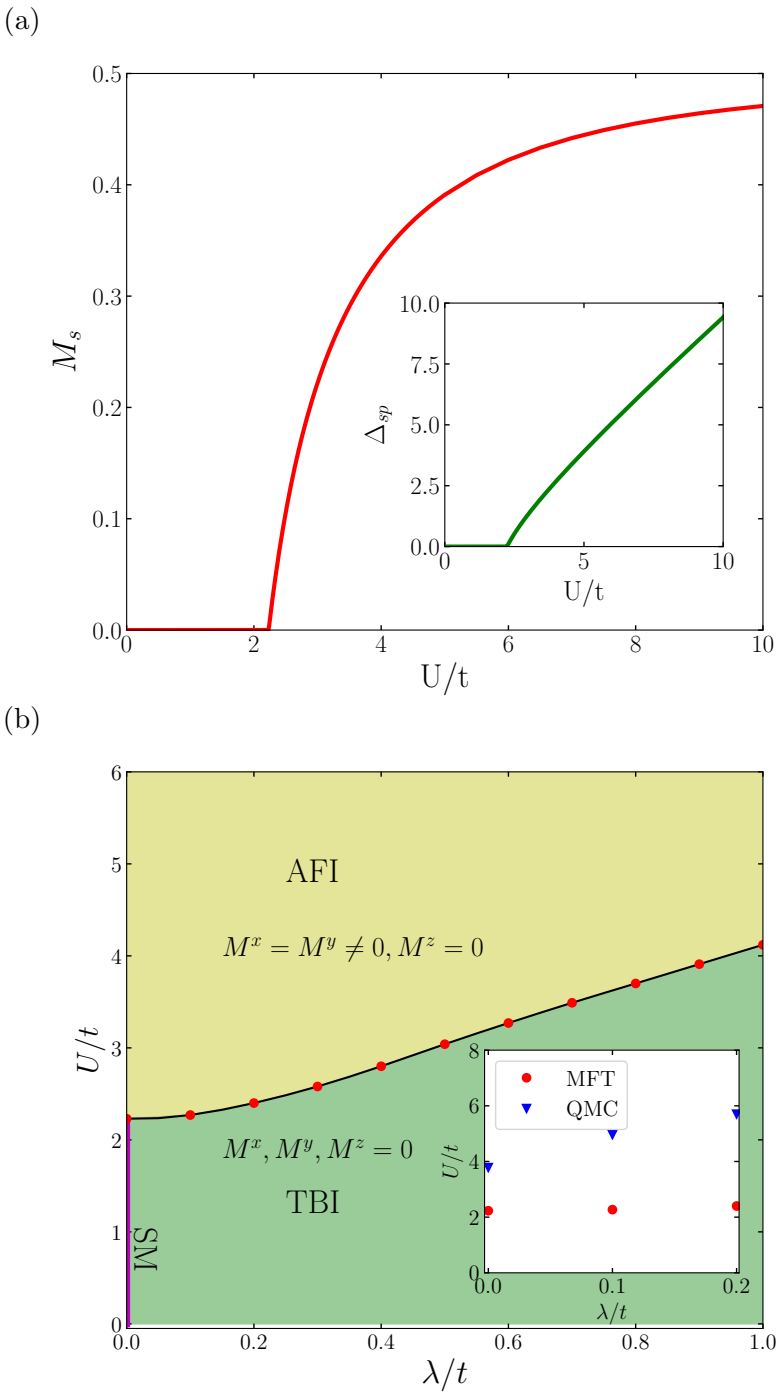

Figure 3.1: (a) Staggered magnetization and single-particle gap (in the inset) Δ_{sp} versus U/t within the mean-field Hubbard approximation. (b) Phase diagram using the KMH model at the mean-field level. The inset displays the data obtained from the MFT (red circles) and QMC (blue triangles).

theory [83, 131], QMC [84, 98], CDMFT (cellular dynamical mean-field theory) [90], VCA (variational cluster approach) [91], and pseudofermion functional renormalization group [131]. To be explicit, Figure 3.2 denotes the staggered magnetization as

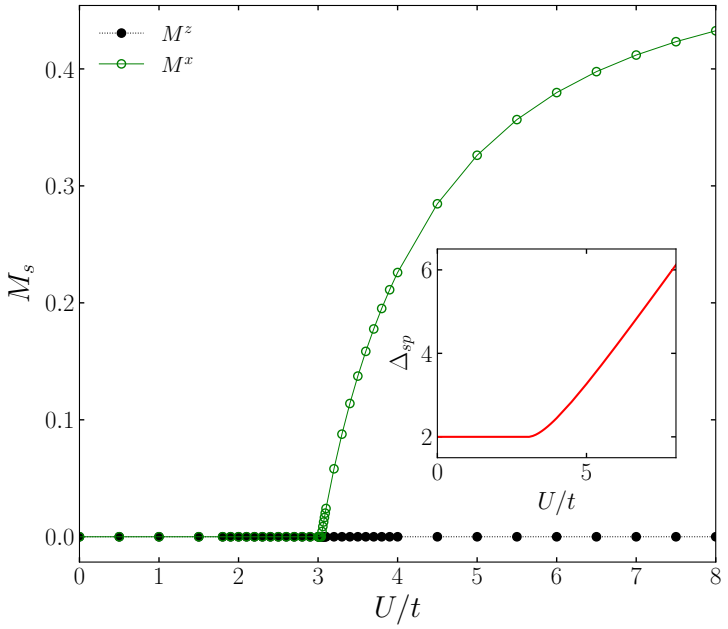

Figure 3.2: Staggered magnetization and single-particle gap (in the inset) as a function of U/t with the intrinsic SOC $\lambda = 0.5t$.

a function of U/t for $\lambda = 0.5t$. The phase transition takes place at $U_c \simeq 3.04t$ where the in-plane magnetization M^x turns on and then increases with U/t beyond the U_c/t, while M^z remains at zero. The inset of Figure 3.2 gives information about the single-particle gap Δ_{sp} for $\lambda = 0.5t$ in which the Δ_{sp} linearly increases with respect to U/t in the AFI state. As expected, a finite gap is observed and is not sensitive to the Coulomb interaction U in the topological insulator phase.

In comparison, the inset of the Figure 3.1(b) also shows the $U - \lambda$ phase diagram of the KMH model using the Hartree-Fock MFT (red circles) and QMC simulations (blue triangles) [2]. Not only does the $U - \lambda$ phase diagram obtained from the QMC simulations introduce the presence of such three phases but also indicates the increase of transition boundary line with respect to λ/t which has the similar effect as in the MFT for the range of λ/t considered. However, the critical value U_c corresponding to each λ for the QMC simulations is higher than that for the MFT, for example $U_c \approx 5.7t$ for the QMC simulations and $U_c \approx 2.4t$ for the MFT at $\lambda = 0.2t$. In addition, the QMC simulations also show that the magnetic ordering in the AFI phase only occurs in the transverse spin directions at $\lambda > 0$ which is exhibited in our calculations as well. Similar results have been found in other works

[2]The data obtained from QMC simulations are computed by Martin Hohenadler (this result was published in Ref. [98])

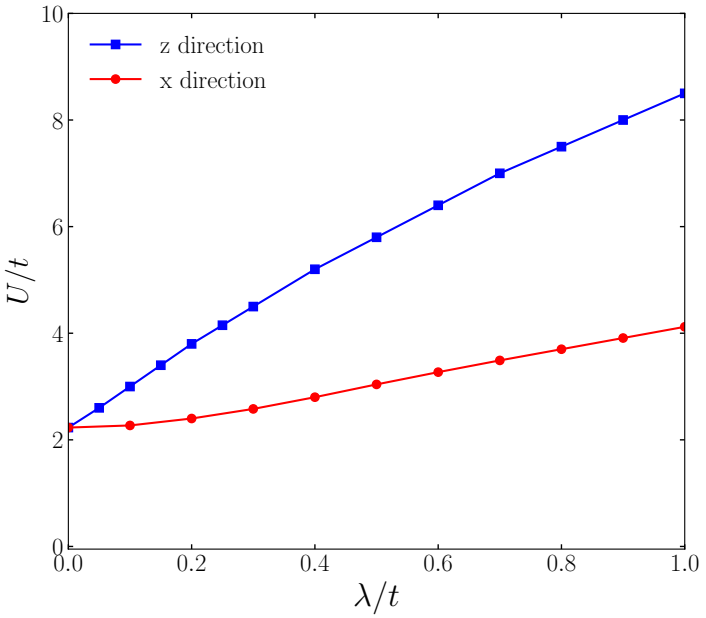

Figure 3.3: Phase diagram using KMH model in the mean-field approximation with the AF moment in z direction (blue line) and x direction (red line).

where U_c increases with increasing λ [84, 91]. Such a phase diagram was calculated by S. Rachel et al. [83] using the Hartree-Fock approximation. However, the slope of the transition boundary line in that study are much higher compared with our results as well as the results obtained from more sophisticated methods, typically $U_c \simeq 2.23t - 8.55t$ in Ref. [83], while $U_c \simeq 2.23t - 4.12t$ corresponding to $\lambda = 0 - 1t$ in our calculation. This difference results from the choice of the quantization axis. To clarify, the phase diagram for the infinite graphene in Ref. [83] is reproduced and plotted in Figure 3.3 where the z axis is chosen as a quantization axis. For $\lambda = 0$, the mean-field critical point U_c is approximately $2.23t$ for any quantization axis. Since the $SU(2)$ symmetry is not broken the magnetization direction is not important [141]. For $\lambda \neq 0$, one sees the difference of the transition boundary lines between the z direction (blue line) and the x direction (red line). According to the QMC calculations, the magnetic moment prefers to lie in the in-plane direction, it thus requires stronger interaction for the stability of the antiferromagnetic state in the out-of-plane direction. The value of U_c in this case is overestimated, while the U_c in x direction is underestimated. As a result, the slope of the blue line is higher than the slope of the red line. Therefore, our results are more accurate than those published in [83] within Hartree-Fock approximation.

To conclude, our results show that the phase transition strongly depends on the intrinsic SOC and the onsite Coulomb energy using the KMH model at the Hartree-Fock mean-field level which has not been reported yet. By comparing to other literature, we find a good agreement with previous works.

3.3 Magnetism in graphene nanoflakes

In what follows, we evaluate the intrinsic magnetism on graphene nanoflakes with two types of geometries: hexagon and diamond with various sizes. The magnetic moment for each site i (or local magnetic moment at site i) is computed as $m_i = \langle s_i^z \rangle = (\langle n_{i\uparrow} \rangle - \langle n_{i\downarrow} \rangle)/2$ and the total magnetic moment $S = \sum_i m_i$. For the antiferromagnetic phase, we calculate the staggered magnetization,

$$M_s = \frac{1}{N} \sum_i (-1)^i \langle s_i^z \rangle, \tag{3.2}$$

where N is the number of carbon atoms on a graphene nanoflake. The factor $(-1)^i$ gets $+$ for i belonging the A sublattice and $-$ for the other. The bigger M_s is, the stronger the antiferromagnetic phase is. Resembling the infinite graphene, the GNFs are here non-magnetic without taking into consideration the electron-electron interaction. The onset of magnetization on the GNFs therefore only occurs at a finite value of U, called U_c as well, where there is a transition from the paramagnetic (PM) to the antiferromagnetic (AF) phase. The value of U_c/t is sensitive to the edge termination, the size as well as the geometry of the GNFs [28, 119, 122, 142]. As indicated by J. Viana Gomes et al. [119] the armchair GNFs do not support any magnetic structure for the value of $U < U_c^{bulk}$ ($\simeq 2.23t$). In addition, that study confirmed that the presence of the zigzag termination gives rise to the reduction of U_c/t. Hence, the origin of the edge magnetization is believed to be due to the presence of the edge states [95, 120, 121]. Therefore, we neglect the armchair GNFs in the current work.

As shown in Figure 3.4, U_c is suppressed to approximately zero upon increasing the size of the nanoflakes for both geometries. Particularly, the value of U_c decreases from $U_c \simeq 2.2t$ ($U_c \simeq 1.51t$) to a tiny $U_c > 0t$ corresponding to $N = 24$ ($N = 30$) to $N = 1350$ ($N = 286$) sites for the hexagonal (diamond) nanoflakes at the mean-field level. For a large enough size, the magnetization on the zigzag edges

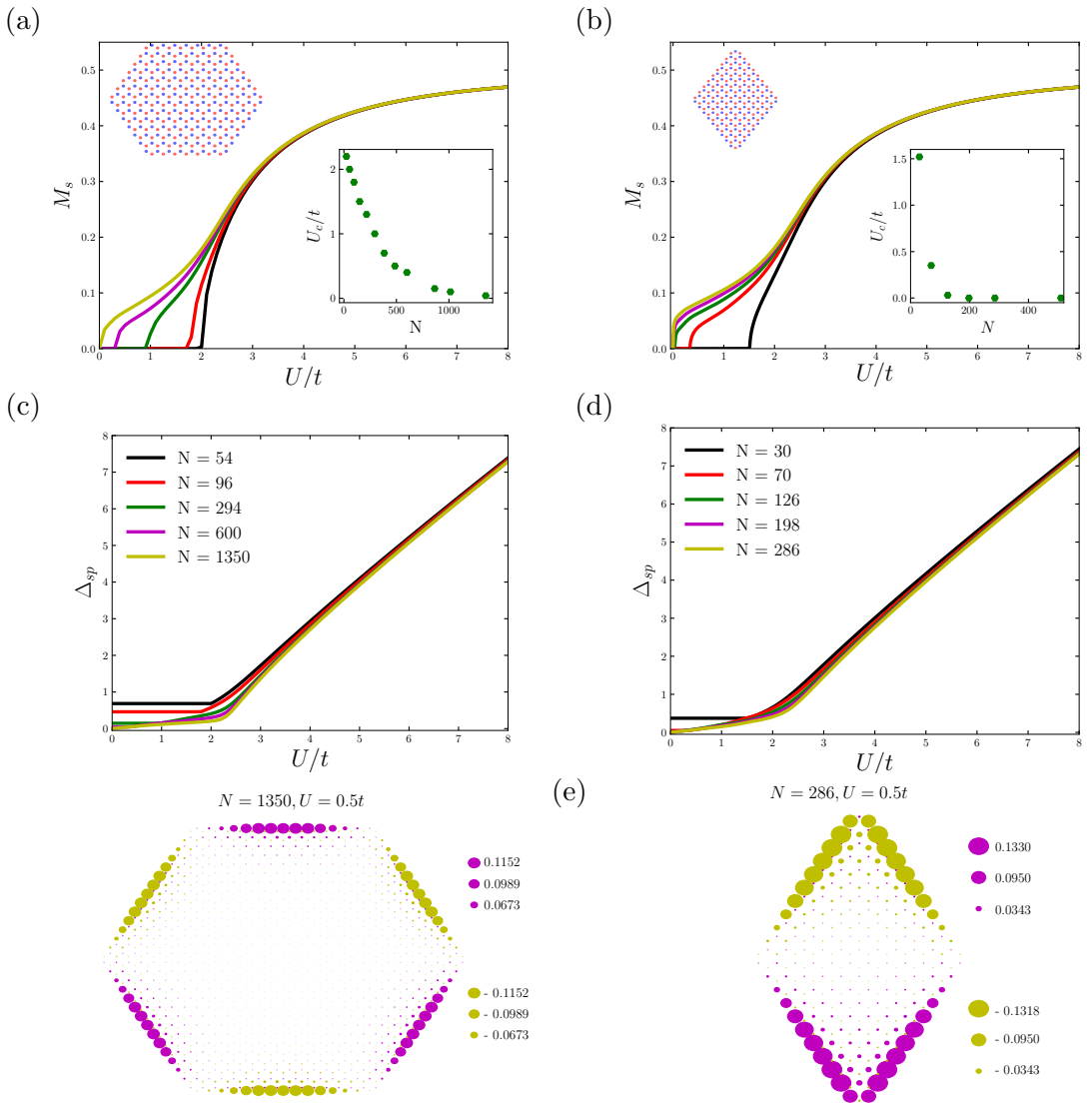

Figure 3.4: Staggered magnetization M_s on the edges (a, b) and single-particle gap Δ_{sp} (c, d) versus U/t, and local magnetic moments (e, f) for hexagonal and diamond GNFs, respectively. Pink circles denote the magnitude of spin-up densities, while yellow ones are proportional to the magnitude of spin-down densities. The insets of figures (a) and (b) display the dependence of U_c/t on the number of sites on each nanoflake.

of GNFs is developed at a tiny U_c, like square-shaped nanoflakes [119] and GNRs [26, 143]. The reduction of U_c is also shown for the hexagonal GNFs within the DMFT where U_c decrease from $\simeq 3.1t$ ($N = 54$) to $\simeq 2.0t$ ($N = 150$) [39]. The origin of this reduction has been controversial. Among the reasons the amplitude of the quantum confinement gap Δ_{sp} without the on-site Coulomb energy [39] can be considered as the main reason. Typically, Figure 3.4(c) and 3.4(d) display that the gap Δ_{sp} is inversely proportional to the increase of the nanoflake size. The

gap of diamond nanoflakes is smaller than that of hexagonal nanoflakes, as a result the transition point in the diamond nanoflakes shifts to a smaller value. Another explanation, suggested by S. Ganguly et al. [130], is in relation to the armchair bond density, defined as $\rho = N_{arm}/N_t$ with N_{arm} (N_t) being the number of the armchair (total) bonds along the edges, on the edges, because the armchair defect gives rise to the damage to magnetization. ρ decreases with increasing nanoflake size, thus resulting in the favor of the AF order in larger nanoflakes rather than in smaller ones at the weak interaction. Besides, changing the shape from the hexagon to the diamond yields a significant reduction of ρ, so the diamond nanoflakes require weaker interaction to trigger the antiferromagnetism than the hexagonal nanoflakes. In other words, the number of carbon atoms on the edges determines directly the value of U_c. In addition, since the number of sites on an edge of the diamond nanoflakes is much larger than that of the hexagonal nanoflakes with the relatively equivalent number of sites on whole nanoflakes the amplitude of magnetization on the diamond GNFs is bigger for the range of $U_c < U < U_c^{bulk}$. However, the amplitude of magnetization remains constant being independent on the size as well as the geometry for the intermediate and strong U/t. The reason for that is the magnitude of the gap being almost equal for all sizes and geometries at the same U/t.

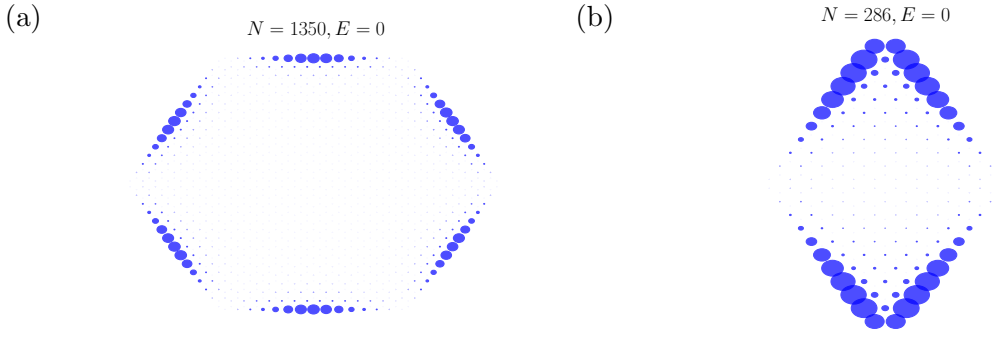

Figure 3.5: Local density of states (LDOS) at each site of the hexagonal (a) and diamond (b) nanoflakes for the energy of $E = 0$ eV. The area of each blue circle is proportional to the amplitude of the LDOS.

In the AF state, with U/t close to U_c/t the magnetic moment on the zigzag edges largely contributes to the magnetization of the nanoflakes and the magnetic moment decreases sharply as moving toward the center of the nanoflakes, see Figure 3.4(e) and 3.4(f). The spin-polarization would occur at all sites of the nanoflakes with strong enough electron-electron interaction, *i.e.*, $U > 2.23t$. The amplitude of the local magnetic moments at the edge sites is substantially larger than that at others. This is a consequence of the reduction of the number of hopping channels for the edge

sites [120–122] compared with the inner sites of the nanoflakes. Remarkably, for the hexagonal GNFs, the magnetic moments on all sites at a given edge align ferromagnetically because all of the carbon atoms belong to the same graphene sublattice. Meanwhile, the magnetic moments on the neighboring edges have antiferromagnetic alignment due to two adjacent edges connected by an armchair defect. Similar findings were reported for small hexagonal nanoflakes, $N = 54$ [39] and $N = 96$ [95]. For the diamond GNFs, we can assume that a diamond nanoflake is constructed by two triangular shapes which are connected by two armchair defects. In analogy to the square nanoflakes or the nanoribbons, if the upper triangular part exhibits parallel spin moments at two edges, the other shows antiparallel spin moments. The net total magnetic moment S for both geometries equals to zero and this result is in accordance with Lieb's theorem for the case of sublattice balance. Furthermore, since there exists the armchair bond at the junction of the edges for both geometries the local magnetic moment increases far away from the armchair defect. As a consequence, the largest magnetic moment resides at the middle site of the edge for the hexagonal nanoflakes. The maximum value of local magnetic moment dwells in the edge sites close to the corners for the diamond nanoflakes. Such local magnetic moment distribution may be due to the electron distribution along the zigzag edges. To be clear, we plot the local density of states (LDOS), the LDOS at site i, $LDOS = (-1/\pi)\Im G_{ii}(r)$ with $G_{ii}(r)$ being the retarded Green's function, for the hexagonal and diamond GNFs at the zero energy. Figure 3.5 reveals that the electron distribution at each site is similar to the distribution of local magnetic moment where the electron densities of the nanoflakes congregate principally on the zigzag edges. These densities dwindle sharply as going toward the bulk sites and close to the armchair defects. Such electron distribution for the hexagonal and triangular nanoflakes was also pointed out in Ref. [144].

To sum up, the electron-electron interaction encoded by U takes responsibility for switching on the magnetism in graphene. Depending on the characteristic of each graphene system, it requires different coupling which is a function of the geometry, edge and size. These findings are in good agreement with previous works [120, 122, 130].

Chapter 4

The non-equilibrium Green's function method

Contents

4.1 Introduction 44

4.2 Setup transport problem 46

4.3 The non-equilibrium Green's function formalism 48

4.3.1 Basic formulas 48

4.3.2 The current of charge carriers 51

4.4 Wide-band limit approximation 54

Due to the difficulties in solving exactly transport issues of a complicated many-body system, approximation methods are required. Recently, a common approach to deal with the transport problems is based on the Green's function, typically the non-equilibrium Green's function formalism. Not only does it allow to describe various systems but one can also conveniently realize computations because the main results of the non-equilibrium Green's function formalism can be summarized in a few equations. In this chapter, we review in short the important equations of the non-equilibrium Green's function formalism. Before doing that, this chapter will begin with an introduction to spin caloritronics. Then we sketch a spin-caloritronic device based on a magnetic zigzag graphene nanoflake used for studying the transport properties.

4.1 Introduction

How to cope with the increasing dissipated heat and improve the performance in electronic devices are the main challenges in the design of these devices at the nanoscale.

In this regard, a new field of study emerges, known as *spin caloritronics*, which integrates two well-established fields, namely spintronics and thermoeletronics. The former explores the spin degree of freedom of an electron and the latter can convert directly heat into electrical power and vice versa. Therefore, the spin caloritronics describes the interaction of spins with heat currents [145–148]. Thanks to this combination, the spin-caloritronic devices can bring interesting features such as miniaturization of device, recovery of waste energy, easy control of the spin current by temperature, development of an effective way for future non-dissipative information transmission and low-energy consumption technology [40], *etc.*

In general, the fundamental structure of a spin-caloritronic device requires an interface between a material with the possibility of spin-polarization and a normal metal, a semiconductor, or another spin-polarized material. When a temperature gradient is applied to a spin-polarized material, the thermally induced carrier currents flow in opposite directions via two spin channels and a spin current can be generated [40, 149, 150]. Unlike the spintronics where a spin-polarized current is generated by a bias voltage, the spin current in the spin caloritronics is induced by a temperature difference rather than by an electrical gradient. The generation of the spin current driven by the temperature gradient is in intimate relation to an effect known as the spin Seebeck effect (SSE). This effect was first observed by Uchida's group in 2008 [151]. In that work, they found a spin voltage and spin current only produced by a temperature gradient in a metallic magnet without an external field. Up to now, the SSE has been measured in many materials by the inverse spin-Hall effect such as half-metallic $La_{0.7}Sr_{0.3}MnO_3$ [152], the ferromagnetic semiconductor GaMnAs [153], the ferrimagnetic insulator $Y_3Fe_5O_{12}$ [154], antiferromagnetic Cr_2O_3 [155], MnF_2 [156], NiO [157], the magnetic insulator $LaY_2Fe_5O_{12}$ [158], and the non-magnetic semiconductor InSb [159]. Noticeably, a perfect SSE can be achieved when there is only a spin current flowing in the device, giving rise to the reduction of the heat dissipation caused by the total charge current [160].

Graphene is an ideal material for spintronic applications due to its weak spin-orbit coupling, long relaxation time and length, as mentioned in Chapter 1. A large number of studies have focused on the spin transport which is brought on by an external bias in the graphene-based spintronic devices [44,161–164]. On the other hand, albeit the pure graphene sheet shows the limitations in thermoelectric applications due to its high thermal conductivity [7], which decreases the thermoelectric efficiency, the

modified graphene offers a relatively large Seebeck coefficient in both theory [165] and experiment [166, 167]. Ouyang et al. [168] reported that the Seebeck coefficient of GNRs was found to be much higher than that of two-dimensional graphene. High thermoelectric power at high temperature was measured in graphene deposited on hBN by F. Ghahari et al. [167]. Moreover, Zeng et al. [40] found that the thermally induced spin current could be generated by applying a temperature difference between two electrodes in a magnetic zigzag GNR. From these considerations, it can result in the possibility of developing graphene-based spin caloritronics.

A variety of theoretical researches in the spin-caloritronic field have been mainly done on the GNRs with the zigzag-shaped edge [40, 169–171] due to the rich magnetic properties [103] and on the armchair GNRs [150, 172] because of its high Seebeck coefficient [173] using the first-principle calculations and the mean-field theory combined with the NEGF technique. In addition to the spin Seebeck effect, the GNR-based spin caloritronic devices exhibit other excellent properties such as spin-filtering effect, spin-Seebeck diode, giant thermal magnetoresistance, negative differential resistance effect [44, 148, 169, 172, 174, 175], *etc.* Those studies indicated that the substantial spin-up and spin-down currents flowing in opposite directions were induced by the temperature gradient without external electric bias. A pure spin current without charge current also generated in the GNR-based devices was reported [171, 176]. Recently, experimental measurements have predicted the possibility of the spin Seebeck effect in graphene [177]. Furthermore, the devices based on graphene with a perfect SSE have been still a challenge and very little attention has been paid to thermally induced spin currents in the graphene nanoflakes. Therefore, we aim to address such spin current in graphene nanoflake-based spin caloritronic devices in the present study.

4.2 Setup transport problem

Figure 4.1(a) sketches the device used to investigate the transport properties in the present work. Particularly, this device consists of a magnetic hexagonal GNF with zigzag edge and two metallic leads (*i.e.*, Au). The GNFs act as the scattering region (central part), while the left and right leads act as the source (S) and the drain (D) with different temperatures T_S and T_D, respectively. It assumes that there are no direct interactions between the source and the drain. These two leads are con-

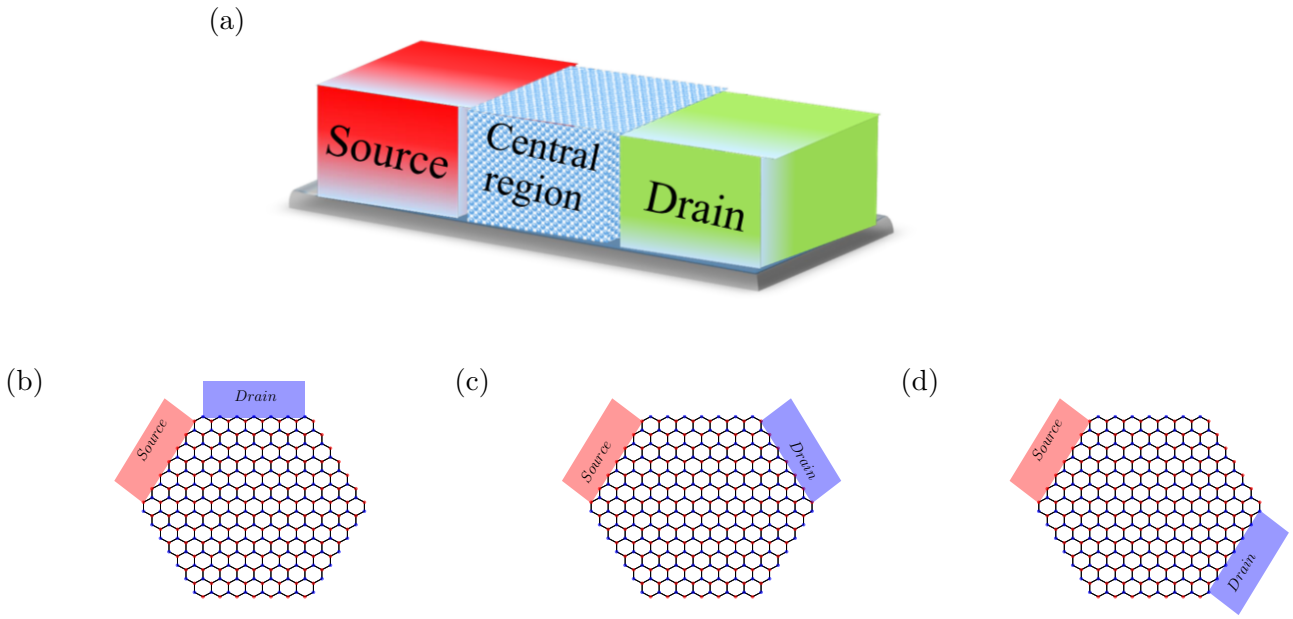

Figure 4.1: (a) The schematic configuration of a two-lead device. The contact position of leads with the edges of GNFs in three configurations: (b) *ortho*, (c) *meta* and (d) *para*.

nected with two zigzag edges of the GNFs. Depending on the contact position of the leads with the edges, there are three possible configurations denoted as *ortho* (4.1(b)), *meta* (4.1(c)) and *para* (4.1(d)), respectively. In the *ortho* and *para* configurations, the leads are connected with carbon atoms belonging to different graphene sublattices. Hence, as the magnetization is triggered the magnetic moments on the edges are antiparallel. In contrast, the leads are attached to carbon atoms of the same graphene sublattice in the *meta* configuration, so the magnetic moments become parallel. The difference among these configurations is expected to bring about interesting spin transport phenomena.

With the device proposed, the total Hamiltonian of the device is given as [178, 179]

$$
\begin{aligned}
H &= H_C + H_S + H_D + H_{SC} + H_{DC} \qquad (4.1)\\
H_C &= -t \sum_{\langle i,j\rangle\sigma} (c^+_{i\sigma} c_{j\sigma} + h.c) + U \sum_i (n_{i\uparrow} - \frac{1}{2})(n_{i\downarrow} - \frac{1}{2})\\
H_{S/D} &= \sum_{\alpha k\sigma} \epsilon_{\alpha k\sigma} d^+_{\alpha k\sigma} d_{\alpha k\sigma}\\
H_{SC/DC} &= \sum_{\alpha i k\sigma} V_{\alpha i k\sigma} c^+_{\alpha i\sigma} d_{\alpha k\sigma} + h.c
\end{aligned}
$$

where H_C describes the graphene nanoflakes with the nearest hopping and Coulomb

interaction. $H_{S/D}$ is the Hamiltonian of the source/drain with $\alpha = S/D$ and $d^{+}_{\alpha k\sigma}$ ($d_{\alpha k\sigma}$) creates (annihilates) an electron with energy $\epsilon_{\alpha k\sigma}$ in the source/drain. $H_{SC/DC}$ is the Hamiltonian for tunneling between the leads and the nanoflake with $V_{\alpha ik\sigma}$ denoting the hopping between the site i of the central region and the state k of the leads. When there is a difference in the temperatures of the leads, the system is driven out of equilibrium and therefore a current will flow through the device. The calculation of such a current is realized by the non-equilibrium Green's function formalism.

4.3 The non-equilibrium Green's function formalism

4.3.1 Basic formulas

The non-equilibrium Green's function method is an elegant and powerful computational approach for treating the transport properties in a nanoscale system. It is developed based on the quantum field theory. In the early 1960s, the initial developments of the non-equilibrium Green's function (NEGF) method were formed with the first key contributions of Martin and Schwinger [180] in the formulation of the general N-particle Green's function. The next important contributions came from Baym and Kadanoff [181] and Keldysh [182]. More remarkably, Keldysh introduced a useful diagrammatic technique for treating the Green's function in non-equilibrium systems, known as Keldysh contour, so the NEGF is sometimes known as the Keydysh formalism [183]. So far this method has been applied successfully to various nonequilibrium problems such as particles in plasmas, electrons, spins and phonons in semiconductors, superconductors, *etc*, see Ref. [184] and its cited references. Particularly, the NEGF method enables us to effectively calculate the currents, current densities, occupation numbers and spin densities in the systems including a finite bias and interactions [184]. In this section, we briefly present the NEGF formalism for a system including a central region (C) (can be a wire, molecule, quantum dot, *etc*) connected to the left and right leads acting as the source (S) and drain (D), respectively, see Figure 4.1(a). Each block in the system can be described by a corresponding Hamiltonian.

To derive the main equations in the NEGF method, we start with the definitions of Green's functions. In quantum mechanics, the single-particle Green's function $G(E)$ of a system described by a Hamiltonian H can be found from the equation

$$(E - H)G(E) = 1. \tag{4.2}$$

The solution of Eq. (4.2) gives the formal Green's function

$$G(E) = (E - H)^{-1}. \tag{4.3}$$

The retarded and advanced Green's functions are defined respectively [185]

$$G^r(E) = (E + i\eta - H)^{-1} \tag{4.4}$$

$$G^a(E) = [G^r(E)]^* = (E - i\eta - H)^{-1} \tag{4.5}$$

here η is a positive infinitesimal number. Consider now the two-terminal system above, the retarded Green's function of the whole system can be determined by solving Eq. (4.2) when replacing $G(E)$ by $G^r(E)$. Eq. (4.2) is recast under the matrix form as follows

$$((E + i\eta)I - H)G^r(E) = I \tag{4.6}$$

where I is an identity matrix. In this case $H = H_S + H_D + H_C + H_{SC} + H_{DC}$ is the total Hamiltonian of the system with $H_{S/D}$ and H_C describing the Hamiltonian of the source/drain and central region respectively, and $H_{SC/DC}$ denoting the coupling between the leads and central region. Since there are no direct interactions between the two leads the Hamiltonian H_{SD} and H^*_{SD} are zero. Here H_C is a finite matrix while the others are infinite matrices in size. We can write Eq. (4.6) in the following form

$$\begin{bmatrix} E + i\eta - H_S & -H_{SC} & 0 \\ -H^*_{SC} & E + i\eta - H_C & -H^*_{DC} \\ 0 & -H_{DC} & E + i\eta - H_D \end{bmatrix} \begin{bmatrix} G^r_S & G^r_{SC} & G^r_{SD} \\ G^r_{CS} & G^r_C & G^r_{CD} \\ G^r_{DS} & G^r_{DC} & G^r_D \end{bmatrix} = \begin{bmatrix} I_S & 0 & 0 \\ 0 & I_C & 0 \\ 0 & 0 & I_D \end{bmatrix} \tag{4.7}$$

here G^r_S and G^r_R describe the source and drain retarded Green's functions, G^r_{SC} and G^r_{RC} are the retarded Green's functions manifesting the interaction between the leads and the central region. The direct scattering between two leads is G^r_{SD} and finally G^r_C is the retarded Green's function of the central region. I_C is the identity matrix of the central region while I_S and I_D are the identity matrices of the leads.

With the aim to find G_C^r, we are only interested in the following set of three equations in Eq. (4.7)

$$\begin{aligned} (E+i\eta-H_S)G_{SC}^r - H_{SC}G_C^r &= 0 \\ -H_{SC}^*G_{SC}^r + (E+i\eta-H_C)G_C^r - H_{DC}^*G_{DC}^r &= I_C \\ -H_{DC}G_C^r + (E+i\eta-H_D)G_{DC}^r &= 0 \end{aligned} \tag{4.8}$$

Implementing simple mathematical calculations, equations above are rewritten as

$$\begin{aligned} G_{SC}^r &= (E+i\eta-H_S)^{-1}H_{SC}G_C^r \\ G_{DC}^r &= (E+i\eta-H_D)^{-1}H_{DC}G_C^r \\ (E+i\eta-H_C)G_C^r - H_{SC}^*G_{SC}^r - H_{DC}^*G_{DC}^r &= I_C \end{aligned} \tag{4.9}$$

Substituting the first and second equations into the third equation of the set of equations above, one gets

$$G_C^r = [E+i\eta-H_C-H_{SC}^*(E+i\eta-H_S)^{-1}H_{SC}-H_{DC}^*(E+i\eta-H_D)^{-1}H_{DC}]^{-1} \tag{4.10}$$

Ultimately, the retarded Green's function of the central region is found as

$$G_C^r = [E+i\eta-H_C-\Sigma_S(E)-\Sigma_D(E)]^{-1} \tag{4.11}$$

where

$$\Sigma_S(E) = H_{SC}^*g_S^rH_{SC} \tag{4.12}$$

and

$$\Sigma_D(E) = H_{DC}^*g_D^rH_{DC}. \tag{4.13}$$

Σ_S and Σ_D are the self-energies of the source and drain, respectively. g_S^r and g_D^r are the retarded surface Green's functions for the leads attached to the central region which are defined respectively

$$g_S^r = (E+i\eta-H_S)^{-1} \tag{4.14}$$

and

$$g_D^r = (E+i\eta-H_D)^{-1}. \tag{4.15}$$

Eq. (4.11) shows that the retarded Green's function G_C^r contains all information

about the electronic structure of the central region connected to the leads. Therefore, solving Eq. (4.11) plays a crucial role in the study of transport phenomena in a nanoscale system. From the computational technique, the main task for finding the solution of Eq. (4.11) revolves around the calculation of the self-energies of the leads or, more accurately, the retarded surface Green's functions $g^r_{S/D}$.

4.3.2 The current of charge carriers

As is well known, a current flows through a system when the charge carrier concentration at the source and drain is out of equilibrium caused by a bias voltage or temperature gradient. In the ballistic transport regime, this current can be treated within the so-called Landauer-Büttiker formalism which was proposed by Landauer [186] and Büttiker [187]. The current in this formalism is related to the probability of an electron to be transmitted through the system and it is given by [188, 189]

$$I = \frac{2e}{h} \int_{-\infty}^{\infty} dE T(E)(f_S(E) - f_D(E)) \tag{4.16}$$

where e is the absolute value of the electron charge, h is the Planck constant. $T(E)$ is the transmission coefficient which is the summation of transmission probabilities of electrons with energy E. $f_{S/D}(E)$ is the Fermi-Dirac distribution function for the source/drain.

$$f_{S/D}(E) = \frac{1}{1 + e^{\beta(E-\mu_{S/D})}} \tag{4.17}$$

with the chemical potential of the source/drain $\mu_{S/D}$ and β inversely proportional to temperature. In the case when the current is induced by the temperature gradient, all the temperature dependences are in the distribution functions $f_{S/D}$ while the transmission coefficient does not depend on the temperature [189].

For a small bias voltage and at low temperature around the Fermi energy E_F, the current of charge carriers through the system is mainly determined by the transmission coefficient $T(E_F)$ with [190]

$$I \sim T(E_F)(\mu_S - \mu_D). \tag{4.18}$$

It can be seen that the calculation of the current concentrates on the evaluation of the transmission coefficient. Although the Landauer-Büttiker formalism (4.16)

has proven its usefulness for the understanding of mesoscopic transport, it is not an effective tool when dealing with problems such as carriers scattering off impurities, lattice vibrations, the mutual influences of the electron and phonon subsystems on each other, *etc* [188,191]. In the meanwhile, such effects can be in general treated by the NEGF method. Moreover, in 1971 Caroli et al. [192] gave an explicit calculation of the current for a metal-insulator-metal tunneling junction to all orders in the applied bias based on the NEGF method. That paper also first provided an efficient way to compute the transmission coefficient in terms of Green's function, the so-called Caroli formula

$$T(E) = Tr(G^a \Gamma_D G^r \Gamma_S), \tag{4.19}$$

where $\Gamma_{S/D}$ denotes the interaction between the source/drain and the central region with

$$\Gamma_{S/D} = i(\Sigma_{S/D} - \Sigma^+_{S/D}). \tag{4.20}$$

Since then, the NEGF has been applied to various systems to formulate an expression for the charge current in terms of the Green's function [183, 191, 193–195]. Those reports not only reproduce the Caroli formula but also derive a Landauer-Büttiker-like formula (see detailed calculations in Refs. [183,191,193–195]). In particular, the current flowing from the source to the central region can be calculated by taking the expectation value of the rate of the occupation number operator N_S of the source [193]

$$I_S = -\frac{ie}{\hbar}\langle [H, N_S] \rangle, \tag{4.21}$$

here

$$H = \sum_i \epsilon_i c_i^+ c_i + \sum_{k,\alpha \in S,D} \epsilon_{k\alpha} d_{k\alpha}^+ d_{k\alpha} + \sum_{i,k,\alpha \in S,D} V_{k\alpha,i} c_i^+ d_{k\alpha} + h.c \tag{4.22}$$

is the Hamiltonian of the two-terminal system and

$$N_S = \sum_{k,\alpha \in S} d_{k\alpha}^+ d_{k\alpha}. \tag{4.23}$$

Where c_i^+ (c_i) creates (destroys) an electron in state i with energy ϵ_i for the central region while $d_{k\alpha}^+$ and $d_{k\alpha}$ are the creation and annihilation operators with energy $\epsilon_{k\alpha}$ for the source (S) or the drain (D), and $V_{ki}^{S,D}$ describes the coupling of an electron with a momentum state k in the lead to an atomic orbital i on the central region.

The current I_S obtained after some algebra is

$$I_S = \frac{ie}{\hbar} \sum_{k,i,\alpha \in S} (V_{k\alpha,i} \langle d^+_{k\alpha} c_i \rangle - V^*_{k\alpha,i} \langle c^+_i d_{k\alpha} \rangle). \tag{4.24}$$

Using definition of the Keldysh Green's function $G^<_{i,k\alpha}(t) \equiv i\langle d^+_{k\alpha} c_i(t) \rangle$ [183,193], one arrives at

$$I_S = \frac{e}{h} \sum_{k,i,\alpha \in S} \int \frac{dE}{2\pi} (V_{k\alpha,i} G^<_{i,k\alpha}(E) - V^*_{k\alpha,i} G^<_{k\alpha,i}(E)). \tag{4.25}$$

In the NEGF method, by introducing the Dyson equations (see Ref. [183] for details), the steady state current I across the system is determined by

$$I = \frac{ie}{h} \int dE (Tr\{[f_S(E)\Gamma_S - f_D(E)\Gamma_D](G^r - G^a)\} + Tr\{(\Gamma_S - \Gamma_D)G^<\}). \tag{4.26}$$

Applying the Dyson equations for the Green's function in the central region into Eq. (4.26) [183],

$$G^< = i f_S(E) G^r \Gamma_S G^a + i f_D(E) G^r \Gamma_D G^a \tag{4.27}$$

and

$$G^r - G^a = -i G^r (\Gamma_S + \Gamma_D) G^a. \tag{4.28}$$

One gets

$$I = \frac{2e}{h} \int_{-\infty}^{\infty} dE (f_S(E) - f_D(E)) Tr(G^a \Gamma_D G^r \Gamma_S) \tag{4.29}$$

with 2 accounting for the spin degeneracy. Note that G^r and G^a are the retarded and advanced Green's functions of the central region. Comparing Eq. (4.29) with Eq. (4.16) and together with Eq. (4.19), one can reproduce the Landauer-Büttiker formula from the non-equilibrium Green's function formalism. Consequently, the problem of the calculation of the transmission coefficient in the Landauer-Büttiker formula can be solved by the NEGF method. In analogy to Eq. (4.11), the transmission coefficient $T(E)$ can be obtained if one knows the retarded surface Green's function $g^r_{S/D}$. Because of the important role of the surface Green's function for the non-equilibrium transport problem, a general algorithm to compute them has been proposed. This algorithm is reviewed in Ref. [189] and is not introduced here. Since the DOS of the metallic leads is approximately constant near the Fermi energy, for simplicity, we apply the wide-band limit approximation in this PhD work to find the transmission coefficient as well as the retarded Green's function G^r_C. We will return to this discussion in more detail in the subsequent section.

4.4 Wide-band limit approximation

The wide-band limit method is an effective approximation employed to treat the self-energies of the leads in the nanoscale. This approximation assumes that the density of states in the leads does not affect the description of the transport in the device [196]. Concretely, the retarded self-energies $\Sigma_S(E)$ and $\Sigma_D(E)$ in the Eq. (4.11) can be split into a Hermitian and anti-Hermitian terms [193, 197]

$$\Sigma_{S,D}(E) = \Lambda_{S,D}(E) - \frac{i}{2}\Gamma_{S,D}(E), \tag{4.30}$$

where $\Lambda_{S,D}(E)$ gives rise to a shift of the orbital resonances and $\Gamma_{S,D}(E)$ describes a level broadening. The imaginary part of the self-energy $\Gamma_{S,D}(E)$ can be expressed as

$$\Gamma_{ij}^{S,D}(E) = 2\pi \sum_k V_{ki}^{S,D} V_{kj}^{*S,D} \delta(E - E_k). \tag{4.31}$$

Near the Fermi energy, $V_{ki}^{S,D}$ is generally a slowly-varying function of the momentum k [193]. We have

$$\Gamma_{ij}^{S,D}(E) \approx 2\pi V_i^{S,D} V_j^{*S,D} \sum_k \delta(E - E_k) = 2\pi V_i^{S,D} V_j^{*S,D} \rho(E) \tag{4.32}$$

where $\rho(E)$ is the DOS in the leads. The fact that the DOS is approximately constant near the Fermi energy for a metallic lead such as gold. Therefore, within the wide-band limit approximation, it assumes that Γ is an energy independent constant, *i.e*, $\Gamma_S = \Gamma_D = \Gamma$, and the level-shift Λ is neglected [197]. The self-energy then has the form

$$\Sigma_{S,D} = -\frac{i}{2}\Gamma_{S,D}. \tag{4.33}$$

It can be seen that this approximation has effectively replaced the complexity of the full self-energies at the leads by a single parameter $\Gamma_{S,D}$ [197]. Despite the simplicity, the wide-band limit approximation still captures the main physical properties and has the great advantage of yielding explicit analytic results [193]. The problem for finding the solution of the transmission coefficient $T(E)$ and the retarded Green's function G_C^r become relatively simple rather than the cumbersome calculations for the surface Green's function. The transmission coefficient within the wide-band limit approximation becomes

$$T_\sigma(E) = \Gamma^2 \sum_{ij\sigma} (G_{ij\sigma}^r(E))^* G_{ij\sigma}^r(E) \tag{4.34}$$

with i and j labelling the number of sites on the edges connected to the leads in our device. According to Valli et al. [39], the increase of Γ results in the extension of spectral features of the transmission and the increase of overall transmission. For the aim of definiteness, the value of Γ/t in this work is set to be 0.02 [39].

To conclude, Eqs. (4.11), (4.19), (4.31) and (4.29) are the main ingredients of the NEGF method often utilized to solve the transport problem in nanodevices and can be conveniently implemented on a computer. We apply them for the next investigations in this PhD thesis. From the computational point of view, the elements in the Hamiltonian matrix H_C need to be known before addressing Eq. (4.11). Therefore, the NEGF method usually combines with another method such as the density functional theory, the dynamical mean-field theory or the mean-field theory which takes responsibility for the calculation of H_C. In the current work, we choose the combination of the NEGF with the mean-field theory. The findings obtained from the approaches will be discussed in the subsequent chapter.

Chapter 5

Thermally induced spin current across a spin caloritronic device

Contents

5.1 Thermally induced spin current 57

5.2 The physical mechanism of thermally induced spin current 61

5.3 The back-gate voltage-modulated spin current 67

5.4 The charge and spin thermovoltage 73

In the following, we discuss the spin-dependent thermoelectric effects of magnetic zigzag graphene nanoflakes in the ballistic regime. The charge and spin currents across such graphene nanoflakes are computed by the Landauer-Büttiker formalism in the framework of the non-equilibrium Green's function method combined with the mean-field theory. Our obtained results exhibit that a pure spin current without charge current is generated when a temperature difference is applied. This is a consequence of the flowing of the carrier currents via the up spin and down spin in opposite directions with the same magnitude. Furthermore, the back-gate voltage effects on the thermally driven spin currents are also studied. Results show that a high spin-filtering effect can be achieved by adjusting the temperature difference, the source temperature and the back-gate voltage. In comparison with the graphene nanoribbon-based devices which require an external condition such as an external magnetic field to be active the spin current, our study just explores sublattice chirality and geometrical symmetry of the graphene nanoflakes without the external condition to attain good results. Therefore, the results in our study have not been found in literature. These results will be presented in our next article.

5.1 Thermally induced spin current

In the present work, we examine the spin-dependent current of the hexagonal zigzag graphene nanoflakes with different sizes. For the *ortho* and *para* configurations, our calculations show that the spin degeneracy of the transmission coefficient is protected (this will be discussed in the next section). This result also indicated by Valli et al. [39], which stems from the symmetry, for a small nanoflake $N = 54$. As a result, a zero current is generated in the device (without the external conditions such as substrate, gate voltage). In the meanwhile, the spin-resolved transmission coefficient is established in the *meta* configuration. Consequently, this work just concentrates on studying the spin current in the *meta* configuration. Applying a temperature gradient, $\Delta T = T_S - T_D$, the current of charge carriers via spin-up and spin-down states flows in the device estimated by the Landauer-Büttiker formula within the NEGF method combined with the mean-field theory. The value of η in Eq. (4.10) and Γ in Eq. (4.34) are chosen $10^{-2}t$ and $0.02t$ (t: the nearest hopping parameter), respectively. Further calculations that are not shown here indicate that the absolute of the thermally spin-resolved current is affected by this choice of η, while the qualitative behavior of these currents as a function of temperature is not affected by this choice. Note that the spin-orbit coupling is neglected, the mean-field approximation via Eq. (2.16) is thus used for all calculations in this investigations because the spin moments develop in the z-direction.

We first study the impact of the on-site Coulomb interaction U on the thermally induced spin current flowing in the device. Figure 5.1(a) displays the spin-resolved current as a function of U/t at the source temperature $T_S = 0.026t$ and temperature difference $\Delta T = 0.0052t$ for the hexagonal zigzag GNFs. It can be seen that the current through the device is absent when the GNFs are in the paramagnetic phase. However, we find three different behaviors in the antiferromagnetic (AF) phase: (i) The spin-up and spin-down currents induced by the temperature gradient rise up to an absolute maximum value at U_h/t. The position of U_h/t is sensitive to the size of the nanoflakes due to the instability of the U_c/t (U_c/t is the critical point of the GNFs) to the nanoflake size. Figure 5.1(b) and Table 5.1 unveil that the U_h gradually decreases, while the absolute maximum value of spin-up (spin-down) current $I_{max\uparrow(\downarrow)}$ rapidly increases by increasing of the nanoflake size up to $N = 726$ (N is the number of carbon atoms on a graphene nanoflake) for the T_S and ΔT considered here. The highest value of $I_{max\uparrow(\downarrow)}$ is found for the nanoflake of $N = 726$

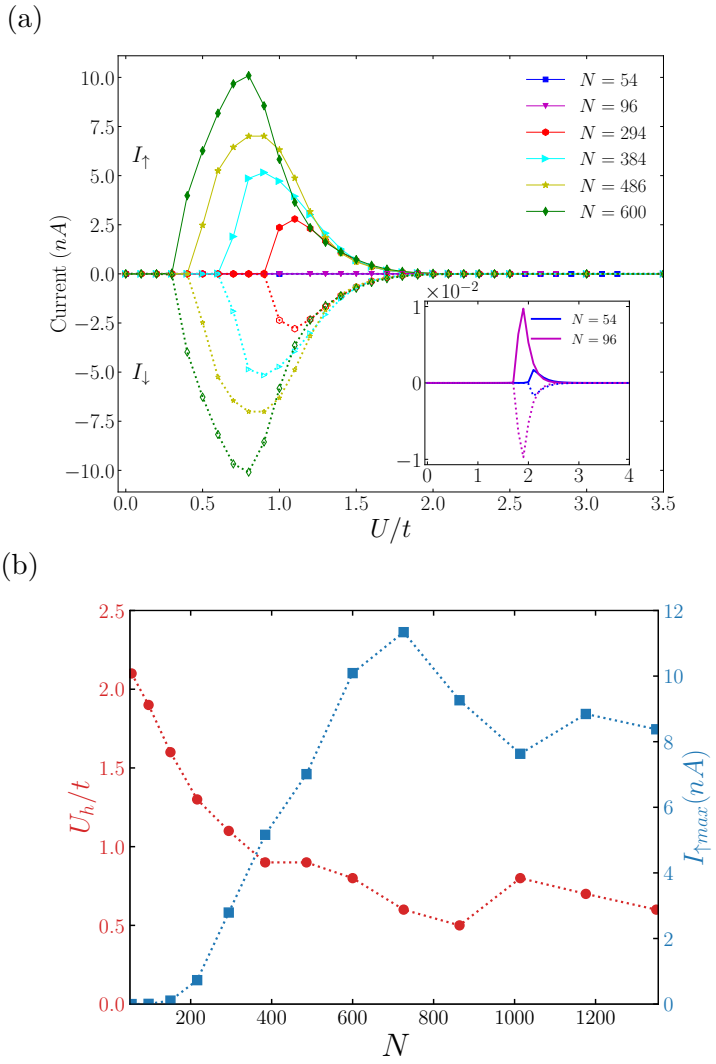

Figure 5.1: Spin-resolved currents versus U/t at $T_S = 0.026t$ and $\Delta T = 0.0052t$ for different sizes of hexagonal zigzag GNFs (a). The maximum value of spin-up current (blue curve) and corresponding value U_h/t (red curve) with respect to the number of sites of nanoflakes N (b). Here $\eta = 10^{-2}t$ and $\Gamma = 0.02t$.

with $I_{max\uparrow} \simeq 11.3\ nA$ at $U_h \simeq 0.6t$. The $I_{max\uparrow(\downarrow)}$ has the tendency to decrease with further increasing the nanoflake size. (ii) Both the spin up and spin-down currents then decrease relatively fast in the range of $U_h < U < U_c^{bulk}$ ($U_c^{bulk} \simeq 2.23t$ at the mean-field level). (iii) For $U \geq U_c^{bulk}$, since the graphene nanoflake becomes an insulator with a large gap the spin-up and spin-down currents completely disappear. From the results obtained, it can be concluded that the spin-resolved current driven by the temperature difference is only generated by the edge-localized magnetism. As a consequence, we believe that such currents do not exist in the hexagonal armchair GNF-based devices (without the external conditions or defects).

To proceed, we choose $U = U_h$ for each nanoflake to investigate the subsequent

behaviors of the spin-resolved current because each nanoflake has different critical point U_c as seen in Table 5.1. Here we focus on four zigzag graphene nanoflakes: $N = 54$, 96, 294 and 600, with their corresponding Coulomb interactions $U_h/t = 2.1, 1.9, 1.1$ and 0.8, respectively.

Table 5.1: The maximum/minimum magnitude of spin-up/spin-down currents and the U_h/t corresponding to each graphene nanoflake.

N	U_c/t	U_h/t	$I_{\uparrow max}$ (nA)	$I_{\downarrow max}$ (nA)
54	2.0	2.1	0.00115	-0.00115
96	1.7	1.9	0.00752	-0.00752
150	1.5	1.6	0.1064	-0.1064
216	1.24	1.3	0.7301	-0.7301
294	0.9	1.1	2.7913	-2.7913
384	0.6	0.9	5.1618	- 5.1618
486	0.5	0.9	7.0113	-7.0113
600	0.3	0.8	10.0909	-10.0909
726	0.2	0.6	11.3395	- 11.3395
864	0.13	0.5	9.2635	-9.2635
1014	0.09	0.8	7.6319	-7.6319
1176	0.05	0.7	8.8453	-8.8453
1350	0.04	0.6	8.3785	-8.3785

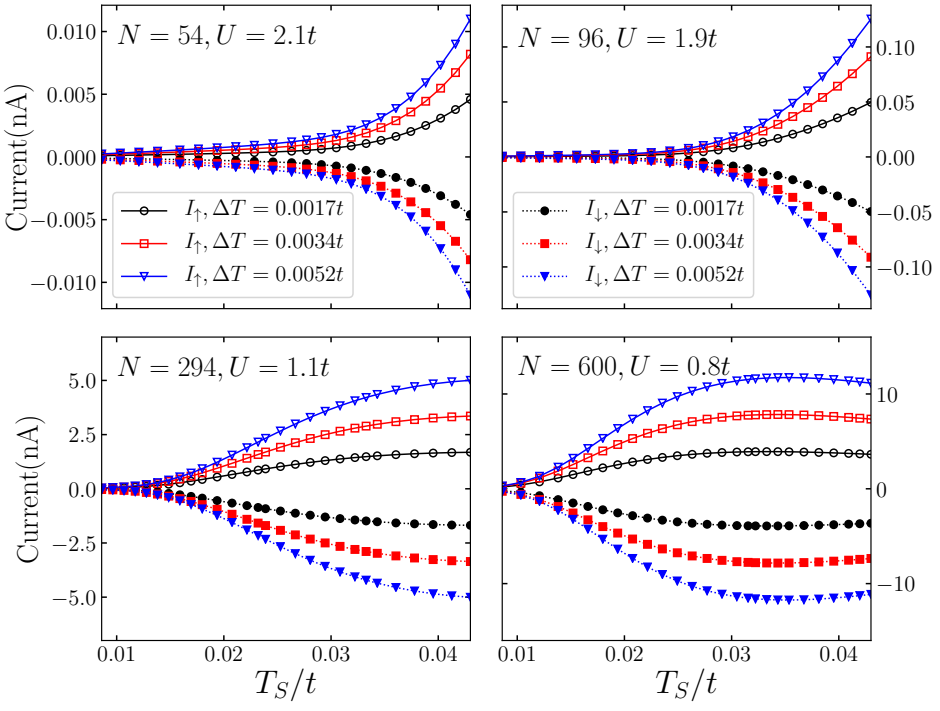

Figure 5.2: Spin-resolved currents versus T_S/t and temperature gradient ΔT for different nanoflake sizes with $\eta = 10^{-2}t$ and $\Gamma = 0.02t$.

Figure 5.2 presents the thermally induced spin current versus the source temperature T_S for three temperature differences $\Delta T = 0.0017t$, $0.0034t$ and $0.0052t$. There exists a threshold temperature T_{th} that the current is negligible for $T_S < T_{th}$. The T_{th} diminishes with the expansion of the nanoflake size. In addition, the T_{th} shares the same amplitude for the spin-up and spin-down currents. When T_S exceeds T_{th} the spin-up and spin-down currents are detected with significant magnitude in the device. For the range of T_S and ΔT considered, one finds that the spin-up current $I_\uparrow$ and the spin-down current $I_\downarrow$ have opposite signs, indicating their opposite flowing directions. Typically, a positive spin-up current flows from the source to the drain, while a negative spin-down one flows from the drain to the source. Since the magnitude of the spin-up current is equal to that of the spin-down current, a net charge current $I_{charge} = I_\uparrow + I_\downarrow$ is totally suppressed, while the net spin current $I_{spin} = I_\uparrow - I_\downarrow$ flowing the source to the drain is twice as large as the spin-up (or spin-down) current. This result gives rise to a pure spin current and a perfect spin Seebeck effect in the device. These effects are also predicted in the zigzag grahene nanoribbons [40, 171], nevertheless an external magnetic field is required. In the meanwhile, our proposed device can easily achieve these effects without the external magnetic field. For a fixed ΔT, the spin-up and spin-down currents increase with increasing T_S. Due to the substantial reduction of the threshold temperature in large nanoflakes, *i.e.*, $N = 294$ and $N = 600$, the spin current goes up relatively fast at low temperature. It is worth mentioning that a significant spin current $I_{spin} \approx 20$ nA is recorded for the nanoflake with size $N = 600$ at $T_S = 0.026t$ ($T_S \approx 300K$) and $\Delta T = 0.0052t$. When T_S is now fixed, the spin-dependent currents go up almost linearly as ΔT increases. Moreover, one also finds that the spin-up and the spin-down currents in bigger nanoflakes are much higher than those in smaller ones at a fixed T_S or ΔT, for example, an insignificant spin current, $I_{spin} \approx 0.02$ nA, obtained in the 54-nanoflake, while a large $I_{spin} \approx 22.3$ nA obtained in the 600-nanoflake at $T_S = 0.043t$ and $\Delta T = 0.0052t$. In comparison, the similar results for $N = 600$ are also obtained within the DMFT + NRG[1] (NRG: Numerical Renormalization Group), see Appendix A.1, indicating the reliability of our findings obtained from the mean-field level. The nature of these phenomena will be discussed in the next section.

[1]The DMFT+NRG calculations are carried out by our colleague, Robert Peters coming from Kyoto University, Japan.

5.2 The physical mechanism of thermally induced spin current

According to the Landauer-Büttiker formula,

$$I_\sigma = \frac{e}{h}\int_{-\infty}^{\infty} dE(f_S(E,T_S) - f_D(E,T_D))T_\sigma(E), \tag{5.1}$$

the spin-resolved current depends not only on the Fermi-Dirac distribution difference between the source and drain $(f_S - f_D)$ but also on the spin-dependent transmission $T_\sigma(E)$. Therefore, to understand the underlying physical mechanism of the transport properties, we analyze the distribution of charge carrier concentration at the two leads and the spin-dependent transmission coefficient.

Because of no electric voltage applied, the difference of the Fermi-Dirac distribution functions, $(f_S - f_D)$, is entirely determined by the difference of the temperatures at the leads. The sign of the function $(f_S - f_D)$ decides the flowing direction of the current at a certain energy considered [43]. When $T_S = T_D$, the device is in the equilibrium state due to $f_S(E,T_S) = f_D(E,T_D)$, resulting in hindering the charge carrier current. For $T_S > T_D$, $(f_S - f_D)$ is positive at the energy being higher than the Fermi energy E_F. The charge carriers with energy above E_F hence flow from higher temperature (the source) to lower temperature (the drain), yielding a positive electron current (I_e). On the contrary, $(f_S - f_D)$ is negative at the energy being lower than E_F. As a result, a negative hole current (I_h) is created due to carriers below E_F flowing from the drain to the source. As exhibited in Figure 5.3, $(f_S - f_D)$ is symmetric with respect to the Fermi energy (set to be zero), the currents hence induced by the carriers above and below the Fermi energy can cancel each other if the transmission spectrum is symmetric with respect to E_F [40]. To obtain the current, the asymmetric distribution of the transmission spectrum around E_F is indispensable. Furthermore, Figure 5.3 also indicates that the peaks of $(f_S - f_D)$ are located at the energies close to $E_F = 0$, therefore the transmission peaks around E_F contribute more to the current [43]. On the other hand, since electrons and holes carry charge and spin, they might bear concurrently both charge current and spin current in the device.

We consider first the transmission coefficient of nanoflakes for the *ortho* and *para* configurations. As plotted in Figure 5.4, even though the magnetization is turned

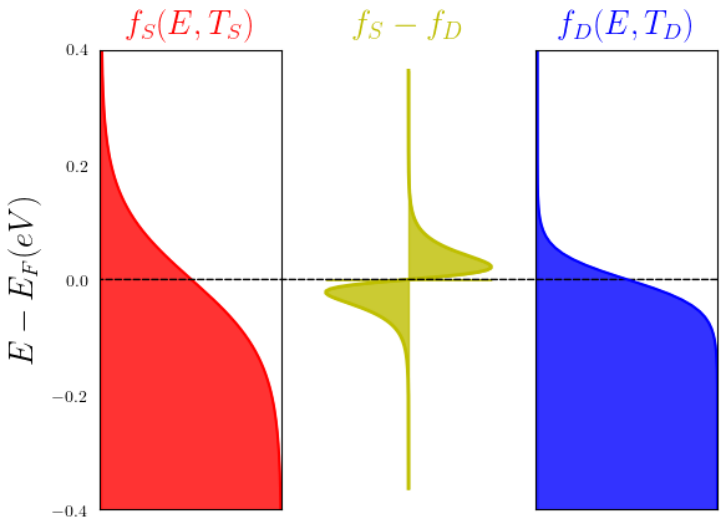

Figure 5.3: The carrier concentration difference between the source and the drain.

on, the spin degeneracy of T_σ is still protected as in the paramagnetic phase for all nanoflakes. Therefore, the spin-dependent transmission spectra are symmetric with respect to E_F, resulting in the cancellation of the carrier currents in these two configurations. The reason for that can be explained through the Green's function because, in our description of the leads, the transmission coefficient, $T_\sigma(E) = \Gamma^2 \sum_{ij\sigma}(G^r_{ij\sigma}(E))^* G^r_{ij\sigma}(E)$, is entirely governed by the Green's function. According to Valli et al. [39], in the presence of the particle-hole symmetry the Green's function transforms in the following way (see Appendix A.2 for details)

$$G^r_{ij\sigma}(-E) = -(-1)^{i+j}(G^r_{ij\sigma}(E))^* \tag{5.2}$$

where the prefactor $(-1)^{i+j}$ equals to ± 1 depending on whether i and j belong to the same or different sublattices. In the AF state, the relation above is written in combination with the spin inversion $\sigma = \bar{\sigma} = -\sigma$ as $G^r_{ij\sigma}(-E) = -(-1)^{i+j}(G^r_{ij\bar{\sigma}}(E))^*$, yielding the relation for spin-dependent transmission

$$T_\sigma(E) = T_{\bar{\sigma}}(-E) \tag{5.3}$$

for all configurations considered. Since the magnetic order coincides with the chiral sublattices, the spin inversion is analogous to the inversion of the chiral pseudospin [39], *i.e.*, exchanging the role of spin and sublattices indices. Thus when i and j belong to different sublattices, as in the *ortho* and *para* configurations, the transmission becomes $T_\sigma(E) = T_\sigma(-E)$ and along with Eq. (5.3), resulting in the

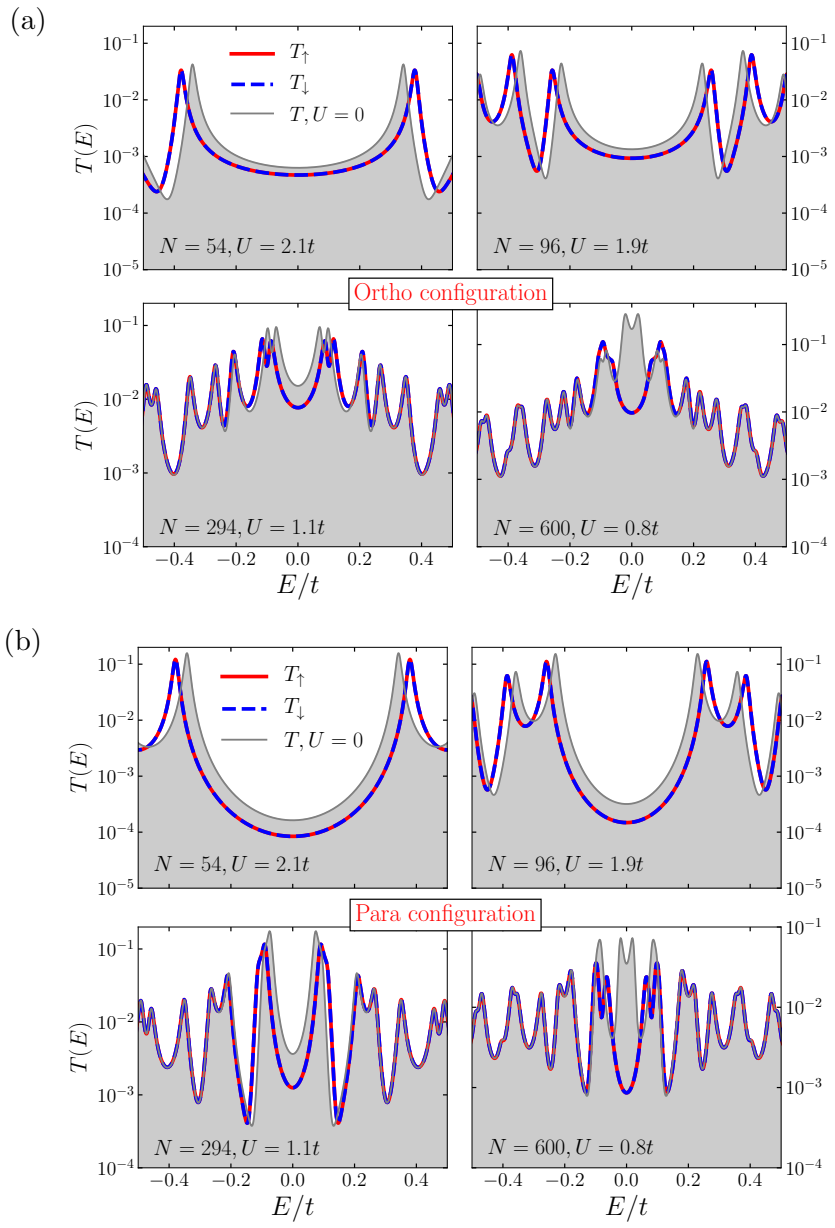

Figure 5.4: Transmission coefficient as a function of E/t in (a) *ortho* and (b) *para* configurations for four nanoflakes plotted in separate panels. Here $U = U_h$, $\eta = 10^{-2}t$ and $\Gamma = 0.02t$.

conservation of the spin degeneracy of the transmission: $T_\sigma(E) = T_{\bar{\sigma}}(E)$. Consequently, the spin transport in these two configurations is hindered. This is why there is no current observed in the *ortho* and *para* configurations. By contrast, $T_\sigma^{AA}(E) = T_{\bar{\sigma}}^{BB}(E)$ in the *meta* configuration which shows the asymmetric spin-resolved transmission spectrum, giving rise to a nonzero current. In the following, we present the detailed analysis for the *meta* configuration.

In the paramagnetic phase, the transmission spectrum (gray curve in Figure 5.5)

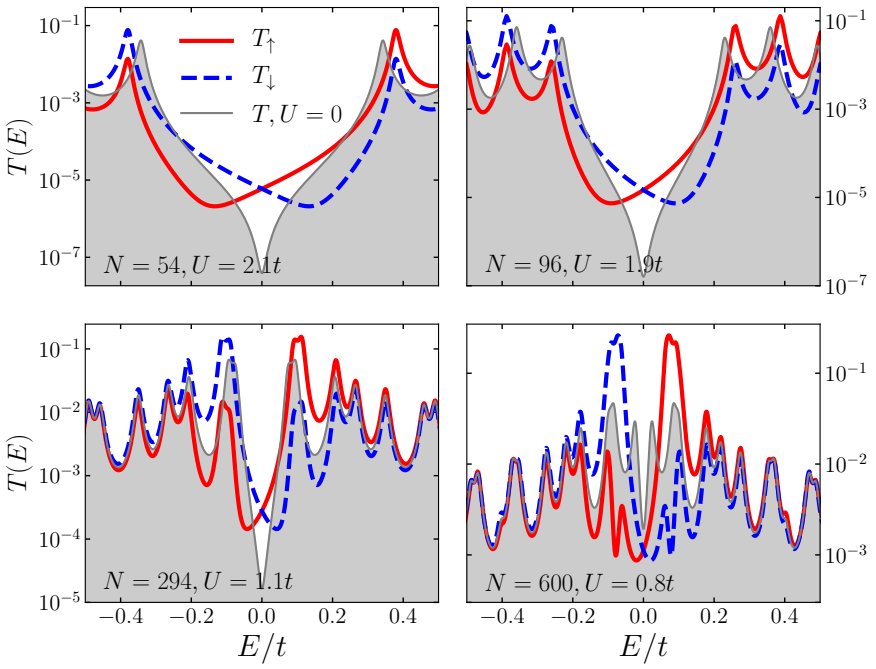

Figure 5.5: Transmission coefficient for spin-up and spin-down versus E/t in *meta* configuration for four nanoflakes. Here $U = U_h$, $\eta = 10^{-2}t$ and $\Gamma = 0.02t$.

is symmetric around the Fermi energy as in the *ortho* and *para* configurations. The spin current is not triggered due to the competition of the electron and hole currents. In the antiferromagnetic phase, as can be seen in Figure 5.5 for all GNFs of interest, the transmission spectra for up spin show that the spin-up electrons and holes can pass above and below E_F, respectively. Since the magnitude of the spin-up transmission peaks above E_F is much larger than that below E_F, the electron current dominates compared with the hole current for the spin-up state, giving a thermal spin-up electron current. On the contrary, the spin-down transmission peaks below E_F are much higher than those above E_F, leading to a thermal spin-down hole current. As a result, a nonzero thermally induced spin-dependent current are produced. In addition, since the spin-up and spin-down transmission spectra are symmetric to each other with respect to E_F, the spin-up electron current equals the spin-down hole current.

On the other hand, the overlap of the Fermi-Dirac distribution difference $(f_S - f_D)$ and the spin-dependent transmission $T_\sigma(E)$ determines the amplitude of the thermally induced spin current in the device [40, 171]. Since the peaks of $(f_S - f_D)$ are close to the Fermi energy, as shown in Figure 5.3, depending on the distance of the transmission peaks to E_F it requires different source temperatures to trigger

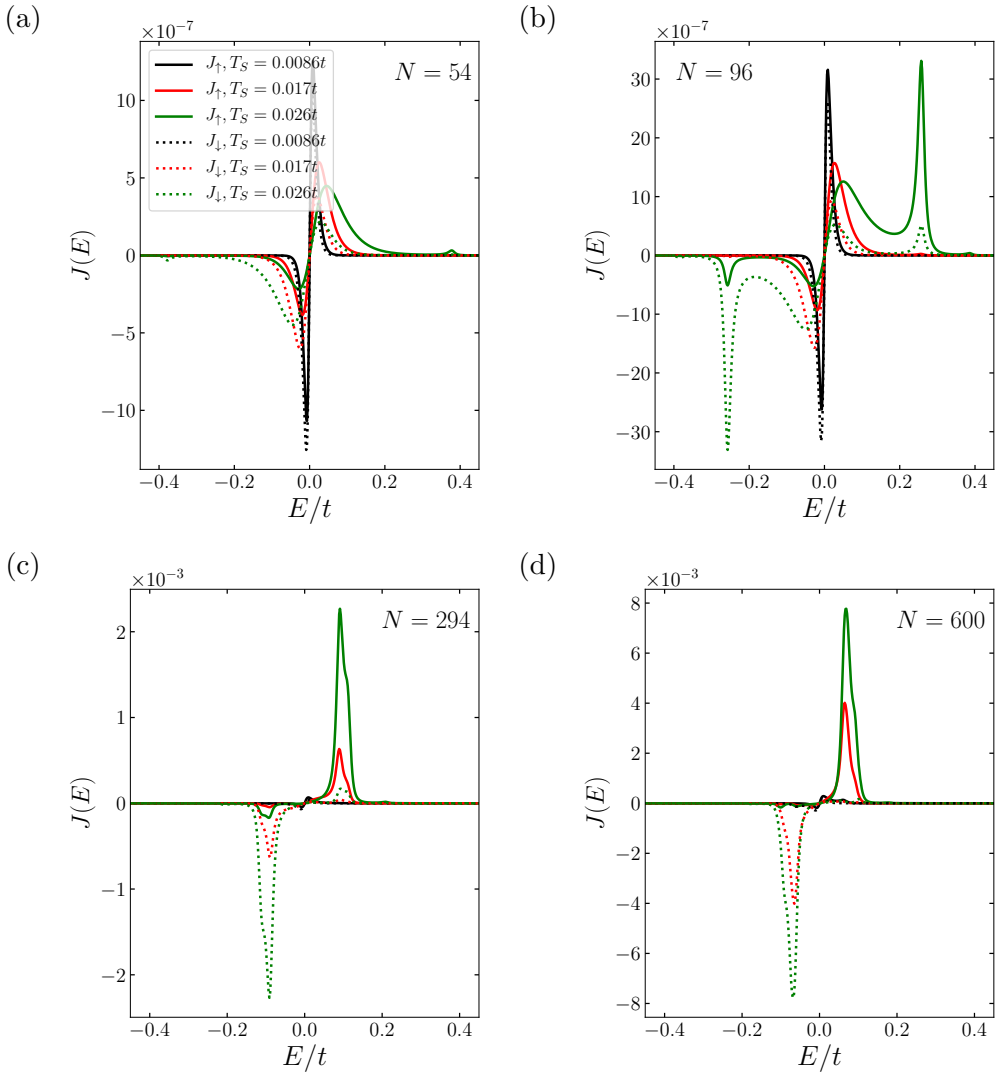

Figure 5.6: Spin-resolved current spectra $J(E)$ versus energy E/t for different T_S and a fixed $\Delta T = 0.0052t$ for four nanoflakes: $N = 54$ (a), 96 (b), 294 (c) and 600 (d) with $U = U_h$, $\eta = 10^{-2}t$ and $\Gamma = 0.02t$.

the spin current. In particular, the transmission peaks of two smaller GNFs are relatively far away from the Fermi energy due to the existence of a quite large bandgap, it thus needs high threshold temperatures T_{th} to broaden the Fermi-Dirac distribution difference so as to overlap with transmission peaks. It only needs a low T_{th} to apply in two bigger ones to get the spin current owing to the proximity to E_F of the transmission peaks. Therefore, it can be said that the reduction of the T_{th} is explained by how close the transmission peaks are to the Fermi energy. In addition, the bigger the overlapping region is, the higher the spin current is. As a result, the spin current in bigger nanoflakes is much higher than that in smaller ones. In other words, the transmission peaks are far away from the Fermi energy

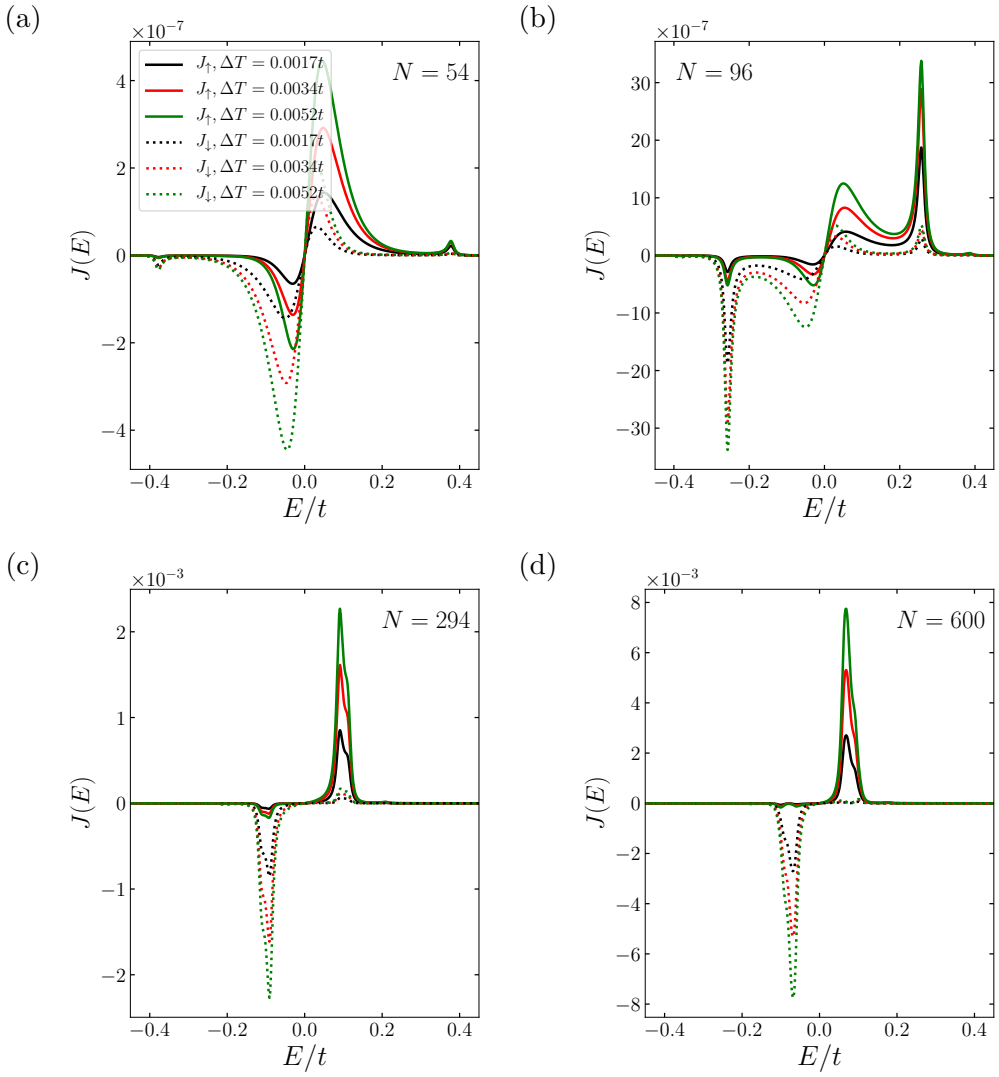

Figure 5.7: Spin-resolved current spectra versus energy E/t at several ΔT and a fixed $T_S = 0.026t$ for four configurations: $N = 54$ (a), 96 (b), 294 (c) and 600 (d) with $U = U_h$, $\eta = 10^{-2}t$ and $\Gamma = 0.02t$.

due to the enlargement of the gap with strong U/t. The spin-resolved current thus reduces gradually and reaches zero when U/t increases. In addition, we can deduce that due to the limitation of the peaks of $(f_S - f_D)$, the transmission peaks just around E_F will contribute more to the current than those far away from E_F.

Moreover, we plot the current spectra $J_\sigma(E)$,

$$J_\sigma(E) = T_\sigma(E)(f_S(E, T_S) - f_D(E, T_D)), \tag{5.4}$$

to analyze quantitatively the spin-resolved current. Figures 5.6 and 5.7 show the current spectra with different T_S at the same ΔT and different ΔT at the same

T_S, respectively. The area verified by the curve of $J_\sigma(E)$ and the horizontal energy axis determines the amplitude of spin currents [47,175]. The spin-up and spin-down current spectra are symmetric to each other through $E/t = 0$ and $J_\uparrow(E) = -J_\downarrow(-E)$. It means that the current spectrum for $J_\uparrow$ is equal to that for $J_\downarrow$, giving $|I_\uparrow| = |I_\downarrow|$. At fixed ΔT, see Figure 5.6, for $N = 54$ and 96, the black spectra ($T_S = 0.0086t$) are nearly symmetric for both spin-up and spin-down, indicating approximately zero current. Although the spectra corresponding to $T_S = 0.017t$ and $T_S = 0.026t$ are asymmetric, the contribution of the spectra to the current is very small. Thus the spin current obtained in these two small nanoflakes is tiny. A high temperature (far away from room temperature) is required to attain a reasonable spin current for the two small nanoflakes. In the meanwhile, in the two bigger nanoflakes, the contribution of spin-resolved current spectra to the current is substantial, yielding the detection of a significant spin current. The same behavior is observed, Fig. 5.7, in the case fixing T_S and tuning ΔT. Typically, the more the temperature gradient goes up, the more the current spectra increases, resulting in the enhancement of the spin current.

5.3 The back-gate voltage-modulated spin current

By localizing back-gate voltage below the graphene nanoflakes, we study in this section the effect of the back-gate voltage V_g on the thermally induced spin currents of the graphene nanoflakes. The nanoflake is described by the following Hamiltonian

$$H_C = -t \sum_{\langle i,j\rangle\sigma} (c^+_{i\sigma} c_{j\sigma} + h.c) + U \sum_i (n_{i\uparrow} - \frac{1}{2})(n_{i\downarrow} - \frac{1}{2}) + V_g \sum_{i\sigma} c^+_{i\sigma} c_{i\sigma}. \tag{5.5}$$

An applied back-gate voltage can lead to the change of the electron density in the graphene nanoflakes. As a result, the magnetic solution of such nanoflakes can be modified [120]. However as long as the back-gate voltage is less than the gap of the graphene nanoflakes, the magnetic state is unaffected, only a back-gate voltage larger than the gap induces electron doping and thus possible changes of the magnetic state. In the following, we will neglect effects of the back-gate voltage on the magnetic solution and use the transmission coefficient of the systems determined at half filling. Figure 5.8 shows the spin-up and spin-down currents as a function of the back-gate voltage V_g/t at $T_S = 0.026t$ and $\Delta T = 0.0052t$. As can be seen, the spin-resolved

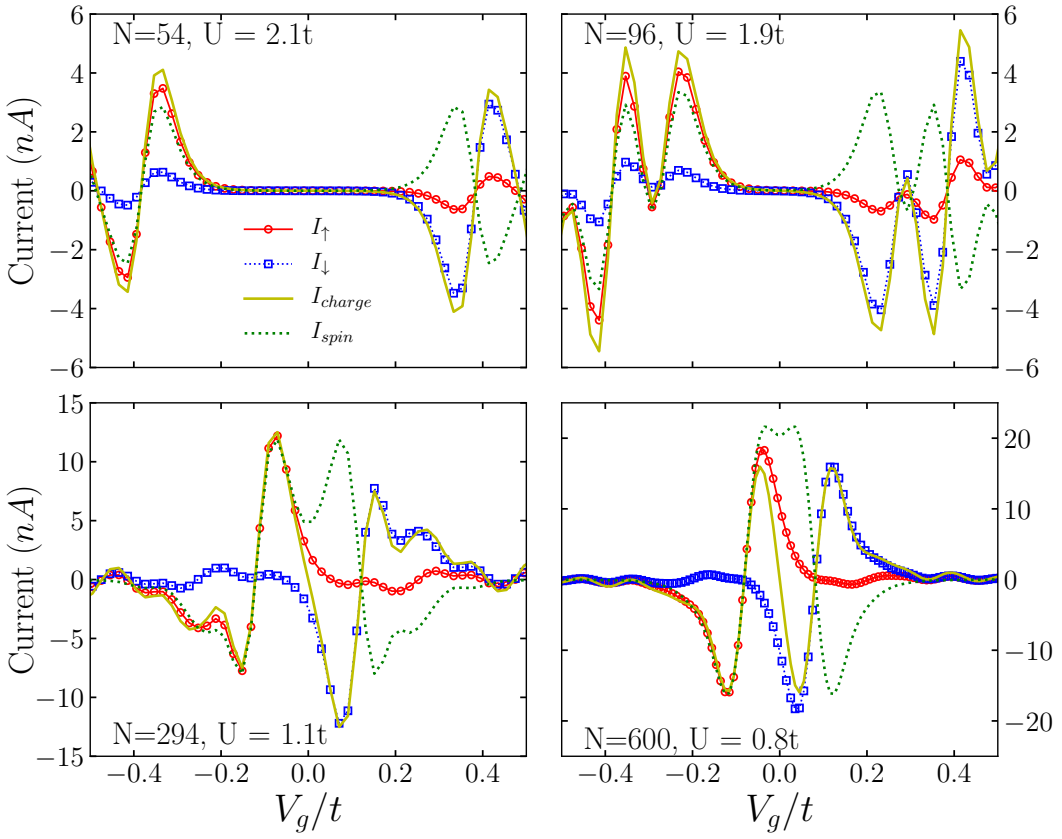

Figure 5.8: The dependence of the spin-resolved currents on the back-gate voltage V_g at $T_S = 0.026t$ and $\Delta T = 0.0052t$ for the nanoflakes with $U = U_h$, $\eta = 10^{-2}t$ and $\Gamma = 0.02t$.

currents are now asymmetric under the spin inversion with $I_\sigma(V_g/t) = -I_{\bar{\sigma}}(-V_g/t)$, giving rise to an even (odd) spin (charge) current. For two bigger nanoflakes, *i.e.*, $N = 294$ and 600, a pure spin current without charge current therefore only exists at $V_g = 0t$, while both the spin current and charge current are expected to be generated for non-zero back-gate voltage. For two smaller nanoflakes with $N = 54$ and 96, they require a finite V_g/t applied to trigger the currents in the device, typically $|V_g/t| > 0.2$ for $N = 54$ and $|V_g/t| > 0.1$ for $N = 96$. While the back-gate voltage drives the spin-up and spin-down currents flowing in the same direction in the two smaller nanoflakes, these currents either flow in the same direction or in the opposite direction in the two bigger nanoflakes. The flowing direction of the currents changes from the positive side to the negative side and vice versa observed in all nanoflakes. Taking $N = 600$ as an example, when $-0.08 < V_g/t < 0.08$, the positive $I_\uparrow$ flows from the source to the drain, but with $-0.43 < V_g/t < -0.08$ the $I_\uparrow$ with the negative sign flows in the opposite way. Such flowing effect of the spin-dependent currents is

attributed to the change in the charge carrier type from electrons (holes) to holes (electrons) for the spin-up (spin-down) current due to the chemical potential passing the transmission peak [40]. Furthermore, the response of the thermally induced spin current modulating by V_g exhibits dependence on the nanoflake size. Typically, a moderate V_g is required to amplify the spin-dependent currents and reach up to a maximum value in the two smaller nanoflakes, namely $|V_g/t| \sim 0.33$ for $N = 54$ and $|V_g/t| \sim 0.41$ for $N = 96$. In the meanwhile, the maximum value of the current shifts to smaller V_g for the two bigger nanoflakes, that is to say, it only needs a tiny V_g to harvest the highest peak of the spin-dependent current in 294 ($|V_g/t| \sim 0.07$) and 600 ($|V_g/t| \sim 0.035$) sizes. In addition, a nearly perfect spin-filtering effect can be achieved by tuning the back-gate voltage such that either the spin-up current or spin-down current is completely suppressed. Thereby both the charge current and spin current are contributed by only the spin-up or spin-down current, resulting in the equivalence in magnitude. Their currents flow either in the same or in the opposite direction depending on either the negative or positive back-gate voltage applied.

To proceed, we now fix $V_g/t = -0.04$ and consider two nanoflakes with the size of $N = 96$ and $N = 600$. The spin-up current is much larger than the spin-down current as shown in Figure 5.9. This effect can be understood by means of the transmission spectra. As indicated in Figure 5.9(c) and 5.9(f), although the symmetry of the spin-resolved transmission T_σ is still preserved well, the symmetric position in which the $T_\uparrow$ and $T_\downarrow$ cross each other shifts to the left-hand side of $E/t = 0$. The transmission peaks for spin-up channel get closer to zero energy than those of $T_\downarrow$. Consequently, the overlap between the Fermi-Dirac distribution difference and the transmission for the spin-up channel is much bigger than that for the spin-down channel. Therefore the spin-up current is amplified, while the spin-down current is suppressed. For the nanoflake with $N = 96$, an unipolar spin transport is displayed where the spin-up current goes up quickly as rising either the source temperature with $T_S > T_{th}$ at fixed ΔT or the temperature gradient ΔT at the same T_S, while the spin-down current is negligible in the range of T_S and ΔT studied. We find an interesting transition from bipolar, where $I_\uparrow = I_\downarrow$ without the back-gate voltage, to unipolar spin transport under the modulation of the temperature bias and the back-gate voltage. Such a transition was also detected in a magnetic local-gated ZGNR-based device by using the NEGF combined with the mean-field Hubbard at $V_g = 0.2\ V$ [171]. For the nanoflake with $N = 600$, when ΔT is fixed, the spin-up current increases linearly

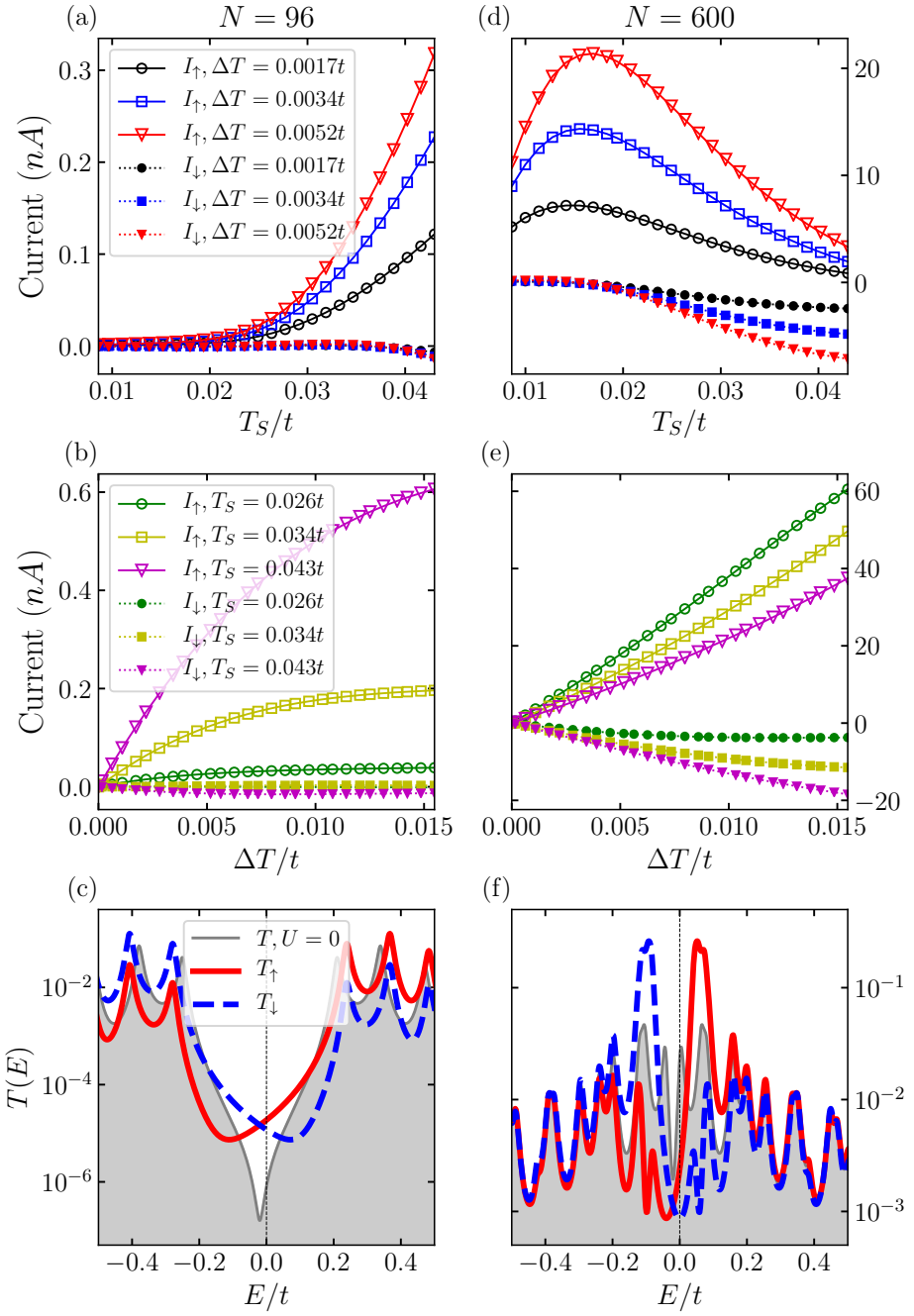

Figure 5.9: Spin-up and spin-down currents with respect to T_S and ΔT, and transmission coefficient as a function of E/t for $N = 96$ (a), (b), (c) and $N = 600$ (d), (e), (f) at a fixed $V_g/t = -0.04$, respectively, with $\eta = 10^{-2}t$ and $\Gamma = 0.02t$.

to a maximum value at low temperature and then decreases with further increasing T_S, indicating the existence of a negative differential thermoelectric resistance [149]. In the meanwhile, there is no spin-down current at low T_S. When T_S overcomes a threshold temperature, $I_\downarrow$ increases slowly. In addition, both the spin-up and spin-down currents increase linearly with rising the temperature difference at a fixed T_S

with different slopes.

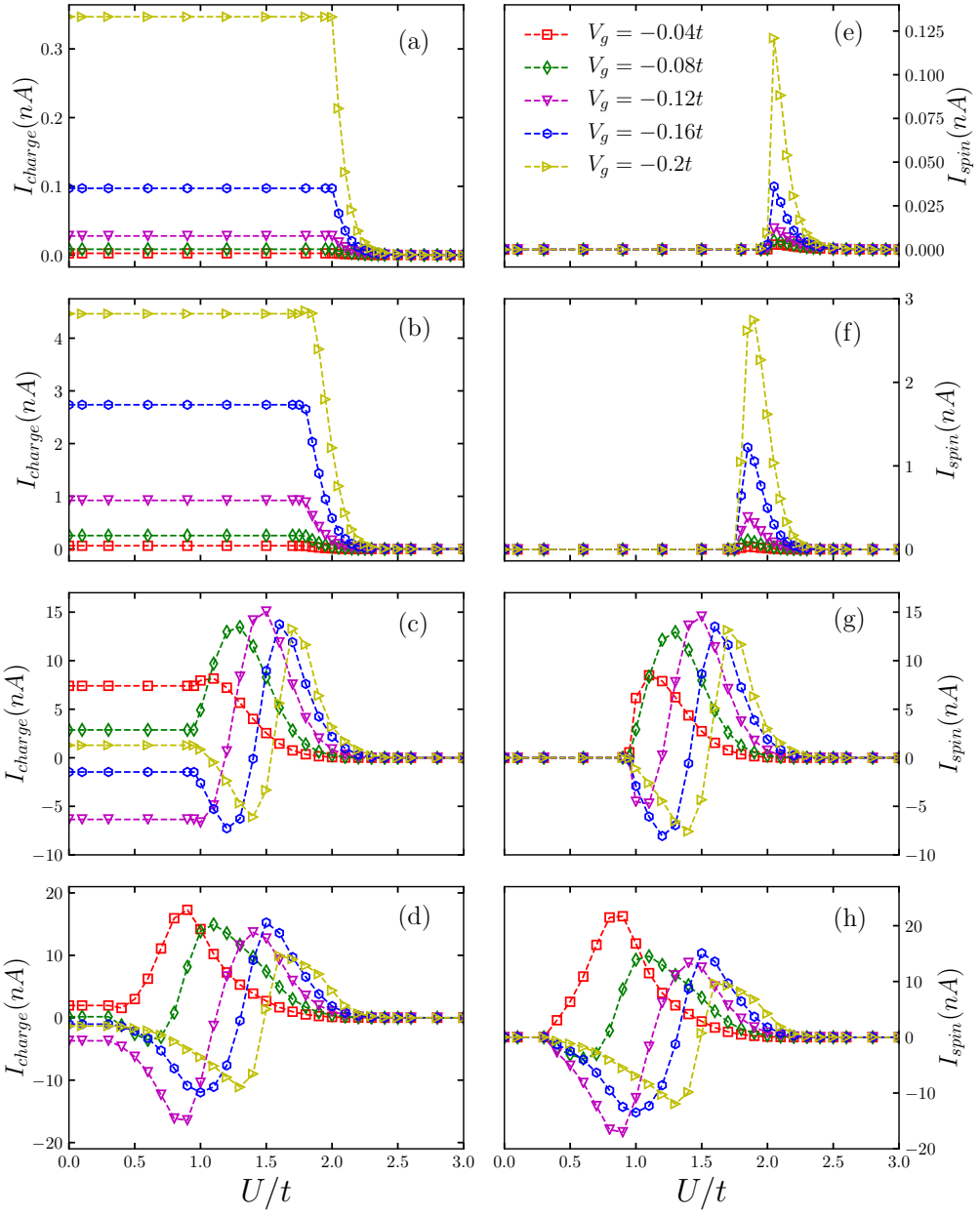

Figure 5.10: The impact of the Coulomb energy U on the charge and spin currents under several V_g for four nanoflakes, wherein (a) and (e) for $N = 54$, (b) and (f) for $N = 96$, (c) and (g) for $N = 294$, and (d) and (h) for $N = 600$, respectively, at $T_S = 0.026t$ and $\Delta T = 0.0052t$ with $\eta = 10^{-2}t$ and $\Gamma = 0.02t$.

Furthermore, increasing the back-gate voltage will shift further the symmetric position of the T_σ away from zero energy. On the other hand, the V_g/t does not change the nature of the transmission spectra, as seen in Figure 5.5 and Figure 5.9(c), (f). Combining these considerations with the effect of the gap, the peaks of the T_σ of

the two smaller nanoflakes approach to zero energy. Therefore, the overlap between the Fermi-Dirac distribution difference and the transmission for up spin (down spin) increases for the intermediate positive (negative) back-gate voltages, yielding to enlarge the currents in the device. On the contrary, for the two bigger nanoflakes, due to the tiny gap the small peaks of the spin-dependent transmission spectra mainly contribute to the current for an intermediate and high V_g/t. Hence, the currents get suppressed rather than being amplified, as indicated in Figure 5.8. A similar scenario exists for the two smaller nanoflakes at higher V_g/t.

We next discuss the influences of the on-site Coulomb energy and the back-gate voltage on the thermally induced spin-dependent current. Figure 5.10 plots the charge current and spin current as a function of U/t and V_g/t at $T_S = 0.026t$ and $\Delta T = 0.0052t$. One observes three different characteristics of the currents flowing in the device. Firstly, the back-gate voltage induces a net constant charge current and zero spin current for all $U < U_c$. The magnitude and current direction of such a net charge current can be tuned by V_g/t and nanoflake size as shown in Figure 5.10. The emergence of a net charge current is due to the asymmetry of the transmission spectra (gray curve) around zero energy, as shown in Figure 5.9(c) and 5.9(f). Secondly, the spin-dependent currents are observed as $U > U_c$ with different responses for all nanoflakes proposed. For small nanoflakes, *i.e.*, $N = 54$ and $N = 96$, the charge current strongly decreases to approximately zero from U_c/t to $U_c^{bulk} \simeq 2.23t$. In contrast, the spin current skyrockets to the maximum value before dwindling drastically to zero. It is also indicated that the increase of V_g/t (in the range considered) enhances the spin current in the small hexagonal nanoflake-based devices. More interesting responses are seen in the nanoflakes with $N = 294$ and $N = 600$. The change of the current direction of both the charge current and the spin current is displayed upon increasing V_g/t, while the flowing direction is stable with $V_g/t = -0.04, -0.08$ for $N = 294$ and $V_g/t = -0.04$ for $N = 600$. In more detail, when the current direction remains unchanged, the charge and spin currents exhibit the same behavior as in the zero back-gate voltage case. For the case when the current direction changes, I_{charge} and I_{spin} first decrease to a minimum value and then increase to zero. Subsequently, these currents change their signs from negative to positive and keep rising until reaching a positive maximum value before gradually reducing to zero. The maximum value shifts to the right-hand side corresponding to the increment of V_g/t. Finally, there is no current if U/t goes far from U_c^{bulk}/t due to the presence of a large gap in the nanoflakes.

In conclusion, From the results obtained above, the gate-localized graphene nanoflakes can support for developing multi-function spintronic devices.

Furthermore, apart from the above, similar current responses can be also exploited when depositing the graphene nanoflake on the hBN (see Appendix A.3 for details). At the computational level, the effect of hBN on GNFs can be encoded by ϵ which can be understood as a sublattice potential. Herein, if ϵ is less than the bandgap of GNFs, the magnetic properties are not affected. In contrast, the magnetic moments are partially quelled if ϵ exceeds the bandgap. Therefore, it requires larger Coulomb energy to switch on the edge magnetization on the GNFs. As a result, the spin current might vanish with further increasing ϵ. In addition, our calculations show that a nearly complete spin-filtering effect can be achieved in this case.

5.4 The charge and spin thermovoltage

A thermovoltage can be generated at two electrodes when the thermal currents are produced across the hexagonal GNF junction. The thermovoltage can be determined from the open-circuit condition with the definitions [198]

$$\begin{aligned} I_{charge}(V^{th}_{charge}, \Delta T) &= 0, \\ I_{spin}(V^{th}_{spin}, \Delta T) &= 0. \end{aligned} \tag{5.6}$$

Herein the thermally activated currents (thermocurrents) in the device are defined as $I_{charge}(V, \Delta T) = (I_\uparrow + I_\downarrow)$ and $I_{spin}(V, \Delta T) = (I_\uparrow - I_\downarrow)$, with V the bias voltage applied across the junction in which one puts to be zero, $V = 0$. Therefore, we emphasize the flow of charge carriers driven by the thermal flux in the device. Once having the thermocurrents, the thermovoltages are found from Eqs.(5.6). The numerical results are shown in Figure 5.11 which displays the charge and spin thermovoltages as a function of the temperature difference ΔT and the negative back-gate voltage. With the increase of ΔT both V^{th}_{charge} and V^{th}_{spin} increase for a fixed V_g. This result exhibits a good correlation between the V^{th}_{charge} and I_{charge} and the V^{th}_{spin} and I_{spin} curves in which both I_{spin} and I_{charge} go up corresponding to the enlargement of ΔT in the presence of the back-gate voltage. As fixing ΔT and changing the magnitude of $V_g/t \in [-0.005, -0.01, -0.02, -0.03, -0.04]$, the back-gate voltage shows an opposite impact on the V^{th}_{charge} and V^{th}_{spin}. In particular, the charge thermovoltage

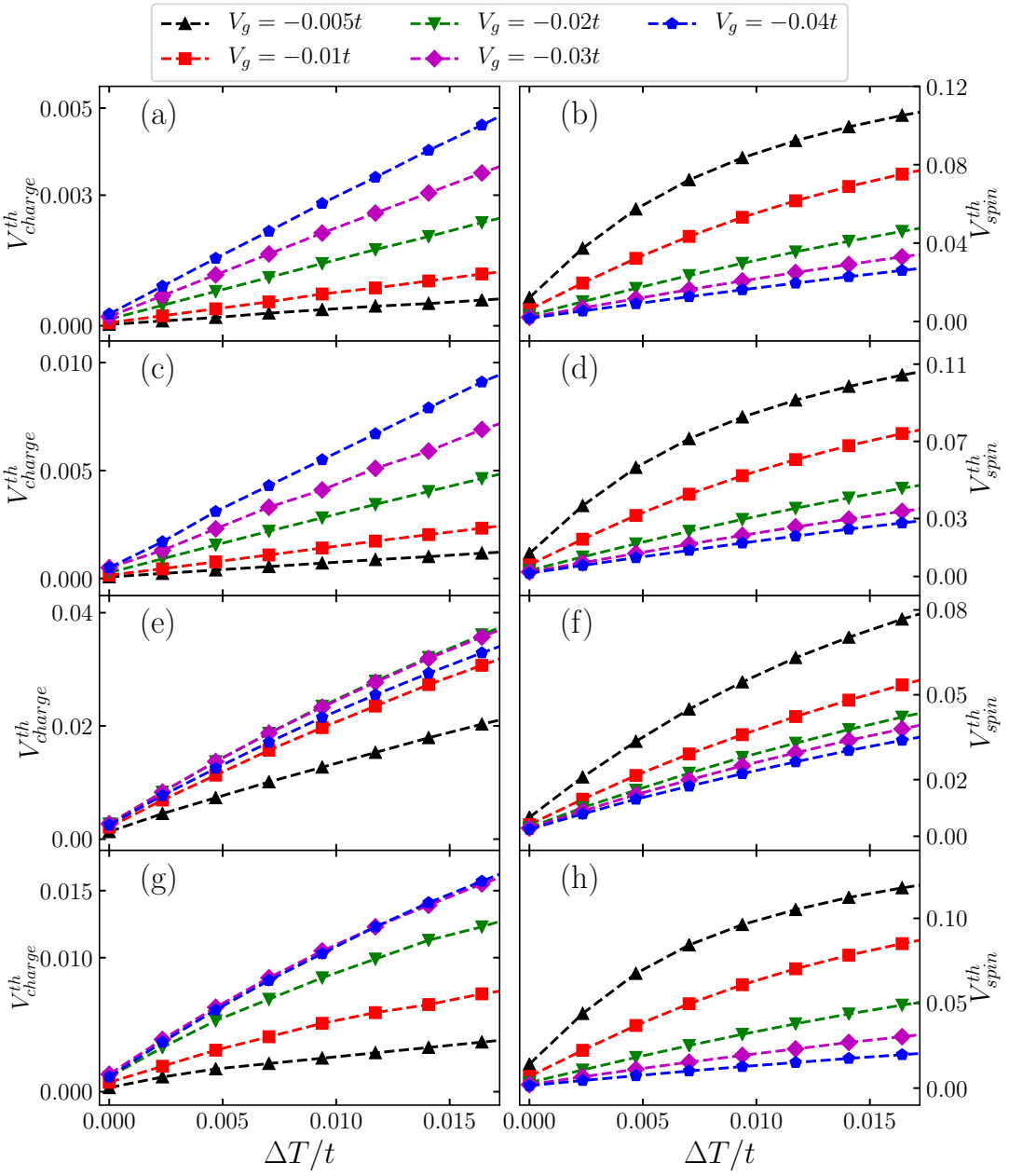

Figure 5.11: Charge and spin thermovoltages as a function of ΔT and V_g for four nanoflakes: (a) and (b) for $N = 54$, (c) and (d) for $N = 96$, (e) and (f) for $N = 294$, and (g) and (h) for $N = 600$, respectively, with $\eta = 10^{-2}t$ and $\Gamma = 0.02t$.

has an uptrend while the spin thermovoltage has a downtrend with increasing the V_g of interest. A similar trend will be observed with the opposite sign if the positive back-gate voltage is applied.

On the other hand, we know well the relation between the thermovoltage and ther-

mopower (the Seebeck effect) in the thermal device [199],

$$S_{charge/spin} = -\frac{V^{th}_{charge/spin}}{\Delta T}. \tag{5.7}$$

As can be seen in Figure 5.11, for the values of V_g considered, when the V^{th}_{charge} and V^{th}_{spin} are positive both the charge and spin thermopowers are negative. Thus the spin-up carriers play a crucial role in the transport, indicating in a good agreement with the numerical results in Figure 5.8. In contrast, the thermopower will change its sign from negative to positive if the back-gate voltage has a positive sign, giving rise to the majority of spin carriers being spin-down. These findings explicitly show that a strong thermoelectric effect can be obtained in the hexagonal graphene nanoflakes with tuning the back-gate voltage.

Chapter 6

Summary

We presented in this dissertation our numerical results obtained in our research on graphene nanoflakes. Herein, the role of the electron-electron interaction on the magnetic and transport properties of GNFs was explored. Three main topics are emphasized including: (1) The phase transition from the non-magnetic state to the AF state on the bulk graphene without and with SOC; (2) Interaction effect on the zigzag GNFs with different sizes and geometries; (3) Spin-resolved transport of charge carriers in the magnetic GNFs in contact with the electrodes (*spin caloritronic* device) induced by the temperature difference. All three problems were solved using the Hartree-Fock mean-field approximation.

(1) The impact of the electron-electron interaction was studied in the framework of the single-band Hubbard model without adding and with the spin-orbit interaction. The gapless SM (for zero SOC) and the topological band insulator (for nonzero SOC) are stable for weak to intermediate electron-electron interaction. The system undergoes a transition to the AF phase at strong coupling. The AF order is of the Néel type without SOC, and of the easy-plane type with SOC. At the Hartree-Fock meal-field level, we indicated that a semimetal-Mott insulator transition occurring at $U_c^{bulk} \simeq 2.23t$ (t is the nearest-neighbor coupling in graphene) without the SOC is independent on the quantization axis. As the SOC is introduced, the $\lambda - U$ phase diagram within the Hartree-Fock meal-field Kane-Mele-Hubbard model computed is believed to be more accurate than that shown in the work of Rachel et al. [83].

(2) Neglecting the contribution of SOC, our numerical results obtained from the single-band Hubbard model at half-filling and zero temperature demonstrated theoretically the existence of the intrinsic magnetization in zigzag graphene nanoflakes. Because of the presence of the edge-localized states, a weak repulsive Coulomb energy U ($U < U_c^{bulk} \simeq 2.23t$) might induce the intrinsic magnetic moment on the zigzag edge, while zero magnetization on the armchair edge. The ferromagnetic orders

show in the intra-edges while the antiferromagnetic or ferromagnetic orders develop in the inter-edges depending on the type of inter-edge connection either the armchair defect or the zigzag defect. Most importantly, by investigating systematically the instability of the magnetization on the zigzag edge with respect to the electron-electron interaction in hexagonal and diamond graphene nanoflakes with the range from small to big size, our calculations indicated that the value of U_c/t decreases upon increasing the number of carbon atoms on the zigzag edge of the nanoflakes. This can be considered as a consequence of the reduction of the bandgap and the density of the armchair defect when the nanoflake size increases. When the strength of electron-electron interaction overcomes the U_c^{bulk}, the antiferromagnetic pattern is preserved without the dependence on the size or geometry as well as edge termination. Although numerous studies of the magnetism on the graphene nanoflakes have been implemented, there has been still no a detailed study indicating the shift to approximately zero of U_c/t at large enough nanoflake size. Therefore, our investigation suggests the possibility of fabricating the magnetic graphene nanoflakes with all shapes when the size of nanoflakes is large enough in experiment.

(3) By the exploitation of the graphene sublattice, geometric symmetry and intrinsic magnetism of the hexagonal zigzag graphene nanoflakes, we obtained good effects compared to previous works. The crucial result in this topic is a spin-resolved current induced by a thermal gradient produced in the device. Since the transmission peaks for the spin-up and spin-down channels are symmetric to each other with respect to the Fermi energy ($E_F = 0$), the spin-up and spin-down currents flowing in opposite directions are equal to each other in magnitude. Hence a perfect Spin Seebeck effect and a pure spin current without a charge current are acquired, exhibiting the potential for developing a perfect spin caloritronic device based on the hexagonal zigzag GNFs. Noticeably, the thermally induced spin-resolved current is only generated in the *meta* configuration, where the leads are connected with all carbon atoms of the same graphene sublattice either A or B. In the meanwhile, there is no spin-polarized transport in the *ortho* and *para* configurations, where the leads are connected with sites belonging to different graphene sublattices, due to the symmetry in the configuration. Furthermore, the findings also indicated the nanoflake size dependency of such a spin-resolved current. A very tiny spin current flows in small graphene nanoflakes, namely $N = 54$ and 96, while a substantial spin current can be harvested in large ones as in $N = 294$ and 600 at room temperature. In addition, the shifting of the crossing position of spin-up and spin-down transmis-

sion spectra below or above the Fermi energy depending on whether the sign of the back-gate voltage V_g is either negative or positive gives rise to the asymmetry of the spin-up and spin-down currents. By tuning the back-gate voltage, some impressing expected effects of the spin-resolved current were acquired such as a transition from the bipolar to unipolar spin transport, the amplification of spin-resolved current, the manipulation of the flowing direction of the currents, the nearly complete spin-filtering effect and the negative differential thermoelectric resistance. On the other hand, the impact of the electron-electron interaction on the thermally induced spin-resolved current was studied which has never been found in other graphene-based devices. The spin-resolved current only flows across the device as $U_c < U < U_c^{bulk}$ and no current with $U > U_c^{bulk}$ due to the graphene nanoflake becoming an antiferromagnetic insulator with large bandgap. In the paramagnetic state, the presence of the back-gate voltage induces a net charge current while it vanishes if $V_g/t = 0$. Moreover, due to the change in the carrier type from electrons (holes) to holes (electrons) for spin-up (spin-down) current in the presence of the V_g, the flowing direction of the spin-up and spin-down currents changes in opposite side upon increasing either V_g/t at fixed U/t or U/t at fixed V_g/t. These results allow us to potentially design a multi-functional spin caloritronic device based on a back-gate voltage-localized graphene nanoflake hosting the intrinsic edge magnetism. With the considerations in our investigation, we believe that a similar scenario can be obtained in all shapes of graphene nanoflakes with the graphene sublattice balance (where $N_A = N_B$). This is confirmed by our calculations for diamond graphene nanoflakes.

Future work: I will exploit the transport properties in the spin caloritronic devices based on bilayer (multi-layer) graphene nanoflakes. Interesting effects are expected when rotating an angle between graphene layers because such rotation can modulate magnetic structure in graphene [200, 201].

Appendices

Appendix A

Thermally induced spin current across a spin caloritronic device

A.1 The thermally induced spin current within the dynamic mean-field theory

For comparison, the results obtained from the real-space dynamical mean-field theory (DMFT) combined with the numerical renormalization group (NRG) are presented here. The real-space DMFT is well-established as a non-pertubative treatment of local electron correlation. The key idea of this theory is to map the many-body problem of the Hubbard model onto an effective quantum impurity problem with a self-consistent condition [202]. With the real-space DMFT, the self-energies which take into account all interaction effects are local but site dependent for an inhomogenous system [203]. In the real-space DMFT approximation, the Hubbard Hamiltonian can be mapped onto a set of single-site problems. To be convenient, a local effective action S_{eff} for that site which is described in terms of an imaginary-time action for the fermionic operators $c_{i\sigma}$ and $c^{+}_{i\sigma}$ is given as [202]

$$S_{eff} = -\int d\tau \int d\tau' \sum_{\sigma} c^{+}_{i\sigma}(\tau) G_{0i\sigma}(\sigma, \tau - \tau')^{-1} c_{i\sigma}(\tau') + U \int d\tau n_{i\uparrow}(\tau) n_{i\downarrow}(\tau), \quad \text{(A.1)}$$

with τ being the imaginary time. $G_{0i\sigma}(\sigma, \tau - \tau')$ is the local non-interacting propagator which can be interpreted as a local dynamical Weiss field. This *Weiss function* is a function of time instead of a single number, thus it takes into account local quantum fluctuation [202]. Comparing with the mean-field theory which assumes that fluctuations are frozen, the dynamical mean-field theory freezes spatial fluctuation but considers the local temporal fluctuations. The local self-energies are determined from solving Eq. (A.1). $G_{0i\sigma}(\omega)$ is obtained from the local Dyson equation in the

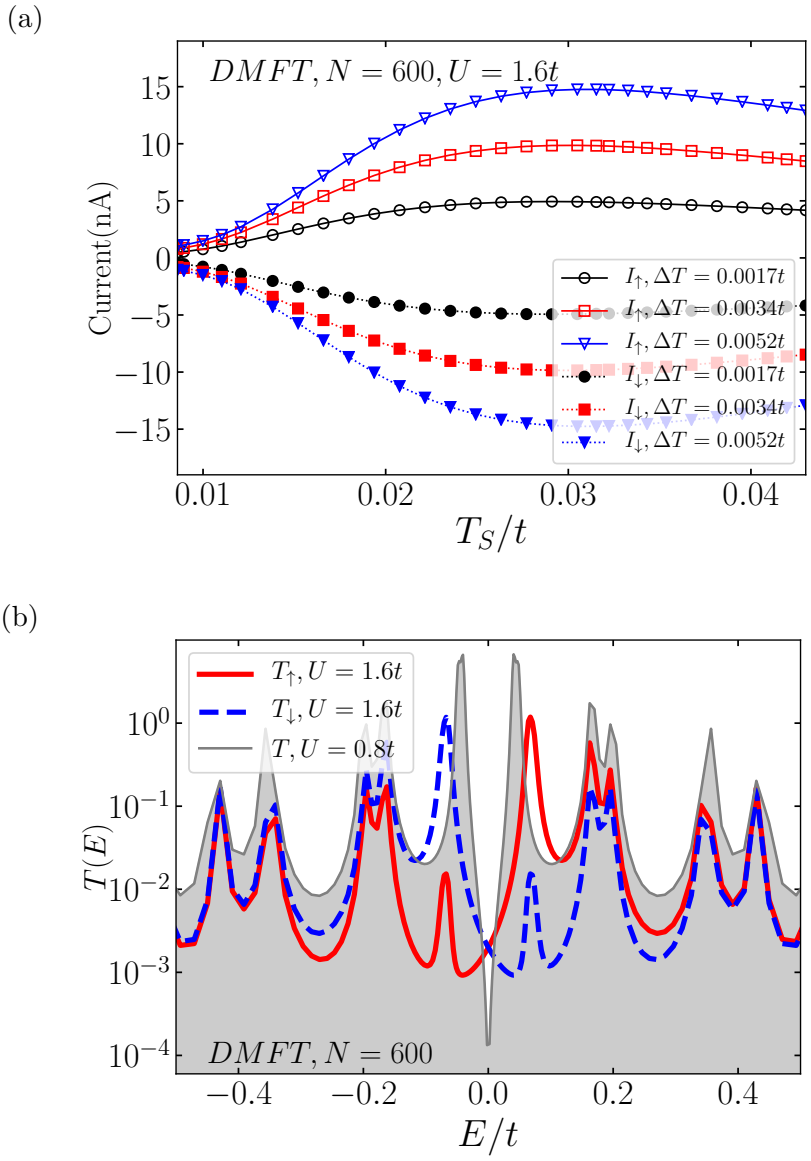

Figure A.1: Spin-resolved currents driven by the temperature gradient versus T_S with ΔT (a) and transmission coefficient (b) as a function of E/t for $N = 600$ at $U/t = 0.8$ and 1.6 using the real-space DMFT.

real-space

$$G_{0i\sigma}(\omega)^{-1} = G_{ii\sigma}(\omega)^{-1} + \Sigma_\sigma(\omega), \tag{A.2}$$

where the interacting Green's function of the whole system from the real-space Dyson equation is $G_{ij\sigma}(\omega)^{-1} = (\omega + \eta)I - t_{ij} - \Sigma_\sigma(\omega)$ with the identity matrix I and the hopping amplitude t_{ij}. To address the equations above, the NRG method is employed. In the computational point of view, the self-consistent solution is realized iteratively starting from the initial input of the Weiss field $G_{0i\sigma}(\omega)$ for each site. Then the mangetic solution on each site i is evaluated as $\langle S_i \rangle = \langle n_{i\uparrow} - n_{i\downarrow} \rangle$.

Combining with the NEGF, the responses of the spin-dependent current induced by the temperature difference obtained from the DMFT+NRG approximation are analogous to those obtained from the MFT level, as can be seen in Figure A.1(a). Here, the spin-up and spin-down currents with the same magnitude also flow in the opposite directions. As a result, there is only a net spin current I_{spin} generated in the device. When ΔT is fixed, these currents increase rapidly at low source temperature T_S. With further increasing T_S, these currents decrease slightly in the range of T_S studied. These behaviors are the consequence of the symmetry of the spin-up and spin-down transmission spectra with respect to zero energy, shown in Figure A.1(b).

A.2 The transmission coefficient under the particle-hole symmetry

As mentioned in the main text, the spin current driven by the thermal bias flows in the *meta* configuration, while it is blocked in the *ortho* and *para* configurations. This is interpreted by the transmission coefficient $T_\sigma(E)$ because such spin current is a function of $T_\sigma(E)$. We recall the transmission coefficient through in the device is estimated within the framework of the non-equilibrium Green's function

$$T_\sigma(E) = Tr[G^{r*}\Gamma_D G^r \Gamma_S]. \tag{A.3}$$

In the wide-band limit approximation, the transmission coefficient,

$$T_\sigma(E) \sim G^{r*}(E) G^r(E), \tag{A.4}$$

is entirely determined by the Green's functions. This represents a direct relation of the $T_\sigma(E)$ with the electronic properties of the graphene nanoflakes. Hence, we can use the Green's function for explaining the behaviors of the $T_\sigma(E)$. One starts from the definition of the retarded Green's function [179, 204]

$$G^r_{ij\sigma}(E) = -i \int \theta(t) \langle \{c_{i\sigma}(t), c^+_{j\sigma}(0)\} \rangle e^{-iEt} dt. \tag{A.5}$$

At half-filling, the particle-hole transformations for graphene are

$$\begin{aligned} c_{i\sigma} &\rightarrow (-1)^i c^+_{i\sigma}, \\ c^+_{i\sigma} &\rightarrow (-1)^i c_{i\sigma} \end{aligned} \tag{A.6}$$

where the factor $(-1)^i = \pm 1$ depends on whether i belongs to either the A graphene sublattice or the B graphene sublattice. Under these transformations, the retarded Green's function is expressed

$$\begin{aligned} G^r_{ij\sigma}(E) &= -i \int \theta(t) \langle \{(-1)^i c^+_{i\sigma}(t), (-1)^j c_{j\sigma}(0)\} \rangle e^{-iEt} dt \\ &= -i(-1)^{i+j} \int \theta(t) \langle \{c^+_{i\sigma}(t), c_{j\sigma}(0)\} \rangle e^{-iEt} dt, \\ G^r_{ij\sigma}(-E) &= -i(-1)^{i+j} \int \theta(t) \langle \{c^+_{i\sigma}(t), c_{j\sigma}(0)\} \rangle e^{iEt} dt. \end{aligned} \tag{A.7}$$

The complex conjugate of Eq. (A.5) is given by

$$(G^r_{ij\sigma})^*(E) = i \int \theta(t) \langle \{c^+_{i\sigma}(t), c_{j\sigma}(0)\} \rangle e^{iEt} dt. \tag{A.8}$$

Comparing Eq. (A.8) with Eq. (A.7), one gets the following relation

$$G^r_{ij\sigma}(-E) = (-1)^{i+j+1} (G^r_{ij\sigma})^*(E). \tag{A.9}$$

On the other hand, one has

$$T_\sigma(E) \sim \sum_{ij\sigma} (G^r_{ij\sigma})^*(E) G^r_{ij\sigma}(E), \tag{A.10}$$

$$T_\sigma(-E) \sim \sum_{ij\sigma} (G^r_{ij\sigma})^*(-E) G^r_{ij\sigma}(-E). \tag{A.11}$$

Using the relation (A.9), Eq. (A.11) can recast

$$T_\sigma(-E) \sim \sum_{ij\sigma} G^r_{ij\sigma}(E) (G^r_{ij\sigma})^*(E). \tag{A.12}$$

Comparing between Eq. (A.10) and Eq. (A.12), the transmission coefficient satisfies the following relation, $T_\sigma(E) = T_\sigma(-E)$, for all transport configurations in this work. This implies that the transmission is an even function in the absence of the intrinsic magnetization, yielding a zero current (without the back-gate voltage applied).

Now, examining the system in the antiferromagnetic state, the particle-hole symmetry is still preserved. However, the particle-hole transformations are modified as follows

$$\begin{aligned} c_{i\sigma} &\to (-1)^i c^+_{i\bar{\sigma}}, \\ c^+_{i\sigma} &\to (-1)^i c_{i\bar{\sigma}}. \end{aligned} \tag{A.13}$$

In this case, one obtains the relations below

$$\begin{aligned} G^r_{ij\sigma}(-E) &= (-1)^{i+j+1}(G^r_{ij\bar{\sigma}})^*(E), \\ T_\sigma(E) &= T_{\bar{\sigma}}(-E). \end{aligned} \tag{A.14}$$

These are correct for all configurations. Furthermore, one can change the role of spin and sublattice indices in the particle-hole transformations as the magnetic order coincides with the sublattices, corresponding particle-hole transformations are [179]

$$\begin{aligned} c_{i\sigma} &\to (-1)^i c^+_{j\sigma}, \\ c^+_{i\sigma} &\to (-1)^i c_{j\sigma}. \end{aligned} \tag{A.15}$$

When the leads are contacted with carbon atoms of different graphene sublattices, the invariance of the retarded Green's function under the new definition of the particle-hole transformations implies

$$\begin{aligned} G^r_{ij\sigma}(E) &= -i(-1)^{i+j}\int \theta(t)\langle\{c^+_{j\sigma}(t), c_{i\sigma}(0)\}\rangle e^{-iEt}dt \\ &= i\int \theta(t)\langle\{c^+_{j\sigma}(t), c_{i\sigma}(0)\}\rangle e^{-iEt}dt \end{aligned}$$

with $(-1)^{i+j} = -1$. Similarly

$$G^r_{ij\sigma}(-E) = i\int \theta(t)\langle\{c^+_{j\sigma}(t), c_{i\sigma}(0)\}\rangle e^{iEt}dt.$$

On the other hand, we have

$$(G^r_{ij\sigma})^*(E) = i\int \theta(t)\{\langle c^+_{i\sigma}(t), c_{j\sigma}(0)\}\rangle e^{iEt}dt.$$

This deduces

$$(G^r_{ij\sigma})^*(E) = -G^r_{ji\sigma}(-E). \tag{A.16}$$

From Eq. (A.16), the transmission coefficient in the *ortho* and *para* configurations becomes $T_\sigma(E) = T_\sigma(-E)$ and along with Eq. (A.14), resulting in $T_\sigma(E) = T_{\bar{\sigma}}(E)$. This results indicates that the spin-resolved transmission in these two configurations is prevented. Consequently, these configurations do not support any spin transport phenomena. In contrast, the invariance of the retarded Green's function under Eq.

(A.15) expressed in the *meta* configuration is

$$G^{rAA}_{ij\sigma}(E) = -i \int \theta(t) \langle \{ c^{+BB}_{j\sigma}(t), c^{BB}_{i\sigma}(0) \} \rangle e^{-iEt} dt.$$

Similarly

$$G^{rBB}_{ji\sigma}(-E) = i \int \theta(t) \langle \{ c^{+AA}_{i\sigma}(t), c^{AA}_{j\sigma}(0) \} \rangle e^{iEt} dt,$$

and together with

$$(G^{rAA}_{ij\sigma})^*(E) = i \int \theta(t) \langle \{ c^{+AA}_{i\sigma}(t), c^{AA}_{j\sigma}(0) \} \rangle e^{iEt} dt$$

yielding

$$(G^{rAA}_{ij\sigma})^*(E) = G^{rBB}_{ji\sigma}(-E) \tag{A.17}$$

where the AA and BB superscripts indicate that the leads are connected to carbon atoms belonging to the same graphene sublattice either A or B. The transmission coefficient in this case is estimated by the following relation $T^{AA}_{\sigma}(E) = T^{BB}_{\sigma}(-E)$ and along with Eq. (A.14) one eventually gets

$$T^{AA}_{\sigma}(E) = T^{BB}_{\bar{\sigma}}(E). \tag{A.18}$$

Eq. (A.14) and (A.18) demonstrate the splitting of the transmission coefficient via the spin-up and spin-down states, and the symmetry of the spin-resolved transmission coefficient in the *meta* configuration. In addition, Eq. (A.18) implies the symmetry of $T_{\sigma}(E)$ via *graphene sublattice-symmetry*. In particular, $T_{\sigma}(E)$ in the case when the leads connect to the A graphene sublattice is equal to $T_{\bar{\sigma}}(E)$ in the case when the leads connect to the B graphene sublattice. This yields the change of the flowing direction of the spin current. Since the graphene sublattice-symmetry is broken the symmetry of the spin-resolved transmission coefficient is predicted to vanish. This effect was reported in the work of Valli et al. [179] for small graphene nanoflake $N = 54$. However, the thermally induced spin current in the nanoflakes when breaking the graphene sublattice-symmetry has yet to been studied. Therefore, we will discuss this investigation in the next section.

A.3 The impact of the degree of chiral symmetric breaking on magnetism and transport properties in graphene nanoflakes

In addition to the findings obtained in terms of the symmetries of the Hubbard Hamiltonian, we focus here on the responses of the thermally governed spin current when the graphene sublattice-symmetry is broken, quintessentially by depositing the graphene nanoflakes on a substrate. One of the candidates chosen to realize the thermal devices is hBN [205]. According to the DFT calculation of Ref. [206] indicates that one of two inequivalent C atoms of graphene located on top of the B atom and the other centered over a hBN ring is the most stable configuration. This gives rise to the breaking of the graphene sublattice-symmetry due to the asymmetric absorption of C on the substrate wherein two graphene sublattices undergo the different chemical environment [39]. So, the graphene nanoflake can be described in the following Hubbard Hamiltonian within the mean-field level as

$$\begin{aligned} H = &- t \sum_{\langle i,j\rangle\sigma} (c^{+}_{i\sigma} c_{j\sigma} + h.c) + U \sum_{i} (\langle n_{i\downarrow}\rangle - \frac{1}{2}) n_{i\uparrow} + (\langle n_{i\uparrow}\rangle - \frac{1}{2}) n_{i\downarrow} - \langle n_{i\uparrow}\rangle\langle n_{i\downarrow}\rangle + \frac{1}{4} \\ &- \epsilon (\sum_{i\in A\sigma} n_{i\sigma} - \sum_{i\in B\sigma} n_{i\sigma}) \end{aligned} \tag{A.19}$$

where ϵ denotes the effect of hBN on the GNFs or can be understood as the sublattice potential. Before analyzing the thermally excited current through the device, let us begin with the magnetic properties on the graphene nanoflakes. Calculations show that the sublattice potential ϵ/t has a tendency to suppress the magnetic order in the graphene nanoflakes which appears in bulk graphene [141]. Therefore, the value of U_c/t is shifted to higher value when increasing ϵ/t, as shown in Figure A.2. This is considered as a consequence of the opening of the gap caused by the graphene nanoflake-substrate interaction [206]. In comparison with large nanoflakes, namely $N = 600$, where U_c/t goes up nearly linearly, the value of U_c/t of small nanoflakes, as in $N = 96$, increases much slower with rising ϵ/t. As a result, the slope of the $U - \epsilon$ phase boundary of $N = 600$ is higher than that of $N = 96$. This difference is due to the existence of a larger gap in small nanoflakes in the absence of ϵ compared to large nanoflakes. Accordingly, for ϵ/t less than the gap, U_c/t is invariant. According to Figure A.2(a), a transition from the paramagnetic phase to the antiferromagnetic insulating phase occurs at higher interaction compared

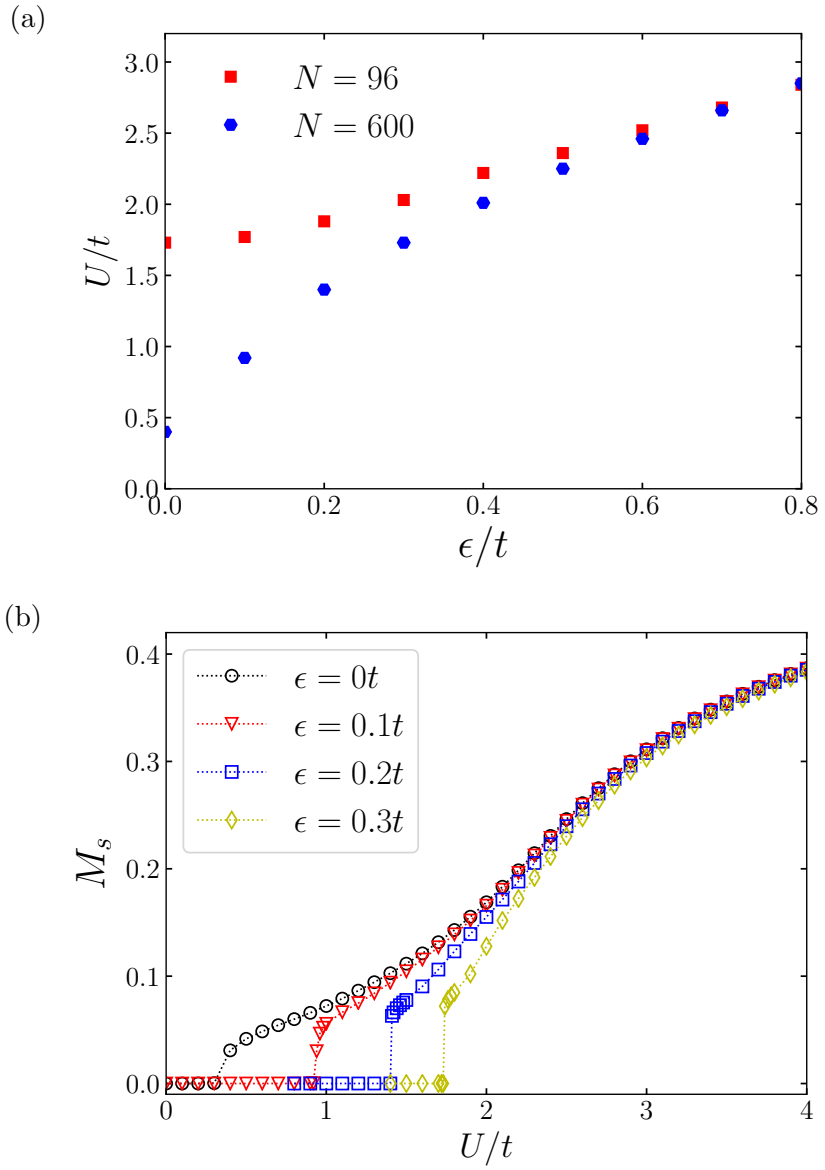

Figure A.2: Phase diagram of graphene nanoflakes: $N = 96$ and $N = 600$ using the mean-field Hubbard model (a). Staggered magnetization on the edges of graphene nanoflake of 600 sites for $\epsilon = 0t$, $0.1t$, $0.2t$ and $0.3t$ (b).

to the GNFs with $\epsilon/t = 0$. Remarkably, except for the partial quench of magnetic moments, the antiferromagnetic pattern of graphene nanoflakes is still preserved [39], as indicated in Figure A.2(b).

Figure A.3 exhibits that the spin-resolved current induced by the temperature difference at $\Delta T = 0.0052t$ and $T_S = 0.026t$ ($\approx 300K$) is controlled by ϵ/t. Since ϵ/t does not enhance dramatically the spin-resolved current, a very tiny spin-resolved current is generated in $N = 54$ and $N = 96$ nanoflakes at room temperature, so they are neglected in this study. Taking a first glance, one finds a point of ϵ/t, hereinafter re-

ferred to as ϵ_q/t, where the spin current I_{spin} is suppressed completely (it means that the spin-up current is equal to the spin-down current, see the inset of Figure A.3). The value of ϵ_q is around $0.08t - 0.09t$. When $\epsilon < \epsilon_q$, the spin-up and spin-down currents flow either in the opposite directions or in the same direction depending on ϵ/t. In detail, at first the spin-up current flowing from the source to the drain increases slightly, then decreases relatively rapidly to zero and subsequently drops to a negative value corresponding to changing its direction. In contrast to the spin-up current, the spin-down current reduces gradually and keeps the direction from the drain to the source. As a consequence, I_{spin} is larger than I_{charge}. As $\epsilon \geq \epsilon_q$ I_{spin} is approximately zero, there is only net I_{charge}, nevertheless, its magnitude decreases gradually to approximately zero. With much higher ϵ/t, no current is detected.

Figure A.4 displays the spin-up and spin-down currents with respect to U/t with some values ϵ/t for two graphene nanoflakes: $N = 294$ and 600. As observed, a vanishing current flows through the device when U is greater than U_c^{bulk}. A significant spin-resolved current is detected when the spin on the edge sites is polarized. More detailed, the spin-up current skyrockets and reaches a peak, after that it goes down to zero. Compared to the spin-up current, the spin-down current, being smaller in

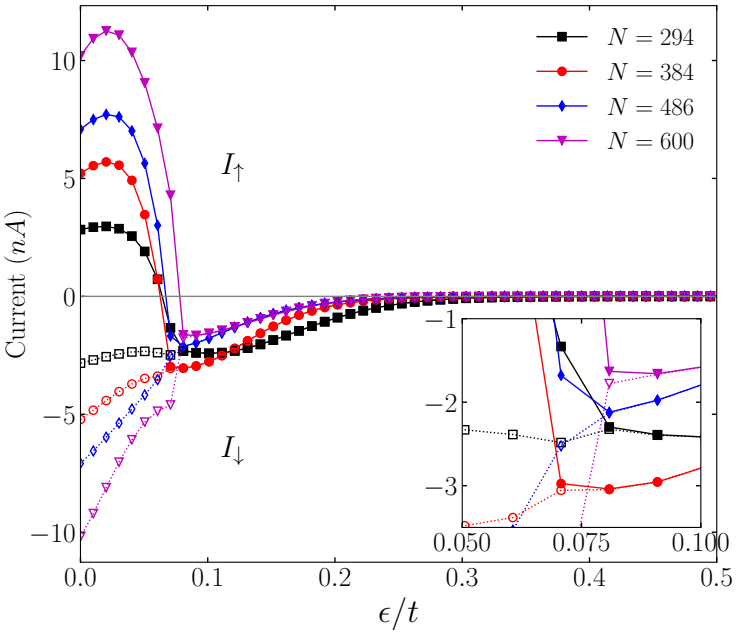

Figure A.3: The dependence of the spin-up and spin-down currents on ϵ/t at $T_S = 0.026t$ and $\Delta T = 0.0052t$ for several hexagonal graphene nanoflakes with the zigzag edge. Herein the repulsive Coulomb energy is U_h/t corresponding to each nanoflake, see Table 5.1, $\eta = 10^{-2}t$ and $\Gamma = 0.02t$.

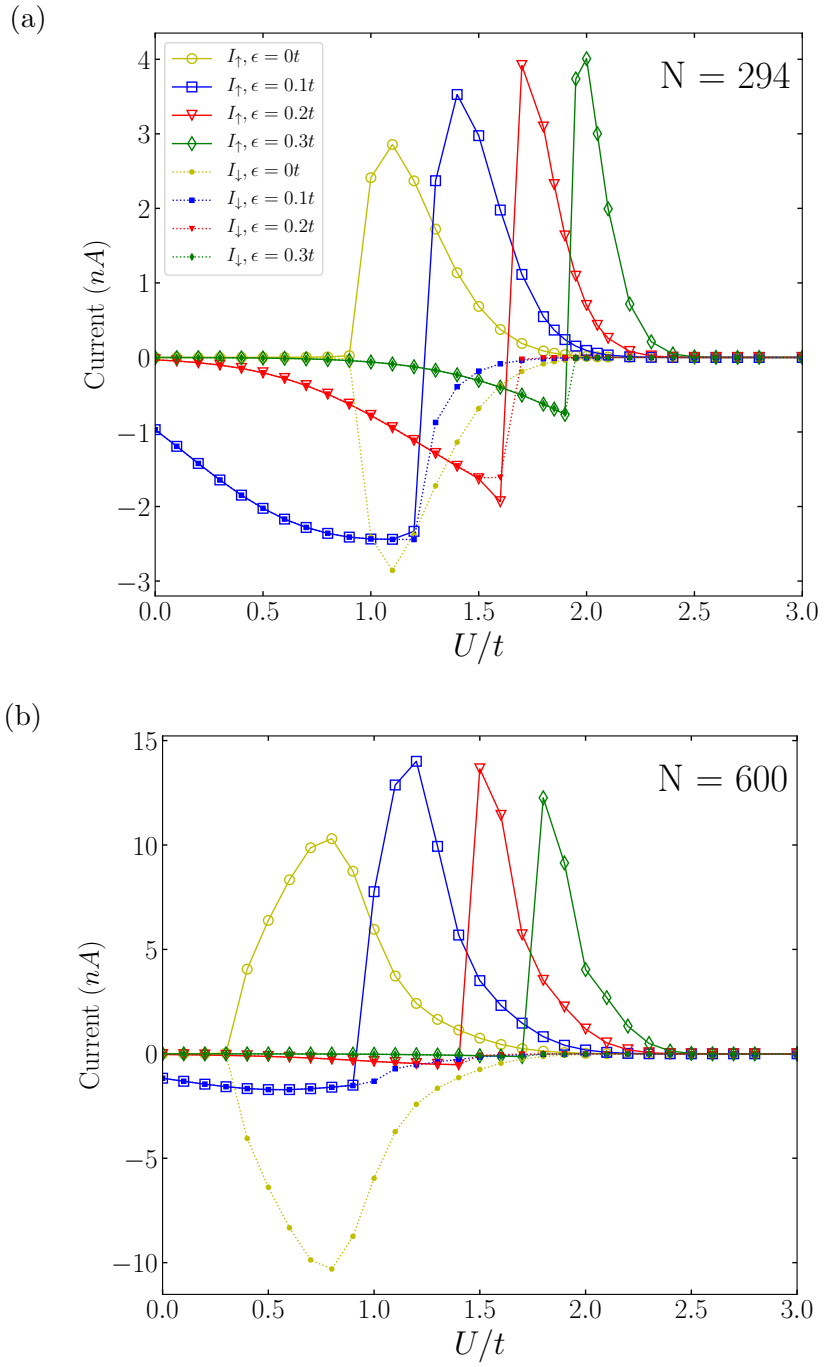

Figure A.4: Spin-resolved current as a function of U/t for several values of $\epsilon = 0t$, $0.1t$, $0.2t$ and $0.3t$ at $T_S = 0.026t$ and $\Delta T = 0.0052t$ for $N = 294$ (a) and $N = 600$ (b) with $\eta = 10^{-2}t$ and $\Gamma = 0.02t$.

magnitude, flows in the opposite direction and its magnitude decreases gradually to zero. It is worth noting that for $N = 600$, the spin-down current is very small, while the spin-up current is rather large, resulting in a nearly complete spin-filtering effect. Moreover, with increasing ϵ/t, the maximum value of the spin-up current moves to

higher U/t due to the shifting to the higher value of U_c/t and the magnitude of the maximum value is higher than the corresponding value with $\epsilon = 0t$. In the paramagnetic state, there merely exists net charge current because the transmission is asymmetric around $E/t = 0$, *i.e.*, $T(-E) \neq T(E)$. In addition, the transmission peaks below zero energy $E/t = 0$ are much larger than those above zero energy, resulting in a negative net charge current. The increase of the I_{charge} is due to the transmission peaks being closer to zero energy. Similar to the symmetric case, even when the edge magnetization of the graphene nanoflakes is switched on, the transmission through the device is spin-polarized. Figure A.5 shows the asymmetry of the spin-up transmission and the spin-down transmission with respect to zero energy, $T_\sigma(E) \neq T_\sigma(-E)$, and $T_\sigma(E) \neq T_{\bar{\sigma}}(-E)$ which is a consequence of the charge imbalance between the two graphene sublattices [39]. The part of the spin-up transmission spectrum above $E/t = 0$ gives the bigger overlap with the Fermi-Dirac distribution difference than that below $E/t = 0$. As a result, the spin-up current with positive sign flows from the left to the right lead. The opposite trend is recorded for the spin-down transmission spectrum as well as the spin-down current. Furthermore, increasing ϵ/t make the graphene nanoflake possible to become nonmagnetic, so the transmission coefficient is not spin-polarized with the dominance of the transmission peaks below $E/t = 0$. Thus one obtains a negative net charge current. With further increasing ϵ, the transmission peaks move far away from $E/t = 0$. Therefore, the net charge current decreases gradually to zero.

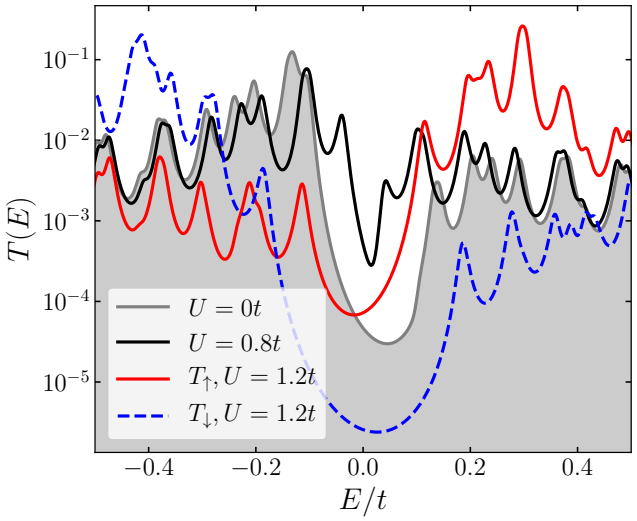

Figure A.5: Spin-resolved transmission spectra with respect to E/t for $N = 600$ at $U = 0t$, $0.8t$, $1.2t$ and a fixed $\epsilon = 0.1t$ with $\eta = 10^{-2}t$ and $\Gamma = 0.02t$.

In summary, our calculations show that the graphene sublattice symmetry breaking

can generate a dramatic spin current subjected to the temperature gradient and a nearly complete spin-filtering effect in the graphene nanoflakes deposited on hBN. This result indicates the possibility of the realization of such spin-caloritronic devices in experiment.

Bibliography

[1] K.S. Novoselov, A.K. Geim, S.V. Morozov, D. Jiang, Y. Zhang, S.V. Dubonos, I.V. Grigorieva, and A.A. Firsov. Electric field effect in atomically thin carbon films. *Science*, 306:666, 2004.

[2] C. Berger, Z. Song, T. Li, X. Li, A.Y. Ogbazghi, R. Feng, Z. Dai, A.N. Marchenkov, E.H. Conrad, P.N. First, and W.A. de Heer. Ultrathin epitaxial graphite: 2D electron gas properties and a route toward graphene-based nanoelectronics. *The Journal of Physical Chemistry B*, 108:19912, 2004.

[3] P.R. Wallace. The band theory of graphite. *Physical Review*, 71:622, 1947.

[4] D.V. Tuan. *Charge and spin transport in disordered graphene-based materials*, chapter 2: Electronic and transport properties of graphene. Springer International Publishing Switzerland, 2016.

[5] K.I. Bolotin, K.J. Sikes, Z. Jiang, M. Klima, G. Fudenberg, J. Hone, P. Kim, and H.L. Stormer. Ultrahigh electron mobility in suspended graphene. *Solid State Communications*, 146:351, 2008.

[6] C. Berger, Z. Song, X. Li, X. Wu, N. Brown, C. Naud, D. Mayou, T. Li, J. Hass, A.N. Marchenkov, E.H. Conrad, P.N. First, and W.A. de Heer. electronic confinement and coherence in patterned epitaxial graphene. *Science*, 312:1191, 2006.

[7] A.A. Balandin, S. Ghosh, W. Bao, I. Calizo, D. Teweldebrhan, F. Miao, and C.N. Lau. Superior thermal conductivity of single-layer graphene. *Nano Letters*, 8(3):902, 2008.

[8] S. Bak, D. Kim, and H. Lee. Graphene quantum dots and their possible energy applications: A review. *Current Applied Physics*, 16:1192 – 1201, 2016.

[9] T.P.D. Shareena, D. McShan, A.K. Dasmahapatra, and P.B. Tchounwou. A review on graphene-based nanomaterials in biomedical applications and risks in environment and health. *Nano-Micro Letters*, 10:53, 2018.

[10] Z. Jin, P. Owour, S. Lei, and L. Ge. Graphene, graphene quantum dots and their applications in optoelectronics. *Current Opinion in Colloid & Interface Science*, 20:439, 2015.

[11] S. Roche and S.O Valenzuela. Graphene spintronics: puzzling controversies and challenges for spin manipulation. *Journal of Physics D: Applied Physics*, 47(9):094011, 2014.

[12] M.H.D. Guimarães, P.J. Zomer, J. Ingla-Aynés, J.C Brant, and B.J. van Wees. Controlling spin relaxation in hexagonal BN-encapsulated graphene with a transverse electric field. *Physical Review Letters*, 113:086602, 2014.

[13] W. Han, R.K. Kawakami, M. Gmitra, and J. Fabian. Graphene spintronics. *Nature Nanotechnology*, 9:794, 2014.

[14] M.V. Kamalakar, C. Groenveld, A. Dankert, and S.P. Dash. Long distance spin communication in chemical vapour deposited graphene. *Nature Communications*, 6:6766, 2015.

[15] A. Dankert, M.V. Kamalakar, J. Bergsten, and S.P. Dash. Spin transport and precession in graphene measured by nonlocal and three-terminal methods. *Applied Physics Letters*, 104:192403, 2014.

[16] M. Drögeler, F. Volmer, M. Wolter, B. Terrés, K. Watanabe, T. Taniguchi, G. Güntherodt, C. Stampfer, and B. Beschoten. Nanosecond spin lifetimes in single- and few-layer graphene-hBN heterostructures at room temperature. *Nano Letters*, 11:6050, 2014.

[17] P. Ruffieux, S. Wang, B. Yang, C. Sánchez-Sánchez, J. Liu, T. Dienel, L. Talirz, P. Shinde, C.A. Pignedoli, D. Passerone, T. Dumslaff, X. Feng, K. Müllen, and R. Fasel. On-surface synthesis of graphene nanoribbons with zigzag edge topology. *Nature*, 531:489, 2016.

[18] R.S. Jordan, Y.L. Li, C.-W. Lin, R.D. McCurdy, J.B. Lin, J.L. Brosmer, K.L. Marsh, S.I. Khan, K.N. Houk, R.B. Kaner, and Y. Rubin. Synthesis of N = 8 armchair graphene nanoribbons from four distinct polydiacetylenes. *Journal of the American Chemical Society*, 139(44):15878, 2017.

[19] J.J. Palacios, J. Fernández-Rossier, and L. Brey. Vacancy-induced magnetism in graphene and graphene ribbons. *Physical Review B*, 77:195428, 2008.

[20] Y. Wang, Y. Huang, Y. Song, X. Zhang, Y. Ma, J. Liang, and Y. Chen. Room-temperature ferromagnetism of graphene. *Nano Letters*, 9(1):220, 2009.

[21] R.R. Nair, I.-L. Tsai, M. Sepioni, O. Lehtinen, J. Keinonen, A.V. Krasheninnikov, A.H. Castro Neto, M.I. Katsnelson, A.K. Geim, and I.V. Grigorieva. Dual origin of defect magnetism in graphene and its reversible switching by molecular doping. *Nature Communications*, 4:2010, 2013.

[22] Q. Miao, L. Wang, Z. Liu, B. Wei, F. Xu, and W. Fei. Magnetic properties of N-doped graphene with high Curie temperature. *Scientific Reports*, 6:21832, 2016.

[23] P. Bloński, J.. Tuček, Z. Sofer, V. Mazánek, M. Petr, M. Pumera, M. Otyepka, and R. Zbořil. Doping with graphitic Nitrogen triggers ferromagnetism in graphene. *Journal of the American Chemical Society*, 139(8):3171, 2017.

[24] L. Fritz and M. Vojta. The physics of Kondo impurities in graphene. *Reports on Progress in Physics*, 76:032501, 2013.

[25] O.V. Yazyev and L. Helm. Defect-induced magnetism in graphene. *Physical Review B*, 75:125408, 2007.

[26] K. Wakabayashi, K.-I Sasaki, T. Nakanishi, and T. Enoki. Electronic states of graphene nanoribbons and analytical solutions. *Science and Technology of Advanced Materials*, 11:054504, 2010.

[27] G.Z. Magda, X.Z. Jin, I. Hagymási, P. Vancsó, Z. Osváth, P. Nemes-Incze, C. Hwang, L.P. Biró, and L. Tapasztó. Room-temperature magnetic order on zigzag edges of narrow graphene nanoribbons. *Nature*, 514:608, 2014.

[28] S. Bhowmick and V.B. Shenoy. Edge state magnetism of single layer graphene nanostructures. *The Journal of Chemical Physics*, 128:244717, 2008.

[29] M. Modarresi, B.S. Kandemir, M.R. Roknabadi, and N. Shahtahmasebi. Spin dependent transport through triangular graphene quantum dot in the presence of Rashba type spin–orbit coupling. *Journal of Magnetism and Magnetic Materials*, 367:81, 2014.

[30] W. Zhang. Voltage-driven spintronic logic gates in graphene nanoribbons. *Scientific Reports*, 4:6320, 2014.

[31] S.S. Gregersen, S.R. Power, and A.-P. Jauho. Nanostructured graphene for spintronics. *Physical Review B*, 95:121406, 2017.

[32] M.H.D Guimarães, J.J. van den Berg, I.J. Vera-Marun, P.J Zomer, and B.J. van Wees. Spin transport in graphene nanostructures. *Physical Review B*, 90:235428, 2014.

[33] K. Luo and W. Sheng. Many-body effects in the spin-polarized electron transport through graphene nanoislands. *Journal of Applied Physics*, 115:053705, 2014.

[34] Y. Lu, S. Wei, J. Jin, W. Lu, and L. Wang. Edge-state-induced energy splitting of exciton triplet states in graphene nanoflakes. *Journal of Applied Physics*, 120:204301, 2016.

[35] K. Luo and W. Sheng. Bias voltage control of magnetic phase transitions in graphene nanojunctions. *Nanotechnology*, 26:345303, 2015.

[36] P. Zhao, Q.H. Wu, D.S. Liu, and G. Chen. Spin-filtering, giant magnetoresistance, rectifying and negative differential resistance effects in planar four-coordinate Fe complex with graphene nanoribbon electrodes. *The Journal of Chemical Physics*, 140:044311, 2014.

[37] C. Cao, M.-Q. Long, X.-J. Zhang, and X.-C. Mao. Giant magnetoresistance and spin-filtering effects in zigzag graphene and hexagonal boron nitride based heterojunction. *Physics Letters A*, 379:1527, 2015.

[38] L.-L. Cui, M.-Q. Long, X.-J. Zhang, X.-M. Li, D. Zhang, and B.-C. Yang. Spin-dependent transport properties of hetero-junction based on zigzag graphene nanoribbons with edge hydrogenation and oxidation. *Physics Letters A*, 380:730, 2016.

[39] A. Valli, A. Amaricci, V. Brosco, and M. Capone. Quantum interference assisted spin filtering in graphene nanoflakes. *Nano Letters*, 18(3):2158, 2018.

[40] M. Zeng, Y. Feng, and G. Liang. Graphene-based spin caloritronics. *Nano Letters*, 11(3):1369, 2011.

[41] H.-H. Fu, L. Gu, and D.-D. Wu. A spin-Seebeck diode with a negative differential spin-Seebeck effect in a hydrogen-terminated zigzag silicene nanoribbon

heterojunction. *Physical Chemistry Chemical Physics*, 18:12742, 2016.

[42] Y.-R. Yang, Z.-Q. Zhang, L. Gu, and H.-H. Fu. Spin-dependent Seebeck effect in zigzag black phosphorene nanoribbons. *RSC Advances*, 6:44019, 2016.

[43] Z. Su, Y. An, X. Wei, and Z. Yang. Spin-dependent thermoelectronic transport of a single molecule magnet $Mn(dmi)_2$. *The Journal of Chemical Physics*, 140(20):204707, 2014.

[44] M. Zeng, L. Shen, M. Zhou, C. Zhang, and Y. Feng. Graphene-based bipolar spin diode and spin transistor: Rectification and amplification of spin-polarized current. *Physical Review B*, 83:115427, 2011.

[45] M. Zeng, W. Huang, and G. Liang. Spin-dependent thermoelectric effects in graphene-based spin valves. *Nanoscale*, 5:200, 2013.

[46] D. Geng, B. Wu, Y. Guo, L. Huang, Y. Xue, J. Chen, G. Yu, L. Jiang, W. Hu, and Y. Liu. Uniform hexagonal graphene flakes and films grown on liquid copper surface. *Proceedings of the National Academy of Sciences of the United States of America*, 109(21):7992, 2012.

[47] H.-H. Fu, D.-D. Wu, Z.-Q. Zhang, and L. Gu. Spin-dependent Seebeck effect, thermal colossal magnetoresistance and negative differential thermoelectric resistance in zigzag Silicene nanoribbon heterojunction. *Scientific Reports*, 5:10547, 2015.

[48] M.O. Goerbig. Electronic properties of graphene in a strong magnetic field. *Reviews of Modern Physics*, 83:1193, 2011.

[49] B. Gharekhanlou and S. Khorasani. *Graphene: Properties, synthesis and applications*, chapter 1: An overview of tight-binding method for two-dimensional carbon structures, pages 1–36. ISBN 978-1-61470-949-7. Nova Science Publisher, Inc., 2011.

[50] A.H. Castro Neto, F. Guinea, N.M.R. Peres, K.S. Novoselov, and A.K. Geim. The electronic properties of graphene. *Reviews of Modern Physics*, 81(1):109, 2009.

[51] S. Reich, J. Maultzsch, and C. Thomsen. Tight-binding description of graphene. *Physical Review B*, 66:035412, 2002.

[52] W. Wu, Y.-H. Chen, H.-S. Tao, N.-H. Tong, and W.-M. Liu. Interacting dirac fermions on honeycomb lattice. *Physical Review B*, 82:245102, 2010.

[53] T. Ando. Theory of electronic states and transport in carbon nanotubes. *Journal of the Physical Society of Japan*, 74:777, 2005.

[54] M.I. Katsnelson, K.S. Novoselov, and A.K. Geim. Chiral tunnelling and the Klein paradox in graphene. *Nature Physics*, 2:620, 2006.

[55] H. Söde, L. Talirz, O. Gröning, C.A. Pignedoli, R. Berger, X. Feng, K. Müllen, R. Fasel, and P. Ruffieux. Electronic band dispersion of graphene nanoribbons via Fourier-transformed scanning tunneling spectroscopy. *Physical Review B*, 91:045429, 2015.

[56] L. Talirz, H. Söde, T. Dumslaff, S. Wang, J.R. Sanchez-Valencia, J. Liu, P. Shinde, C.A. Pignedoli, L. Liang, V. Meunier, N.C. Plumb, M. Shi, X. Feng, A. Narita, K. Müllen, R. Fasel, and P. Ruffieux. On-surface synthesis and characterization of 9-atom wide armchair graphene nanoribbons. *ACS Nano*, 11:1380, 2017.

[57] K.A. Simonov, A.V. Generalov, A.S. Vinogradov, G.I. Svirskiy, A.A. Cafolla, C. McGuinness, T. Taketsugu, A. Lyalin, N. Martensson, and A.B. Preobrajenski. Synthesis of armchair graphene nanoribbons from the 10,10′-dibromo-9,9′-bianthracene molecules on Ag(111): The role of organometallic intermediates. *Scientific Reports*, 8(1):3506, 2018.

[58] X. Dong, L. Wang, K. Li, H. Zheng, Y. Wang, Y. Meng, H. Shu, H.-K. Mao, S. Feng, and C. Jin. Tailored synthesis of the narrowest zigzag graphene nanoribbon structure by compressing the lithium acetylide under high temperature. *Journal of Physical Chemistry C*, 122(35):20506, 2018.

[59] X. Zhang, O.V. Yazyev, J. Feng, L. Xie, C. Tao, Y.-C. Chen, L. Jiao, Z. Pedramrazi, A. Zettl, S.G. Louie, H. Dai, and M.F. Crommie. Experimentally engineering the edge termination of graphene nanoribbons. *ACS Nano*, 7(1):198, 2013.

[60] W. Chen, F. Li, C. Wu, and T. Guo. Optical properties of fluorescent zigzag graphene quantum dots derived from multi-walled carbon nanotubes. *Applied Physics Letters*, 104:063109, 2014.

[61] G. Rajender, U. Goswami, and P.K. Giri. Solvent dependent synthesis of edge-controlled graphene quantum dots with high photoluminescence quantum yield and their application in confocal imaging of cancer cells. *Journal of Colloid and Interface Science*, 541:387, 2019.

[62] N. Merino-Díez, A. Garcia-Lekue, E. Carbonell-Sanromà, J. Li, M. Corso, L. Colazzo, F. Sedona, D. Sánchez-Portal, J.I. Pascual, and D.G. de Oteyza. Width-dependent band gap in armchair graphene nanoribbons reveals Fermi level pinning on Au(111). *ACS Nano*, 11:11661, 2017.

[63] Y.W. Son, M.L. Cohen, and S.G. Louie. Energy gaps in graphene nanoribbons. *Physical Review Letters*, 97:216803, 2006.

[64] C. Tao, L. Jiao, O.V. Yazyev, Y.-C. Chen, J. Feng, X. Zhang, R.B. Capaz, J.M. Tour, A. Zettl, S.G. Louie, H. Dai, and M.F. Crommie. Spatially resolving edge states of chiral graphene nanoribbons. *Nature Physics*, 7:616, 2011.

[65] A. Mielke. *Many-Body Physics: From Kondo to Hubbard*, volume 5, chapter 11: The Hubbard model and its properties, pages 11.1–11.26. Forschungszentrum Jülich, 2015.

[66] J. Hubbard. Electron correlations in narrow energy bands. *Proceedings of the Royal Society of London*, 276(1365):238, 1963.

[67] J. Kanamori. Electron correlation and ferromagnetism of transition metals. *Progress of Theoretical Physics*, 30(3):275, 1963.

[68] M.C. Gutzwiller. Effect of correlation on the ferromagnetism of transition metals. *Physical Review Letters*, 10:159, 1963.

[69] R.T. Scaletttar. *Quantum materials: Experiments and theory*, volume 6, chapter 4: An introduction to the Hubbard Hamiltonian, pages 4.1 – 4.29. Forschungszentrum Jülich, 2016.

[70] E.H. Lieb. Two theorems on the Hubbard model. *Physical Review Letters*, 62(10):1201, 1989.

[71] Diep The Hung. *Theory of magnetism: Application to surface physics*. World Scientific Publishing Co. Pte. Ltd, 5 Toh Tuck Link, Singapore 596224, 2014.

[72] P. Farkasovsky. Ground state properties of the simplified Hubbard model. *Modern Physics Letters B*, 6(20):1245, 1992.

[73] M. Golor, T.C. Lang, and S. Wessel. Quantum Monte Carlo studies of edge magnetism in chiral graphene nanoribbons. *Physical Review B*, 87:155441, 2013.

[74] C.N. Varney, C.-R. Lee, Z.J. Bai, S. Chiesa, M. Jarrell, and R.T. Scalettar. Quantum Monte Carlo study of the two-dimensional fermion Hubbard model. *Physical Review B*, 80:075116, 2009.

[75] V.M.M. Alvarez, J.E.B. Vargas, M. Berdakin, and L.E.F.F. Torres. Topological states of non-Hermitian systems. *The European Physical Journal Special Topics*, 227:1295, 2018.

[76] J. Maciejko, T.L. Hughes, and S.C. Zhang. The quantum spin Hall effect. *Annual Review of Condensed Matter Physics*, 2:31, 2011.

[77] B. Simon. Holonomy, the quantum adiabatic theorem and Berry's phase. *Physical Review Letters*, 51:2167, 1983.

[78] C.L. Kane and E.J. Mele. Quantum spin Hall effect in graphene. *Physical Review Letters*, 95:226801, 2005.

[79] C.L. Kane and E.J. Mele. Z_2 topological order and the quantum spin Hall effect. *Physical Review Letters*, 95:146802, 2005.

[80] B.A. Bernevig and S.C. Zhang. Quantum spin Hall effect. *Physical Review Letters*, 96:106802, 2006.

[81] F.D.M. Haldane. Model for a quantum Hall effect without Landau levels: Condensed-matter realization of the "Parity anomaly". *Physical Review Letters*, 61:2015, 1988.

[82] H. Buhmann. The quantum spin Hall effect. *Journal of Applied Physics*, 109:102409, 2011.

[83] S. Rachel and K. Le Hur. Topological insulators and Mott physics from the Hubbard interaction. *Physical Review B*, 82:075106, 2010.

[84] D. Zheng, G.-M. Zhang, and C. Wu. Particle-hole symmetry and interaction effects in the Kane-Mele-Hubbard model. *Physical Review B*, 84:205121, 2011.

[85] D. Gosálbez-Martínez, D. Soriano, J.J. Palacios, and J. Fernández-Rossier. Spin-filtered edge states in graphene. *Solid State Communications*, 152:1469, 2012.

[86] Y. Li, E. Zhang, B. Gong, and S. Zhang. Intrinsic spin-orbit coupling in zigzag and armchair graphene nanoribbons. *Journal of Nanomaterials*, 2011:364897, 2011.

[87] C.-H. Chung, D.-H. Lee, and S.-P. Chao. Kane-Mele Hubbard model on a zigzag ribbon: stability of the topological edge states and quantum phase transitions. *Physical Review B*, 90:035116, 2014.

[88] Z.-F. Liu, Q.-P. Wu, A.-X. Chen, X.-B. Xiao, N.-H. Liu, and G.-X. Miao. Helical edge states and edge-state transport in strained armchair graphene nanoribbons. *Scientific Reports*, 7:8854, 2017.

[89] M. Bercx, M. Hohenadler, and F.F. Assaad. Kane-Mele-Hubbard model on the π-flux honeycomb lattice. *Physical Review B*, 90:075140, 2014.

[90] W. Wu, S. Rachel, W.M. Liu, and K. Le Hur. Quantum spin Hall insulators with interactions and lattice anisotropy. *Physical Review B*, 85:205102, 2012.

[91] M. Laubach, J. Reuther, R. Thomale, and S. Rachel. Rashba spin-orbit coupling in the Kane-Mele-Hubbard model. *Physical Review B*, 90:165136, 2014.

[92] T.-S. Zeng, W. Zhu, J.-X. Zhu, and D.N. Sheng. Nature of continuous phase transitions in interacting topological insulators. *Physical Review B*, 96:195118, 2017.

[93] H. Bruus and K. Flensberg. *Many-body quantum theory in condensed matter physics*. Oxford University Press Inc., New York, 2004.

[94] F. Lechermann. *The LDA+DMFT approach to strongly correlated materials*, volume 1, chapter 3: Model Hamiltonians and basic techniques, pages 3.1–3.29. Forschungszentrum Jülich, 2011.

[95] H. Feldner, Z.Y. Meng, A. Honecker, D. Cabra, W. Stefan, and F.F. Assaad. Magnetism of finite graphene samples: Mean-field theory compared with Exact

diagonalization and Quantum Monte Carlo simulation. *Physical Review B*, 81:115416, 2010.

[96] Y. Claveau, B. Arnaud, and S. Di Matteo. Mean-field solution of the Hubbard model: The magnetic phase diagram.

[97] A. Altintaş and A.D. Güçlü. Defect induced Anderson localization and magnetization in graphene quantum dots. *Solid State Communications*, 281:44, 2018.

[98] M. Hohenadler, F.P. Toldin, I.F. Herbut, and F.F. Assaad. Phase diagram of the Kane-Mele-Coulomb model. *Physical Review B*, 90:085146, 2014.

[99] S. Krompiewski. Edge magnetism of finite graphene-like nanoribbons in the presence of intrinsic spin–orbit interaction and perpendicular electric field. *Nanotechnology*, 27(31):315201, 2016.

[100] M. Hohenadler, Z.Y. Meng, T.C. Lang, S. Wessel, A. Muramatsu, and F.F Assaad. Quantum phase transitions in the Kane-Mele-Hubbard model. *Physical Review B*, 85:115132, 2012.

[101] S.-L. Yu, X.C. Xie, and J.-X. Li. Mott physics and topological phase transition in correlated Dirac fermions. *Physical Review Letters*, 107:010401, 2011.

[102] M. Raczkowski, R. Peters, T.T. Phùng, N. Takemori, F.F. Assaad, A. Honecker, and J. Vahedi. The hubbard model on the honeycomb lattice: from static and dynamical mean-field theories to lattice quantum monte carlo simulations. *arXiv:1908.04307*, 2019.

[103] Oleg V. Yazyev. Emergence of magnetism in graphene materials and nanostructures. *Reports on Progress in Physics*, 73:056501, 2010.

[104] V.L.J. Joly, M. Kiguchi, S.-J. Hao, K. Takai, T. Enoki, R. Sumii, K. Amemiya, H. Muramatsu, T. Hayashi, Y.A. Kim, M. Endo, J. Campos-Delgado, F. López-Urías, A. Botello-Méndez, H. Terrones, M. Terrones, and M.S. Dresselhaus. Observation of magnetic edge state in graphene nanoribbons. *Physical Review B*, 81:245428, 2010.

[105] M. Slota, A. Keerthi, W.K. Myers, E. Tretyakov, M. Baumgarten, A. Ardavan, H. Sadeghi, C.J. Lambert, A. Narita, K. Müllen, and L. Bogani. Magnetic edge

states and coherent manipulation of graphene nanoribbons. *Nature*, 557:691, 2018.

[106] S.S. Rao, S.N. Jammalamadaka, A. Stesmans, V.V. Moshchalkov, J. van Tol, D.V. Kosynkin, A. Higginbotham-Duque, and J.M. Tour. Ferromagnetism in graphene nanoribbons: Split versus oxidative unzipped ribbons. *Nano Letters*, 12(3):1210, 2012.

[107] S.S. Rao, A. Stesmans, J. van Tol, D.V. Kosynkin, A. Higginbotham-Duque, W. Lu, A. Sinitskii, and J.M. Tour. Spin dynamics and relaxation in graphene nanoribbons: Electron spin resonance probing. *ACS Nano*, 6(9):7615, 2012.

[108] S.S. Rao, A. Stesmans, J. van Tol, D.V. Kosynkin, and J.M. Tour. Magnetic defects in chemically converted graphene nanoribbons: Electron spin resonance investigation. *AIP Advances*, 4:047104, 2014.

[109] J. Lu, P.S.E. Yeo, C.K. Gan, P. Wu, and K.P. Loh. Transforming C_{60} molecules into graphene quantum dots. *Nature Nanotechnology*, 6:247, 2011.

[110] X. Ding. Direct synthesis of graphene quantum dots on hexagonal boron nitride substrate. *Journal of Materials Chemistry C*, 2:3717, 2014.

[111] X. Fei, X. Zhang, V. Lopez, G. Lu, H.-J. Gao, and L. Gao. Strongly interacting $C_{60}/Ir(111)$ interface: Transformation of C_{60} into graphene and influence of graphene interlayer. *The Journal of Physical Chemistry*, 119(49):27550, 2015.

[112] D. Jiang, Y. Chen, N. Li, W. Li, Z. Wang, J. Zhu, H. Zhang, B. Liu, and S. Xu. Synthesis of luminescent graphene quantum dots with high quantum yield and their toxicity study. *PloS One*, 10(12):0144906, 2015.

[113] R. Tian, S. Zhong, J. Wu, W. Jiang, Y. Shen, W. Jiang, and T. Wang. Solvothermal method to prepare graphene quantum dots by hydrogen peroxide. *Optical Materials*, 60:204, 2016.

[114] M. Zhao. Direct synthesis of graphene quantum dots with different fluorescence properties by oxidation of graphene oxide using Nitric acid. *Applied Sciences*, 8:1303, 2018.

[115] Y. Sun, Y. Zheng, H. Pan, J. Chen, W. Zhang, L. Fu, K. Zhang, N. Tang, and Y. Du. Magnetism of graphene quantum dots. *npj Quantum Materials*, 2:5,

2017.

[116] O.V. Yazyev and M.I. Katsnelson. *Theory of magnetism in graphene*, chapter 4, pages 71 – 103. Advanced Functional Materials, 2012.

[117] P.P. Shinde, O. Gröning, S. Wang, P. Ruffieux, C.A. Pignedoli, R. Fasel, and D. Passerone. Stability of edge magnetism in functionalized zigzag graphene nanoribbons. *Carbon*, 124:123, 2017.

[118] K.A. Ritter and J.W. Lyding. The influence of edge structure on the electronic properties of graphene quantum dots and nanoribbons. *Nature Materials*, 8:235, 2009.

[119] J. Viana-Gomes, V.M. Pereira, and N.M.R. Peres. Magnetism in strained graphene dots. *Physical Review B*, 80:245436, 2009.

[120] M. Kabir and T. Saha-Dasgupta. Manipulation of edge magnetism in hexagonal graphene nanoflake. *Physical Review B*, 90:035403, 2014.

[121] A. Valli, A. Amaricci, A. Toschi, T. Saha-Dasgupta, K. Held, and M. Capone. Effective magnetic correlations in hole-doped graphene nanoflakes. *Physical Review B*, 94:245146, 2016.

[122] J. Fernández-Rossier and J.J. Palacios. Magnetism in graphene nanoislands. *Physical Review Letters*, 99:177204, 2007.

[123] S. Haffad, L. Benchallal, L. Lamiri, F. Boubenider, H. Zitoune, B. Kahouadji, and M. Samad. Effect of vacancies on electronic and magnetic properties of hydrogen passivated graphene nanoribbons. *Acta Physical Polonica A*, 133(5):1307, 2018.

[124] M. Topsakal, E. Aktürk, H. Sevinçli, and S. Ciraci. First-principles approach to monitoring the band gap and magnetic state of a graphene nanoribbon via its vacancies. *Physical Review B*, 78:235435, 2008.

[125] G. Yang, B. Li, W. Zhang, M. Ye, and T. Ma. Strain-tuning of edge magnetism in zigzag graphene nanoribbons. *Journal of Physics: Condensed Matter*, 29:365601, 2017.

[126] S. Cheng, J. Yu, T. Ma, and N.M.R Peres. Strain induced edge magnetism at zigzag edge in graphene quantum dot. *Physical Review B*, 91:075410, 2015.

[127] S. Chacko, D. Nafday, D.G. Kanhere, and T. Saha-Dasgupta. Exact diagonalization study for nanographene: Modulation of charge and spin, magnetic phase diagram, and thermodynamics. *Physical Review B*, 90:155433, 2014.

[128] L.L. Song, X.H. Zheng, R.L. Wang, and Z. Zeng. Dangling bond states, edge magnetism, and edge reconstruction in pristine and B/N-terminated zigzag graphene nanoribbons. *Journal of Physical Chemistry C*, 114(28):12145, 2010.

[129] O. Voznyy, A.D. Güçlü, P. Potasz, and P. Hawrylak. Edge stability, reconstruction, zero-energy states and magnetism in triangular graphene quantum dots with zigzag edges. *Physical Review B*, 83:165417, 2011.

[130] S. Ganguly, M. Kabir, and T. Saha-Dasgupta. Magnetic and electronic phase crossovers in graphene nanoflakes. *Physical Review B*, 95:174419, 2017.

[131] J. Reuther, R. Thomale, and S. Rachel. Magnetic ordering phenomena of interacting quantum spin Hall models. *Physical Review B*, 86:155127, 2012.

[132] A. Vaezi, M. Mashkoori, and M. Hosseini. Phase diagram of the strongly correlated Kane-Mele-Hubbard model. *Physical Review B*, 85:195126, 2012.

[133] S.P. Sorella, A. Parola, M. Parrinello, and E. Tosatti. Numerical study of the $2D$ Hubbard model at half filling. *International Journal of Modern Physics B*, 3:1875, 1989.

[134] S. Sorella and E. Tosatti. Semi-metal-insulator transition of the Hubbard model in the honeycomb lattice. *Europhysics Letters*, 19(8):699, 1992.

[135] F.F. Assaad and I.F. Herbut. Pinning the order: the nature of quantum criticality in the Hubbard model on honeycomb lattice. *Physical Review X*, 3:031010, 2013.

[136] S. Sorella, Y. Otsuka, and S. Yunoki. Absence of a spin liquid phase in the Hubbard model on the honeycomb lattice. *Scientific Reports*, 2:992, 2012.

[137] N. Furukawa. Antiferromagnetism of the Hubbard mode on a layered honeycomb lattice-is MgB_2 a nearly-antiferromagnetic metal? *Journal of the Physical Society of Japan*, 70:1483, 2001.

[138] T. Paiva, R.T. Scalettar, W. Zheng, R.R.P Singh, and J. Oitmaa. Ground state and finite temperature signatures of quantum phase transitions in the half-

filled Hubbard model on a honeycomb lattice. *Physical Review B*, 72:085123, 2005.

[139] S. Arya, P.V. Sriluckshmy, S.R. Hassan, and A.-M.S. Tremblay. Antiferromagnetism in the Hubbard model on the honeycomb lattice: a two-particle self-consistent study. *Physical Review B*, 92:045111, 2015.

[140] C. Honerkamp. Density waves and Cooper pairing on the honeycomb lattice. *Physical Review Letters*, 100:146404, 2008.

[141] R. Triebl and M. Aichhorn. Topological insulator on honeycomb lattices and ribbons without inversion symmetry. *Physical Review B*, 94:165169, 2016.

[142] M. Grujić, M. Tadić, and F.M. Peeters. Antiferromagnetism in hexagonal graphene structures: Rings versus dots. *Physical Review B*, 87:085434, 2013.

[143] O.V. Yazyev. Magnetism in disordered graphene and irradiated graphite. *Physical Review Letters*, 101:037203, 2008.

[144] M. Zarenia, A. Chaves, G.A. Farias, and F.M. Peeters. Energy levels of triangular and hexagonal graphene quantum dots: a comparative study between the tight-binding and the Dirac approach. *Physical Review B*, 84:245403, 2011.

[145] G.E.W. Bauer, E. Saitoh, and B.J. van Wees. Spin caloritronics. *Nature Materials*, 11:391, 2012.

[146] S.R. Boona, R.C. Myers, and J.P. Heremans. Spin caloritronics. *Energy & Environmental Science*, 7:885, 2014.

[147] R. Beiranvand and H. Hamzehpour. Spin-dependent thermoelectric effects in graphene-based superconductor junctions. *Journal of Applied Physics*, 121:063903, 2017.

[148] H. Huang, A. Zheng, G. Gao, and K. Yao. Thermal spin filtering effect and giant magnetoresistance of half-metallic graphene nanoribbon co-doped with non-metallic Nitrogen and Boron. *Journal of Magnetism and Magnetic Materials*, 449:522, 2018.

[149] D.-D. Wu, H.-H. Fu, Q.-B. Liu, G.-F. Du, and R. Wu. Magnetic nanotubes: A new material platform to realize a robust spin-Seebeck effect and a perfect thermal spin-filtering effect. *Physical Review B*, 98:115422, 2018.

[150] M. Shirdel-Havar and R. Farghadan. Armchair graphene nanoribbons with giant spin thermoelectric efficiency. *Physical Chemistry Chemical Physics*, 20:16853, 2018.

[151] K. Uchida, S. Takahashi, K. Harii, J. Leda, W. Kishibae, K. Ando, S. Maekawa, and E. Saitoh. Observation of the spin Seebeck effect. *Nature*, 455:778, 2008.

[152] B.W. Wu, G.Y. Luo, J.G. Lin, and S.Y. Huang. Longitudinal spin Seebeck effect in a half-metallic $La_{0.7}Sr_{0.3}MnO_3$ film. *Physical Review B*, 96:060402(R), 2017.

[153] C.M. Jaworski, J. Yang, S. Mack, D.D. Awschalom, J.P. Heremans, and R.C. Myers. Observation of the spin-Seebeck effect in a ferromagnetic semiconductor. *Nature Materials*, 9:898, 2010.

[154] K. Uchida, H. Adachi, T. Ota, H. Nakayama, S. Maekawa, and E. Saitoh. Observation of longitudinal spin-Seebeck effect in magnetic insulators. *Applied Physics Letters*, 97:172505, 2010.

[155] S. Seki, T. Ideue, M. Kubota, Y. Kozuka, R. Takagi, M. Nakamura, Y. Kaneko, M. Kawasaki, and Y. Tokura. Thermal generation of spin current in an antiferromagnet. *Physical Review Letters*, 115:266601, 2015.

[156] S.M. Wu, W. Zhang, A. KC, P. Borisov, J.E. Pearson, J.S.L Jiang, D. Lederman, A. Hoffmann, and A. Bhattacharya. Antiferromagnetic spin Seebeck effect. *Physical Review Letters*, 116:097204, 2016.

[157] J. Holanda, D.S. Maior, O.A. Santos, L.H. Vilela-Leão, J.B.S. Mendes, A. Azevedo, R.L. Rodríguez-Suárez, and S.M. Rezende. Spin Seebeck effect in the antiferromagnet nickel oxide at room temperature. *Applied Physics Letters*, 111:172405, 2017.

[158] K. Uchida, J. Xiao, H. Adachi, J. Ohe, S. Takahashi, J. Ieda, T. Ota, Y. Kajiwara, H. Umezawa, H. Kawai, G.E.W. Bauer, S. Maekawa, and E. Saitoh. Spin Seebeck insulator. *Nature Materials*, 9:894, 2010.

[159] C.M. Jaworski, R.C. Myers, E. Johnston-Halperin, and J.P. Heremans. Giant spin Seebeck effect in a non-magnetic material. *Nature*, 487:210, 2012.

[160] L. Zhu, F. Zou, G. Gao, and K. Yao. Spin-dependent thermoelectric effects in $Fe - C_6$ doped monolayer MoS_2. *Scientific Reports*, 7:497, 2017.

[161] H. Liu, H. Kondo, and T. Ohno. Spintronic transport in armchair graphene nanoribbon with ferromagnetic electrodes: Half-metallic properties. *Nanoscale Research Letters*, 11:456, 2016.

[162] D. Zhang, M. Long, X. Zhang, L. Cui, X. Li, and H. Xu. Perfect spin filtering, rectifying and negative differential resistance effects in armchair graphene nanoribbons. *Journal of Applied Physics*, 121:093903, 2017.

[163] D. Kang, B. Wang, C. Xia, and H. Li. Perfect spin filter in a tailored zigzag graphene nanoribbon. *Nanoscale Research Letters*, 12:357, 2017.

[164] K. Li and X.-H. Zhang. Asymmetrical edges induced strong current-polarization in embedded graphene nanoribbons. *Physics Letters A*, 382:1167, 2018.

[165] H. Sadeghi, S. Sangtarash, and C.J. Lambert. Enhancing the thermoelectric figure of merit in engineered graphene nanoribbons. *Beilstein Journal of Nanotechnology*, 6:1176, 2015.

[166] Y.M. Zuev, W. Chang, and P. Kim. Thermoelectric and magnetothermoelectric transport measurements of graphene. *Physical Review Letters*, 102:096807, 2009.

[167] F. Ghahari, H.-Y. Xie, T. Taniguchi, K. Watanabe, M.S. Foster, and P. Kim. Enhanced thermoelectric power in graphene: Violation of the Mott relation by inelastic scattering. *Physical Review letters*, 116:136802, 2016.

[168] Y. Ouyang and J. Guo. A theoretical study on thermoelectric properties of graphene nanoribbons. *Applied Physics letters*, 94:263107, 2009.

[169] Y. Ni, K. Yao, H. Fu, G. Gao, S. Zhu, and S. Wang. Spin Seebeck effect and thermal colossal magnetoresistance in graphene nanoribbon heterojunction. *Scientific Reports*, 3:1380, 2013.

[170] J. Li, B. Wang, F. Xu, Y. Wei, and J. Wang. Spin-dependent Seebeck effects in graphene-based molecular junctions. *Physical Review B*, 93:195426, 2016.

[171] Z. Zhao, X. Zhai, and G. Jin. Bipolar-unipolar transition in thermospin transport through a graphene-based transistor. *Applied Physics Letters*, 101:083117, 2012.

[172] X.Q. Tang, X.M. Ye, X.Y. Tan, and D.H. Ren. Metal-free magnetism, spin-dependent Seebeck effect, and spin-Seebeck diode effect in armchair graphene nanoribbons. *Scientific Reports*, 8:927, 2018.

[173] H. Zheng, H.J. Liu, X.J. Tan, H.Y. Lv, L. Pan, J. Shi, and X.F. Tang. Enhanced thermoelectric performance of graphene nanoribbons. *Applied Physics Letters*, 100:093104, 2012.

[174] M.X. Zhai, X.F. Wang, P. Vasilopoulos, Y.S. Liu, Y.J. Dong, L. Zhou, Y.J. Jiang, and W.L. You. Giant magnetoresistance and spin Seebeck coefficient in zigzag α-graphyne nanoribbons. *Nanoscale*, 6:11121, 2014.

[175] H. Huang, G. Gao, H. Fu, A. Zheng, F. Zou, G. Ding, and K. Yao. Multiple thermal spin transport performances of graphene nanoribbon heterojuction co-doped with Nitrogen and Boron. *Scientific Reports*, 7:3955, 2017.

[176] Q.B. Liu, D.D. Wu, and H.H. Fu. Edge-defect induced spin-dependent Seebeck effect and spin figure of merit in graphene nanoribbons. *Physical Chemistry Chemical Physics*, 19:27132, 2017.

[177] J.F. Sierra, I. Neumann, J. Cuppens, B. Raes, M.V. Costache, and S.O. Valenzuela. Thermoelectric spin voltage in graphene. *Nature Nanotechnology*, 13:107, 2018.

[178] Z.C. Yang, Q.F. Sun, and X.C. Xie. Spin-current Seebeck effect in quantum dot systems. *Journal of Physics: Condensed Matter*, 26:045302, 2014.

[179] A. Valli, A. Amaricci, V. Brosco, and M. Capone. Interplay between destructive quantum interference and symmetry-breaking phenomena in graphene quantum junctions. *Physical Review B*, 100:075118, 2019.

[180] P.C. Martin and J. Schwinger. Theory of many-particle systems I. *Physical Review*, 115(6):1342, 1959.

[181] G. Baym and L.P. Kadanoff. Conservation laws and correlation functions. *The Physical Review*, 124(2):287, 1961.

[182] L.V. Keldysh. Diagram technique for nonequilibrium processes. *Soviet Physics Jetp*, 20:1018, 1965.

[183] Y. Meir and N.S. Wingreen. Landauer formula for the current through an interacting electron region. *Physical Review Letters*, 68:2512, 1992.

[184] V. Špička, B. Velický, and A. Kalvová. Electron systems out of equilibrium: Nonequilibrium Green's function approach. *International Journal of Modern Physics B*, 28(23):1430013, 2014.

[185] Supriyo Datta. *Quantum transport: Atom to transistor*. Cambridge University Press, New York, 2005.

[186] R. Landauer. Spatial variation of currents and fields due to localized scatterers in metallic conduction. *IBM Journal of Research and Development*, 1:223, 1957.

[187] M. Büttiker. Absence of backscattering in the quantum Hall effect in multiprobe conductors. *Physical Review B*, 38:9357, 1988.

[188] V.-N. Do. Non-equilibrium green function method: Theory and application in simulation of nanometer electronic devices. *Advances in Natural Sciences: Nanoscience and Nanotechnology*, 5:033001, 2014.

[189] J.S. Wang, J. Wang, and J.T. Lü. Quantum thermal transport in nanostructures. *The European Physical Journal B*, 62:381, 2008.

[190] S. Datta, P.F. Bagwell, and M.P. Anantram. *Scattering Theory of Transport for Mesoscopic Superconductors*. Purdue University, West Lafayette, 1992.

[191] M. Calperin, A. Nitzan, and M.A. Ratner. Heat conduction in molecular transport junctions. *Physical Review B*, 75:155312, 2007.

[192] C. Caroli, Combescot R., P. Nozieres, and D. Saint-James. Direct calculation of the tunneling current. *Journal of Physics C: Solid State Physics*, 4:916, 1971.

[193] A.P. Jauho, N.S. Wingreen, and Y. Meir. Time-dependent transport in interacting and noninteracting resonant-tunneling systems. *Physical Review B*, 50(8):5528, 1994.

[194] A. Dhar and D. Sen. Non-equilibrium Green's function formalism and the problem of bound states. *Physical Review B*, 73:085119, 2006.

[195] J.S. Wang, B.K. Agarwalla, H. Li, and J. Thingna. Nonequilibrium Green's function method for quantum thermal transport. *Frontiers of Physics*, 9:673, 2014.

[196] F. Covito, F.G. Eich, R. Tuovinen, M.A. Sentef, and A. Rubio. Transient charge and energy flow in the wide-band limit. *Journal of Chemical Theory and Computation*, 14(5):2495, 2018.

[197] C.J.O. Verzijl, J.S. Seldenthuis, and J.M. Thijssen. Applicability of the wide-band limit in DFT-based molecular transport calculations. *The Journal of Chemical Physics*, 138:094102, 2013.

[198] J. Vahedi and F. Barimani. Spin and charge thermopower effects in the ferromagnetic graphene junction. *Journal of Applied Physics*, 120:084303, 2016.

[199] W. Lin, M. Hehn, L. Chaput, B. Negulescu, S. Andrieu, F. Montaigne, and S. Mangin. Giant thermoelectric effect in Al_2O_3 magnetic tunnel junctions. *Nature Communications*, 3:744, 2012.

[200] L.A. Gonzalez-Arraga, J.L. Lado, F. Guinea, and P. San-Jose. Electrically controllable magnetism in twisted bilayer graphene. *Physical Review Letters*, 119:107201, 2017.

[201] H.-P Yang, W.-J. Yuan, J. Luo, and J. Zhu. Modulation of magnetic and electrical properties of bilayer graphene quantum dots using rotational stacking faults. *Chinese Physics B*, 28:078106, 2019.

[202] A. Georges, G. Kotliar, W. Krauth, and J. Rozenberg. Dynamical mean-field theory of strongly correlated fermion systems and the limit of infinite dimensions. *Reviews of Modern Physics*, 68:13, 1992.

[203] B. Chatterjee, J. Skolimowski, K. Makuch, and K. Byczuk. Real-space dynamical mean-field theory of Friedel oscillations in strongly correlated electron systems. *Physical Review B*, 100:115118, 2018.

[204] M.M. Odashima, B.G. Prado, and E. Vernek. Pedagogical introduction to equilibrium Green's functions: Condensed-matter examples with numerical

implementations. *Revista Brasileira de Ensino de Física*, 39:e1303, 2017.

[205] Z. Zhang, S. Hu, J. Chen, and B. Li. Hexagonal boron nitride: A promising substrate for graphene with high heat dissipation. *Nanotechnology*, 28:225704, 2017.

[206] G. Giovannetti, P.A. Khomyakov, G. Brocks, P.J. Kelly, and J. van den Brink. Substrate-induced band gap in graphene on hexagonal boron nitride: Ab initio density functional calculations. *Physical Review B*, 76:073103, 2007.